Structural Characterization of δβγ Epithelial Sodium Channels Provide Insight into Channel Assembly

by

Alexandra Houser

A DISSERTATION

Presented to the Neuroscience Graduate Program

and the Oregon Health and Science University

School of Medicine

in partial fulfillment of the requirements for the degree of

Doctor of Philosophy

August 2024

School of Medicine

Oregon Health and Science University

CERTIFICATE OF APPROVAL

This is to certify that the Ph.D. Dissertation of

ALEXANDRA HOUSER

has been approved on August 20th, 2024

Advisor, Isabelle Baconguis, Ph.D.

Member and Chair, Gary Westbrook, M.D.

Member, Swetha Murthy, Ph.D.

Member, Steve Reichow, Ph.D.

Member, Eric Gouaux, Ph.D.

Member, Shivani Ahuja, Ph.D

Table of Contents

Acknowledgements

This work is the culmination of the last six years of my life, but it could not have been done without the help of so many other people both in and out of the lab. I would have never been given the opportunity to accomplish this work if it was not for Dr. Isabelle Baconguis taking a chance on someone who had never done a protein purification in her life. Isabelle has been an outstanding mentor intellectually, at the bench, and on a personal level. Not many mentors would show up to the hospital on a Sunday night for their student.

It has been such a gift to learn biochemistry and structural biology surrounded by some of the most talented and intelligent scientists I have ever met. I have so much gratitude for Dr. Arpita Bharadwaj. Her patience and talent for teaching are something I can never thank her enough for. I will always be grateful for the time she spent teaching me cell culture and protein purifications those first few years. Not only is Arpita a phenomenal scientist and teacher, her laughter has always been one of my favorite parts of being in lab. The previous graduate students in the lab, Dr. Sigrid Noreng and Dr. Richard Posert, have left big shoes for me to fill. Both of them are constant sources of inspiration. While Sigrid and I only overlapped for a short time, she was the first person to show me how to collect data on an electron microscope. It was a magical and formative moment in my life and I so appreciate her introducing me to the world of cryo-EM. Rich was like a big brother in so many ways, we fought a little, we laughed a lot, but at the end of the day I am so lucky to him in my life. Rich is the reason I know the very little coding I do, which I am sure will benefit my career for rest of my life, even though I still use GraphPad Prism. I am also incredibly thankful for our Covid adoptees, Dr.

Kimberely Hartfield and soon to be Dr. James Cahill. Thank you, James, for all of the fun gossip over the years. I was least productive when we shared a bay, but I wouldn't have had it any other way. Kim, thank you for always having time for my random ponderings. Whether they are actually about science or are silly stylist things, like what colors I should use in a figure, you always gave it your full attention and have the best ideas. Your opinion is one of my highest regarded. Thank you also to all of the amazing people in the Gouaux lab, past and present. Especially Dr. Farzad Jalali-Yazdi for teaching me how to process single particle data, and Dr. April Goehring and Natalie Sheldon for all of the cells you gave me over the years. Last, but definitely not least, thank you soon to be Dr. Makayla Freitas. Graduate school is hard but having another graduate student to commiserate with on the first floor was so cathartic. It has been a pleasure having a built-in conference buddy and fellow victim of the ENaC/Deg transmembrane domains.

The last few years I have spent the majority of my waking life in lab, but the people who believed in and supported me outside the lab were the life force that kept me going. I would like to say thank you to my dad for always make me laugh and being my favorite drinking buddy. I would also like to thank my mom for always be an inspiration for women excelling in their career, you walked so I could run. Thank you to the Handford's who have been the best in laws ever, my favorite days are spent on your farm. A huge thank you goes to the Gamblin family, especially Aliyah Gamblin, without her I would have never gone back and finished high school, let alone get my PhD. Thank you to Tony Gamblin who was always my biggest fan, I'm sorry you're not here to see me get this far and I'm sorry I'll never be able to give you that autograph you always wanted. You are sorely missed.

The friends I made while in graduate school kept me afloat the last 6 years. I am so grateful to have been a part of the coolest cohort to have ever graced the NGP. They are so lucky to have us. Thank you to my friends who I made before graduate school that still put up with me, you have kept me grounded through the years. Thank you to the Alliance for Visible Diversity in Science (AVDS) for EVERYTHING. I made so many wonderful friends here, but I also learned so much about myself, my internal biases, but most importantly the tools to continually work on bettering myself. In AVDS I found community and support like no other, thank you for bringing so much light into my graduate experience.

Finally, I would like to thank my chosen family. Mason Handford has put up with the mean, bad, and the ugly of my stress while going through graduate school but he took it all in stride with foot rubs and warm homemade bread for me after the waters calmed. You're the best husband I could ever ask for, you are my best friend and my favorite person to mess with. Thank you for patiently explaining organic chemistry to me when I have a question, and most of all thank you for listening to me complain about my experiments even though I am sure I used way too much jargon most of the time and was impossible to understand. You're my favorite scientist and I am so excited to see where the years will lead us.

List of Abbreviations

ASIC	acid sensing ion channel
Cryo-EM	cryogenic electron microscopy
CNS	central nervous system
DDM	n-dodecyl-β-D-maltoside
DEG	degenerin
ECD	extracellular domain
eGFP	enhanced green fluorescent protein
EGTA	ethylene glycol tetraacetic acid
ENaC	epithelial sodium channel
Fab	fragment antibody
FSC	Fourier shell correlation
FSEC	fluorescent size exclusion chromatography
GRIP	gating relief of inhibition by proteolysis
HPLC	high performance liquid chromatography
IF	immunofluorescence
IHC	immunohistochemistry
MOI	multiplicity of infection
PBS	phosphate-buffered saline
SCNN1	sodium channel non-voltage gated 1
SEC	size exclusion chromatography
SEM	standard error of the mean
TEVC	two-electrode voltage clamp
TMD	transmembrane domain

List of Figures and Tables

Tables

APPENDIX

Abstract

When thinking of sodium channels in the nervous system the most notable are voltage gated sodium channels, but a multitude of non-voltage gated channels also contribute to sodium homeostasis in the brain. One of these lesser studied sodium channels in the nervous system is the Epithelial Sodium Channel (ENaC). The ENaC family of proteins are characterized by their sensitivity to amiloride and their high selectivity of sodium ions. ENaC is a uniquely proteolytically activated channel that is canonically composed of three subunits, α, β, and γ, to form a heterotrimer. However, shortly after αβγ ENaC was cloned, a fourth subunit was found, δ, which is most closely related to the α subunit and is therefore predicted to form a heterotrimer with the β and γ subunit. Despite the sequence similarity, α and δ containing ENaC differ in expression pattern, protease activation, and channel selectivity. While δ ENaC's importance in humans is stressed by its expression throughout the brain, pancreas, testis, and ovaries, there is still a large gap in our knowledge of δ ENaC compared to αβγ ENaC. In large part this is due to the δ subunit not being expressed in *Mus musculus*, where the majority of previous ENaC studies have been conducted. In order to expand our knowledge on δ ENaC, I heterologously expressed human δβγ ENaC in HEK293S GnTI- cells. Utilizing single particle cryogenic electron microscopy, I resolved the first structure of δβγ ENaC at 3.38Å resolution. Several notable differences are apparent between α and δ containing channels that inform the differences in channel function. Interestingly, our structural studies also demonstrated the presence of ββγ heterotrimers and βγ dimers, which may relate to the process of ENaC subunit assembly. At a functional level, *Xenopus laevis* oocytes expressing human δβγ ENaC resulted in increased currents at pHs below 6. We also observed that while αβγ ENaC is activated by Zn^{2+}, the same concentration of Zn^{2+} significantly inhibited δβγ ENaC. These results demonstrate that δ ENaC can form a heterotrimeric channel with the β and γ subunits and establish a novel role for Zn^{2+} as an endogenous antagonist for δ-containing ENaCs.

Chapter One

Introduction

The δ ENaC Subunit

Overview of Epithelial Sodium Channels

Membrane proteins are involved in a multitude of first responder type roles such as anchoring the cell in the environment, recognizing neighbors, and signaling to neighboring cells or systemically when in a multicellular organism. A key subtype of membrane proteins that are found in nearly every cell type from Archaea to Eukarya are ion channels (Anderson and Greenberg, 2001; Pohorille et al., 2005). Ion channels bridge the hydrophobic plasma membrane by acting as aqueous tunnels to allow ions such as K^+ or Cl^- in and out of cells. Ion channels are essential for a number of cellular and organismal processes that can range from signaling for a cell to die, to allowing you to read this sentence (Bortner and Cidlowski, 2014; Wang et al., 2017). Many ion channels are selective in terms of what ions they allow to pass through their pores, with some being more permeable to anions like Cl^-, whereas others only allow in cations of similar sizes such as Li^+ and Na^+ (Alexander et al., 2011). In addition to their differences in selectivity, ion channels can be opened or closed by a variety of stimulus, such as the voltage across the plasma membrane, temperature, acidity of extracellular environment, and even by pressure being applied to the cell (Alexander et al., 2011). With the large breadth of diversity in function and consequential utilization of ion channels within life as we know it, increasing our understanding of channel function is critical to our comprehension of biology as well as the future development of pharmacological therapies.

Many ion channels are obvious drug targets, such as voltage-gated sodium channels for pain relief, but a large number of targets have been predominantly unexplored. One such ion channel, that has recently been aptly named as “an underestimated drug target”, is the Epithelial Sodium Channel (Lemmens-Gruber and Tzotzos, 2023). Epithelial Sodium Channels (ENaC) have been found to be expressed throughout the human body and have a long and rich history among the ion channels. Before the Epithelial Sodium Channel was identified and named, there were hints of its presence through work investigating the transport of water and ions across epithelial cells. Early work looked at the application of sodium chloride and subsequent water intake, but it wasn’t until 1948 that it was first hypothesized that the transport of sodium and chloride ions were separate. Using a beautifully designed apparatus that would subsequently be used in many other pioneering papers, Hans Ussing was able to measure the flux of ions across isolated frog (*Rana pipiens*) skin (Ussing, 1949). Following the idea that sodium and chloride are transported separately, the importance of sodium transport across membranes and the relationship to water retention was demonstrated in frog skin (*Rana esculenta*) (Fuhrman and Ussing, 1951). The intricacies of the ion selectivity across frog skin started to become apparent when it was revealed that while the apical membrane of frog skin allows transport of Na^+ and Li^+, it is largely impermeable to K^+ (Koefoed-Johnsen and Ussing, 1958). In the same year, it was illustrated that these properties of sodium and water transport were not unique to frogs and was identified in other epithelial cells, notably in the epithelia of toad (*Bufo marinus* and *Bufo bufo*) bladder (Bentley, 1958; Leaf et al., 1958). In the toad bladder, hints of the intricate regulation of this sodium channel first emerged through work in the Leaf lab at

Harvard when it was found that the transport of sodium across toad bladder was increased in the presence of aldosterone, a hormone that we now know increases ENaC activity (Crabbé, 1961; Stockand, 2002; Verrey, 1995).

A critical point of ENaC characterization occurred in 1967 when it was found that the application of amiloride, which is now recognized as a blocker of ENaC, led to an increase of sodium in the renal tubules of dogs (Baer et al., 1967). This result was replicated a year later in toad bladder (*Bufo marinus*), calling attention to the wide variety of epithelial cells whose sodium transport is disrupted in the presence of amiloride (Bentley, 1968). This discovery is key because it allowed isolation of ENaC ion flux by recording the amiloride sensitive current, allowing researchers to answer targeted ENaC questions. Using amiloride-sensitive currents, the idea of Na^+ self-inhibition was first shown in isolated frog skin (*Rana esculenta*), that is to say, prolonged exposure to Na^+ results in a closure of the channel (Fuchs et al., 1977). With the use of amiloride sensitive currents, in the early 1980's using bullfrog skin (*Rana catesbeiana*) and toad bladder (*Bufo marinus*) it was determined that the ion selectivity of epithelial expressing ENaC was $Li^+ > Na^+ > K^+$ with the ratio of $Na^+:K^+$ permeability being greater than 1000:1 (Benos et al., 1980; Palmer, 1982). When this is considered in relation to voltage-gated sodium channels, which have been demonstrated to have a Na^+ to K^+ selectivity ratio from 3-18:1, it becomes clear that ENaCs are particularly selective for a Na^+ channel (Ulmschneider et al., 2013).

Then came the dawn of patch-clamp electrophysiology. In 1985 single channel recordings of ENaC were accomplished via cell-attached recordings on the apical membrane of rat cortical collecting tubules demonstrating a single channel conductance

of 5 pS (L. G. Palmer and Frindt, 1986; L G Palmer and Frindt, 1986). This work was pivotal to the understanding of epithelial channel function, but at this point we still had no clue as to the composition of this channel, nor even an established name.

In fact, it was not until over 50 years after the first recordings that the epithelial sodium channel was cloned and named. Using a cDNA library from rat colon the first ENaC subunit was cloned and named the α subunit of the rat epithelial Na^+ channel (αrENaC) (Canessa et al., 1993). Canessa and colleagues found transcripts for αENaC in the medulla and cortex of rat kidney as well as the distal colon. Northern blots showed no αENaC RNA in rat proximal colon, brain or liver. With the isolated cDNA they established that αrENaC can assemble into a pore forming channel by itself in *Xenopus* oocytes. The cloning and establishment of αrENaC as an ion channel had large implications not just for ENaCs, but also for the ENaC/Degenerin superfamily as a whole. By comparing the cDNA for αrENaC to DNA sequences in the EMBL Nucleotide Sequence Database and the NIH GenBank, they found that αENaC was very closely related to two recently cloned *C. elegan* genes, *deg-1* and *mec-4*. These two genes were identified in *C. elegans* by a screen that tested for touch insensitive worms following mutagenesis with ethyl methanesulphonate (EMS) (Chalfie and Au, 1989). The *deg-1* mutant has a dominant phenotype in which specific types of neurons, including touch neurons, swell and lyse (Chalfie and Wolinsky, 1990). The resulting *mec-4* gene mutation was characterized shortly after, and carries a similar dominant mutation phenotype which causes the lysis of touch sensitive neurons (Driscoll and Chalfie, 1991). Curiously, while both the *deg-1* and *mec-4* mutants from the EMS screen caused neuronal death, knockout of the genes had no observable phenotype. Based on this observation and what was

known of the sequence, it was thought that these two genes coded for membrane receptors that when specific dominant mutations were induced, might signal for an uncharacterized inherited neurodegenerative disease similar to Huntington's or ALS (Driscoll and Chalfie, 1991). However, the cloning of αrENaC by Canessa and colleagues rewrote the hypothesis that they were membrane receptors, to them being ion channels and *C. elegan* homologues of mammalian epithelial sodium channels. Despite initially misinterpreting the function of these *C. elegan* genes, the discovery of *deg-1* and *mec-4* through this EMS screen was central to the identification of what is now known as the degenerin mutation, a residue that is conserved across the ENaC/degenerin superfamily that when mutated drastically increases the open probability of the channel.

A year after cloning the α subunit, the β and γ subunits were cloned by the same group. By screening for functional complementation against the α subunit in rats, they were able to isolate cDNA for what they termed the β-rENaC and γ-rENaC subunits (Canessa et al., 1994). A number of crucial observations about ENaC came from this study. Notably, they found that when injecting *Xenopus* oocytes with either β and γ alone, or in combination with each other, no amiloride sensitive currents were detected. It was only when β or γ were co-injected with the α subunit that amiloride sensitive currents were observed. Moreover, when all three subunits, α, β, and γ were injected, the amplitude of the currents were 100 fold greater than α alone. More importantly, single channel recording done via patch-clamp electrophysiology on oocytes expressing all three subunits showed a conductance of 4.6-7.7pS, which was consistent with recordings from native ENaC (Canessa et al., 1994; Kemendy et al., 1992; L G Palmer and Frindt, 1986). This implication of ENaC being composed of three homologous subunits spread

beyond ENaC to the *C. elegan* Degenerin proteins. In an exciting blockbuster event for the ENaC/Degenerin superfamily, the Nature issue that published Canessa and colleagues 1994, also contained two papers that immediately followed it supporting the idea that Degenerins in *C. elegans* are ion channels and are composed of homologous subunits, similar to mammalian ENaC (Hong and Driscoll, 1994; Huang and Chalfie, 1994). At the time, the story of human ENaC composition seemed to be at an end, with Canessa even going so far as stating "At present there is no reason to believe that other subunits are required for reconstituting the basic functions of the channel." In just a little over a year though we would be introduced to the fourth member of the ENaC family.

Discovery and cloning of δ ENaC

At first glance it may seem strange for Canessa and colleagues to make such a bold statement when a year later a fourth ENaC subunit would be discovered. It is important to note though that all of their work was done in rats. It was Waldmann and colleagues use of human databases that led them to the fourth subunit, δ (Waldmann et al., 1995). Using the sequences of α, β, and γ they identified a partial match in GenBank. From there they used this partial sequence to screen a human kidney cDNA library that resulted in a 3.4kb clone that coded for a protein that is 638 amino acids in length. Comparison between the three known ENaC subunits showed it is most similar to the α subunit with a 37% identity overlap. Similar to the α subunit, Waldmann and colleagues recorded amiloride-sensitive currents from *Xenopus* oocytes injected with δ cRNA alone. When adding β and γ, the amplitude of those currents increased 50 fold, which is similar to the increases seen with the α subunit in the presence of β and γ (Canessa et al., 1994; Waldmann et al., 1995). Although those were surprisingly similar traits for δ and the α

subunit to share, there were notable differences between the function of these two subunits. In both δ homotrimers and δβγ heterotrimers, there were larger inward currents of Na^+ compared to Li^+ with a ratio of I_{Li+}/I_{Na+}=0.6 for δ compared to I_{Li+}/I_{Na+}~2 for α containing ENaC. Additionally, they observed that while δ ENaC is still sensitive to the blockers amiloride and benzamil, it is significantly less sensitive than α ENaC containing channels: δ ENaC ($IC50_{amiloride}$=2.6μM, $IC50_{benzamil}$=0.27μM); α ENaC ($IC50_{amiloride}$=80nM, $IC50_{benzamil}$=7nM). Single channel conductance of Na^+ also differed between δ and α ENaC containing channels, 11.6±0.4 pS and 4.8±0.3 pS respectively. Surprisingly, the conductance for Li^+ remained nearly the same: δβγ = 6.8±0.5 pS and αβγ = 7.3±0.2 pS (Waldmann et al., 1995).

The differences between α- and δ-containing single channel function and how this could relate to differences in function at an organismal level was highlighted by Waldmann and colleague's results from Northern blot analysis of δ mRNA among human tissue. Although δ ENaC was cloned from human kidney, the kidney actually showed very low expression of δ when compared to other tissues. The highest levels of δ mRNA were found in the testes, ovaries, pancreas, and brain. (Waldmann et al., 1995). Despite the abundance of information about the δ subunit gained from this manuscript, there were also many questions left unanswered. The work in this paper led the authors to postulate how the composition of different ENaC subunits effect channel function. They were particularly surprised by the similarities of macroscopic properties (such as selectivity and pharmacology) between α and δ homotrimers compared to them in complex with β and γ. Waldmann suggested that this could be due to either δ and α being the pore forming subunits, or α and δ forming channels with small levels of endogenous *Xenpous*

β and γ when injected alone. Based on comparison to another member of the ENaC/DEG super family, Acid Sensing Ion Channels (ASICs), it is unlikely that α or δ entirely form the pore of ENaC (Gonzales et al., 2009). As for the possibility of endogenous β and γ in *Xenopus* oocytes forming a small number of channels when exogenous α and δ are introduced, we are not able to definitively answer that as it is not established whether β and γ ENaC are expressed in oocytes. It is entirely possible that β and γ are indeed expressed endogenously, especially since *X. laevis* oocytes have been shown to express δ ENaC in small quantities (Babini et al., 2003). It should be noted however that the δ subunit is expressed endogenously at such low quantities in oocytes that when RNA for *X. laevis* β and γ subunits are injected into oocytes, amiloride sensitive currents are not detectable. It is only when *X. laevis* RNA for the δ subunit is added in concert with β and γ, are large amiloride sensitive currents present (Wichmann et al., 2018). If the β and γ subunits were expressed at a similar level as δ in oocytes, we would not expect exogenous α or δ to form complexes with endogenous β and γ at a level such that we would be able to detect amiloride sensitive currents. It is not uncommon in other organisms and tissues for ENaC subunits to be expressed at varying levels though, so it would be remiss to assume that if β and γ are expressed in oocytes, that they would be at similarly low levels as endogenous *Xenopus* δ is in oocytes (Amin et al., 2005; Krueger et al., 2012; Wichmann et al., 2018).

In a massive 2004 sequencing effort of human cDNA, a clone was identified that was described as ‘highly similar to amiloride-sensitive sodium channel delta-subunit’ (Ota et al., 2004). Two papers came out almost back to back cloning this cDNA from human brain to identify a second δ isoform named δ_2 (Giraldez et al., 2007; Yamamura et

al., 2006). Both studies found that δ_2 contains an elongated N terminus, expanding the length from 638 amino acids to 703 (Yamamura et al., 2006) or 704 residues (Giraldez et al., 2007) based on a frame shift in exon 3 and alternative splicing of exon 4. Yamamura and colleagues concluded that there is no functional difference between the δ and δ_2 isoforms, both as homotrimers and in complex with β and γ. However, the results from the Yamamura 2006 paper, along with other work by their group on δ ENaC, has been quite controversial. One explanation for the lack of functional differences between δ and δ_2 reported by Yamamura is that the authors did not use multiple cell types and they had a low number of replicates compared to other work that support difference in δ_1 and δ_2 function (Wesch et al., 2012). The second cloning of δ_2 was done a year later and is more widely accepted in the field, based on this the majority of the focus on δ_2 for this introduction will be placed on the cloning work done by Giraldez and colleagues in 2007.

Using RT-PCR Giraldez and colleagues reported δ_2 expression in brain, muscle, and pancreas, but not in kidney, lung, and liver. By expressing δ_2 in *Xenopus* oocytes they were able to detect an amiloride-sensitive current when co-expressed with β and γ ENaC, but not with δ_2 alone. Peculiarly, the amiloride sensitive currents from $\delta_2\beta\gamma$ were 10 fold smaller than αβγ ENaC. Western blots of homogenized oocytes post injection showed similar levels of $\delta_2\beta\gamma$ expression as αβγ, so an issue with expression does not explain the difference in current amplitude. To investigate whether this could be due to low levels of $\delta_2\beta\gamma$ being trafficked to the plasma membrane, they injected oocytes with a YFP tagged δ_2, along with β and γ and then compared fluorescent signal to oocytes injected with YFP tagged α, β, and γ. The oocytes expressing $\delta_2\beta\gamma$ showed levels of fluorescence similar to un-injected oocytes, suggesting that almost no channels were being trafficked to the

plasma membrane (Giraldez et al., 2007). Based on these results and RT-PCR results showing almost no expression of β and γ in human brain, these authors proposed that the low levels of δ_2 at the membrane is due to δ_2 not preferentially forming a channel with β and γ. The authors suggested that *in vitro* this δ isoform preferentially forms channels with other members of the ENaC/degenerin family, such as ASIC1 or ASIC2 that are found in pyramidal neurons in rats (Alvarez de la Rosa et al., 2002; Duggan et al., 2002; Lingueglia et al., 1997). Further work done by Giraldez and colleagues demonstrated that both δ and δ_2 ENaC are expressed in pyramidal neurons in human cortex and in the telencephalon of monkeys (*Macaca fascicularis*). Using *in situ* hybridization they determined that both isoforms are neuronal specific and not expressed in neighboring glia, and with double labeling they found that the expression of δ isoforms in neurons were non-overlapping. Depending on the region of the cortex, neurons expressing one of the isoforms were either in distinct clusters, or were intermingled (Giraldez et al., 2007). The stark pattern of differential expression between the two isoforms in pyramidal neurons raises two important questions, what is the role of δ in the brain and what are the functional differences in neurons expressing either of the two δ isoforms.

A history of δ and δβγ functional work

In the previous section, I describe the initial functional work for both δ ENaC alone and δβγ ENaC pharmacology, selectivity, and conductance. Nearly 10 years after δ was cloned, work was done to identify the underlying cause for the difference seen in α and δ selectivity and pharmacology (Ji et al., 2004). Using three sets of chimeras (labeled as *i, ii,* and *iii*) for δ and α they swapped the following regions between each subunit: *i*. the palm domain (β sheets 10-12) and the knuckle domain, *ii*. the half of transmembrane

domain 2 closest to the extracellular space (TM2a) as predicted by AlphaFold3, and *iii.* chimera *i* and *ii* combined (**Introductory Figure 1**). The authors tested whether any of the chimeras effected the selectivity or pharmacology. Some very slight changes were noticed in the sensitivity to amiloride in the *i* chimeras. The *i*-αβγ channels became slightly less sensitive to amiloride when mutated and the *i*-δβγ became a little more sensitive to amiloride, but neither fully reverted to the other's expected dose response to amiloride so there is likely more at play than this region when it comes to differences of amiloride IC_{50} between αβγ and δβγ ENaC (Ji et al., 2004). The *i* chimeras not fully reversing the amiloride sensitivity is not wholly unexpected as one of the key residues for amiloride sensitivity that has been identified for the α subunit is S556. The S556 residue is located in TM2a, which is not included in the *i* chimera (Schild et al., 1997). That being said, if S556 is responsible for a large portion of the amiloride inhibition of α containing channels, it is strange that the authors did not see a change in amiloride sensitivity with either chimera *ii* or *iii* as those do contain TM2a. Overall there were no large changes in selectivity with the chimeras with the exception of the *ii*-αβγ which showed a slight increase in Na^+ current compared to wild type αβγ (from 5pS to 7pS), but the pattern of larger currents for Li^+ compared to Na^+ remained and they were not able to replicate this result when doing inside out patches (Ji et al., 2004). While this work did not give clear answers as to what was involved in the pharmacology and selectivity differences between α and δ containing ENaC, it is striking to see that when what is predicted to be all of TM2a is swapped, no large changes are seen. This is especially surprising when taking into account that in ASICs TM2a is thought to be largely responsible for the selectivity filter (Gonzales et al., 2009; Yoder and Gouaux, 2020).

Later that same year two papers were published suggesting that δ ENaC's Na^+ current is increased in the presence of protons. The first of these papers looked at homomeric δ based on evidence of δ ENaC being expressed in the human brain while β and γ are not (McDonald et al., 1995; Waldmann et al., 1995). Recordings from *Xenopus* oocytes showed an increase in amiloride-sensitive inward current when the pH was lowered from 7.5 to 6.5 and continued to increase as pH is lowered until plateauing at pH 4, with a half maximal activation at pH 5 (Yamamura et al., 2004a). The authors also found that in both oocytes and Chinese hamster ovary cells (CHO-K1), the inward current at pH 5 was more than double the current at pH 7.5 (Yamamura et al., 2004a). The second paper examined the effect of protons on the heteromeric channel, δβγ ENaC (Ji and Benos, 2004). The authors started with homomeric δ and saw an EC_{50} at pH 6, which is notably higher than Yamamura's results (Yamamura et al., 2004a). When looking at δβγ, they saw an 44 fold increase in the current compared to δ alone but a similar EC_{50} of pH 6 (Ji and Benos, 2004). However the majority of the experiments were performed at pH4, a not particularly physiologically relevant pH and far from their reported EC_{50} of pH 6. The authors suggest that the degenerin site mediates proton activation of δβγ but this is controversial in the field and needs further investigation (Ji and Benos, 2004). These two studies focused on δ ENaC in the brain, but pH levels below 6 are not common in the extracellular space of the central nervous system except in extreme instances such as ischemia (Fedorovich et al., 2020). Although the brain does not often reach such levels of acidity, there is evidence suggesting expression and proton activation of δ ENaC at <pH 5 in human skin and the stomach lining (Yamamura et al., 2008b, 2008a). Recent work investigating the effect of pH on δ from the Althaus lab

investigated proton activation of the *Xenopus* δβγ channel (Wichmann et al., 2019). While they saw a substantial response of 7-8 fold larger amiloride sensitive currents in the presence of protons with an EC_{50} of pH 6.9 in *Xenopus* δβγ ENaC, they saw no change in current from pH 8-6 in human δβγ ENaC (Wichmann et al., 2019). This is not only a surprising result for human δβγ, but they also observed no change in amiloride sensitive current from pH 8-6 for αβγ, which has been thought to be inhibited by protons (Chalfant et al., 1999; Konstas et al., 2000; Zhang et al., 1999). The results from Wichmann and colleagues leave a lot of uncertainty surrounding whether human δ is proton sensitive or not.

Beyond pH there are no known endogenous activators of δ ENaC, though two synthetic agonists have been identified. One is a vanilloid, capsazepine, that seems to be δ specific as it had no effect on αβγ ENaC. When investigating other vanilloids or structurally related compounds, such as capsaicin or dopamine respectively, no effect was observed with δ ENaC (Yamamura et al., 2004b). The same group found that icilin, a synthetic compound that while unrelated to menthol elicits a similar feeling of cold in humans, acted as an agonist for δ ENaC (Yamamura et al., 2005). The authors suggested that these compounds could be used as a lead for drug development targeting δ containing ENaCs.

Role of δ in the human body

As mentioned previously, the initial cloning work for δ and δ_2 reported expression in the brain, pancreas, testes, ovaries, and muscle (Giraldez et al., 2007; Waldmann et al., 1995). This has been supported by RNA dot blot analyses showing δ ENaC mRNA in brain, heart, kidney, and pancreas (Yamamura et al., 2004a). Since this early work, the

vast majority of δ has been found to express in the nervous system with the exception of human umbilical vein endothelial cells (Downs et al., 2018) and *Xenopus* δ in urogenital tissues (Wichmann et al., 2018). In the eye, δ was first observed in the retina along with the other three ENaC subunits and ASIC1-4 by RT-PCR (Brockway et al., 2002). However in this same study, only α and β were observed by immunohistochemistry (IHC) and by Western blot only α and β ENaC and ASIC1 were detected. Work by Krueger and colleagues 10 years later replicated the RT-PCR findings, demonstrating α, δ, β, and γ expressed widely throughout the eye. Similar to Brockway et al. 2002, no evidence for translation of δ was observed in the eye. Using IHC only β and γ were detected (Krueger et al., 2012). Evidence for a role of δ in taste was first established in 2008 when RT-PCR results found mRNA for all 4 ENaC subunits in circumvallate, fungiform cells, and non-chemosensory lingual tissue, though δ mRNA was 100 fold lower than other ENaC subunits (Stähler et al., 2008). For α, β, and γ expression was highest in non-chemosensory lingual tissue and from surrounding epithelial tissue, which the authors suggest could explain the low levels of δ expression compared to α, β, and γ. Using an antibody for δ, that is unfortunately no longer available (Chemicon AB3536P), Stähler and colleagues reported that δ organized in a ring-like structure to the pore in the apical membrane of every taste bud whereas the other ENaC subunits immunolocalized to the basolateral membrane. The authors mention that the pore of taste bud cells are “sticky”, that is, the pore is known for non-specific binding of antibodies. This is worth mentioning believe many commercial antibodies for δ are not specific, such as the Invitrogen δ ENaC antibody (PA5-87738) which reportedly shows reactivity to human, rat, and mouse δ, although there is no δ in rats or mice. Stähler argues that since all the ENaC subunit

antibodies were raised in the same organism and non-specific binding does not occur with the α, β, or γ antibodies that the δ antibody binding to the pore is specific. The function of δ ENaC in the taste bud pore is not yet understood and needs further investigation.

Expression of δ isoforms in the human brain has been well mapped. Both δ and δ_2 are expressed in human brains, with δ_2 only reported in primates (Giraldez et al., 2007; Waldmann et al., 1995; Wesch et al., 2012). Both δ and δ_2 have been observed in pyramidal neurons in layers II, VI, and the underlying white matter in the frontal and temporal cortices in humans and in the telencephalon of monkeys in a non-overlapping pattern (Giraldez et al., 2007; Wesch et al., 2012). Additionally, expression of δ was also seen by Northern blotting in cerebellum and hippocampus (Yamamura et al., 2004a).

These differences in δ and δ_2 expression, especially the fact that co-expression of the two isoforms has not been observed, brings into question what role each isoform plays in neurons. Earlier work that was discussed found that there was a difference in whole cell currents for *Xenopus* oocytes expressing either δ or δ_2 with β and γ ENaC, with $\delta_2\beta\gamma$ resulting in substantially smaller amiloride sensitive currents (Giraldez et al., 2007). In this paper it was determined that the smaller currents were due to a lack of channels at the plasma membrane of oocytes. A few years later, Giraldez expanded further on this in her own lab by expressing both $\delta_2\beta\gamma$ and $\delta\beta\gamma$ in *Xenopus* oocytes and in human embryonic kidney 293 (HEK 293) cells. In both oocytes and HEK 293 cells they observed smaller currents for $\delta_2\beta\gamma$ compared to $\delta\beta\gamma$, but single channel recordings showed nearly identical conductance for channels containing either isoform (Wesch et al., 2012). Fluorescent microscopy with YFP tagged δ and δ_2 found that fluorescence at the

membrane was 2-fold lower for oocytes injected with $\delta_2\beta\gamma$ ENaC. Interestingly this difference was shown to be independent of association with the β and γ subunits. When δ and δ_2 were injected into oocytes without β and γ, overall currents were markedly reduced, but a 3-fold larger whole cell current was still observed with δ compared to δ_2 (Wesch et al., 2012). Only the β and γ subunits have PY binding motifs, so it is surprising that the difference in δ isoform levels at the membrane persists in the absence of β and γ since PY motifs are necessary for trafficking facilitated by Nedd4-2, an established ubiquitin ligase for αβγ channel regulation (Goulet et al., 1998; Staub et al., 1996). The authors concluded that because δ does not have a PY motif, another method of either insertion or removal of the channel must be at play. Further supporting that the difference in δ isoform abundance at the membrane does not seem to be regulated by Nedd4-2, knocking down dynamin with dynasore resulted in no change in current for either isoform of δ. This contrasts with the significant increase in current observed with αβγ when dynasore was introduced, giving the impression that δβγ channel regulation is independent of dynamin dependent clathrin mediated endocytosis which has been established for αβγ ENaC (Shimkets et al., 1998; Wang et al., 2006). By making a series of mutations in the N terminus of δ_2, which is the region where the two δ isoforms differ, they found that only when both groups of residues 25-45 and 66-85 are deleted from δ_2 are whole cell currents equal to δ and levels at the plasma membrane are increased to δ levels (Wesch et al., 2012). While this work did not conclude what role these residues play in membrane abundance of δ_2, they did find that while there are less pyramidal neurons expressing δ_2 in human cerebral cortex, qPCR shows that the levels of mRNA for δ and δ_2 correlate to the number of neurons observed expressing either isoform. The

authors postulate from this that if δ isoforms abundance in the cell membrane is similar in pyramidal neurons when compared to oocytes and HEK 293 cells, that while neurons expressing δ or δ_2 have nearly equal levels of RNA, the neurons containing δ RNA will be more excitable than δ_2 expressing neurons since more channels will be at the plasma membrane (Wesch et al., 2012).

Regulation of δ, let alone the differences in regulation between subunits, is still not fully understood. The first hint at regulation of δ ENaC came from the McDonald lab via a screen for binding partners using a yeast two-hybrid screen with the N- and C-terminal domains of ENaC. They found a protein that would later be identified as COMMD1, which binds to the C-terminus of δ ENaC between residues 592-615 (Biasio et al., 2004). Recordings from *Xenopus* oocytes with two electrode voltage clamp (TEVC) showed that the presence of COMMD1 significantly reduces the current of δβγ ENaC (Biasio et al., 2004). Later the same group investigated how co-expression COMMD1 and δβγ ENaC reduced amiloride sensitive currents when compared to δβγ alone. Using co-immunoprecipitation experiments with an HA tagged δ subunit and serial mutations to COMMD1, they found that COMMD1 binds to δ via the COMM domain, residues 100-190 (Chang et al., 2011). When co-expressing COMMD1 with δ ENaC in COS-7 cells, they found 50% less δ ENaC at the cell surface compared to δ without COMMD1 by Western blot analysis of biotin labeled surface protein. They also found an increase in δ ubiquitination when co-expressed with COMMD1, from which the authors hypothesize that COMMD1 promotes the ubiquitination of δ ENaC (Chang et al., 2011). In 2013, the McDonald lab furthered our understanding a bit more by finding that ubiquitination of δ is dependent on three cytosolic residues, K42 and K84 on the N-

terminus and K584 on the C-terminus. While single and double mutants of each lysine to an arginine result in a reduction of ubiquitination, only the triple mutant completely abolished ubiquitination of δ ENaC (Ly et al., 2013). The triple mutant also significantly increased both the amount of intracellular and cell surface δ when compared to wild type δ. Ly and colleagues argue this supports that ubiquitination is required for trafficking intracellular and surface δ ENaC. Additionally, Ly and colleagues shed more light on the players involved in δ regulation. By co-expressing δ with the ubiquitin ligase XIAP they saw an increase of δ which they believe stems from downregulation of COMMD1 by XIAP, supported by the reduction of COMMD1 signal by Western blot when XIAP is introduced (Ly et al., 2013). With δβγ ENaC they also found that introduction of Nedd8, a ubiquitin like protein that binds to and activates RING E3 SCF ligases, increases δ ENaC ubiquitination as well as a reduces δ and δβγ currents. A similar effect was seen with αβγ when Nedd8 was introduced (Ly et al., 2013). Lastly, while δ does not have a PY motif, it was found that when δβγ is co-expressed with Nedd4-2, δ ubiquitination is increased and amiloride sensitive currents are reduced by nearly 80%, which is comparable to the reduction seen with αβγ ENaC (Kabra et al., 2008; Ke et al., 2010; Ly et al., 2013). This last result is controversial because it directly contradicts work done by Teresa Giraldez' group the year before suggesting regulation of δ and δ_2 is independent of Nedd4-2 (Wesch et al., 2012). Both studies were performed in *Xenopus* oocytes, but both groups failed to perform experiments to definitively say whether or not the δ population is reduced at the cell surface when Nedd4-2 is introduced. This could have been verified with biotin labeling or fluorescent microscopy, techniques used in each paper respectively for other experiments in their same manuscript, to ascertain whether there was a

reduction in δ at the cell surface. Instead, the conclusions were reached by comparing differences in amiloride sensitive currents. Additionally, Wesch and colleagues did not use Nedd4-2 in any of their experiments, instead their hypothesis relied on δ not having a PY motif and work that suggested Nedd4-2 regulation of ENaC is through clathrin mediated endocytosis (Shimkets et al., 1998; Wang et al., 2006). To bring clarity to whether δ ENaC is regulated by Nedd4-2, experiments to measure the amount of δ ENaC at the cell surface with and without Nedd4-2 present are needed.

Comparison of δ to other ENaC/Deg Channels

Differences in expression between δ and other ENaC/Deg channels

While there is not a substantial amount of knowledge on the δ subunit, the comparison of δ to other ENaC/Deg proteins can provide a better understanding of the unique role for the δ subunit. Where a protein is expressed in an organism can tell a lot about its function. As discussed earlier, δ ENaC is found extensively throughout the central and peripheral nervous system. Interestingly, with the exception of epithelial cells in vasculature, the α, β, and γ subunits have not been reported in noticeable quantities in human brain (Drummond et al., 2004; Giraldez et al., 2007). That does not make δ unique in its neuronal expression among ENaC/Deg proteins. The first genes to be cloned in this family, *deg-1* and *mec-4* are expressed in *C. elegan* neurons (Chalfie and Wolinsky, 1990; Driscoll and Chalfie, 1991). In *D. melanogaster*, the insect ENaC homologue *pickpocket* (*ppk*) was first cloned and found to be involved in mechanosensation in the peripheral nervous system (Adams et al., 1998; Darboux et al., 1998). Even in humans there are other ENaC/DEG channels. For example, before Acid Sensing Ion Channels (ASICs) got

their official name they were called Brain Sodium Channels (BNaC) (García-Añoveros et al., 1997; Waldmann et al., 1997). Amoung the ASICs, δ ENaC is most similar ASIC1 with a 16% identity overlap of sequences (Hanukoglu and Hanukoglu, 2016). In the human brain ASIC1 is expressed in glia and involved in responses to neuronal disease and injury in microglia, astrocytes, and oligodendrocytes (Feldman et al., 2008; Huang et al., 2010; Vergo et al., 2011; Yang et al., 2016; Yu et al., 2015). There is an insubstantial amount of work looking into whether δ ENaC is in glia, but the Barres lab Brain RNA Seq data suggests that δ ENaC is found in human fetal astrocytes, though at a $1/10^{th}$ the level of ASIC1 (Zhang et al., 2016). No significant levels of RNA were found for δ in adult astrocytes, which agrees with *in-situ* hybridization work showing no co-localization of δ and GFAP in adult human cortex (Giraldez et al., 2007; Zhang et al., 2016).

Much of the cell specific expression of ASIC1 has been done in mice and found to be expressed in numerous neuronal cell types, notably pyramidal cells in the hippocampus, in the cingulate cortex, and throughout the neocortex with particularly strong signal in layers 2/3 (de la Rosa et al., 2003; Lingueglia et al., 1997; Price et al., 2014; Wemmie et al., 2003). The localization of ASIC1 to layers II/III in mice is interesting when thinking about how δ ENaC is localized to layers II and VI of the neocortex of humans (Giraldez et al., 2007). Is the localization of ASIC1 in mice cortex the same in humans? If so, is δ playing a redundant role in layer II or is it interacting with ASIC1 in some way as has been hypothesized in the literature (Giraldez et al., 2007)? Without detailed analysis of ASIC1 expression in humans it is difficult to even form a solid hypothesis in either direction. There is inconsistency of ENaC/DEG expression between rodent and human CNS, so it would be remiss to assume ASIC1 expression in

the human cortex layers match that of mice. Although α, β, and γ have not been seen in humans neurons, in rats which lack the δ subunit, both rtPCR and immunostaining showed α, β, and γ in rat brain, especially in the cortex, hippocampus, thalamus, and amygdala (Amin et al., 2005). Curiously, the strongest immunoreactivity was seen in rat cortical neurons in layers II and VI, correlating to the distribution of δ in the human cortex. These apparent differences between rat and human expression of ENaC/DEG channels in the cortex leaves a lot to be explored.

Function and sequence comparison to αβγ ENaC and ASIC

The ENaC subunit most similar to δ is the α subunit based on sequence comparison. Interestingly, despite only sharing a sequence identity of 37%, both α and δ can form a channel with β and γ. There are a number of regions that are conserved between α and δ that are not found in β and γ. Most notable of these regions is an almost 45 residue long sequence that is nearly identical between α and δ on the N terminus prior to what is predicted to be transmembrane domain 1 (TM1) (**Introductory Figure 1a**). The original cloning paper for δ ENaC speculated that this region could be critical for association with the β and γ subunits (Waldmann et al., 1995). Another region of similarity between the α and β subunit, based on sequence comparison, is the predicted hinge that separates TM2a and TM2b. However, there is substantial conservation within this region for β and γ as well, which is not unexpected since this region is predicted to form the selectivity filter for ENaCs.

In the ENaCs three residues have been identified as belonging to the selectivity filter. In the human ENaC subunits α, β, and γ, those residues are GSS (587-589), GGS (531-533), and SCS (540-542) respectively (Kellenberger et al., 1999a, 1999b, 2001;

Kellenberger and Schild, 2002a; Li et al., 2003; Sheng et al., 2000; Snyder et al., 2000). Mutations in these residues lead to an increase in permeability to K^+ and in some cases cause a reduction of permeability to other ions such as Li^+. These residues are also conserved within the larger ENaC/DEG family. In ASIC1a these residues are known as the GAS (443-445) belt (Baconguis et al., 2014). Most similar to ASIC1a in this respect, the δ subunit of ENaC in primates selectivity motif is GAS (537-539). This similarity is particularly interesting given the selectivity of each channel. Where αβγ is more permeable to Li^+ than Na^+, both ASIC1a and δ ENaC containing channels are more permeable to Na^+ with a Na^+ to Li^+ ratio of 1.3 and 2, respectively (Waldmann et al., 1997, 1995).

Another potential similarity between ASICs and δ ENaC is activation by protons. While it has recently come in to question whether human δ ENaC responds to protons at all, there is more evidence suggesting that low pH increases the open probability of δ ENaC (Ji and Benos, 2004; Wichmann et al., 2019; Yamamura et al., 2008a, 2008b, 2004a). Within the supporting body of work, there are some notable differences between the pH sensitivity of ASICs and δ ENaC. The EC_{50} of pH for ASIC1a has been reported as being between 6.2-6.4 (Sutherland et al., 2001; Waldmann et al., 1997). This is higher than the purported EC_{50} for δ ENaC that is between pH 5-6 (Ji and Benos, 2004; Yamamura et al., 2004a). However, this difference is not exceptional when comparing to the range of values for proton EC_{50} among the ASICs. ASIC3 has a reported EC_{50} of 6.5-6.7, while ASIC2a has been reported to have an EC_{50} less than 4.5 (Champigny et al., 1998; Sutherland et al., 2001; Ugawa et al., 2001; Waldmann et al., 1997). There are also substantial differences in the gating kinetics of proton-induced current between ASICs

and δ ENaC. For ASICs within 30 seconds the pH elicited current is almost completely gone, though with δ containing ENaC at 120 second the current is still at nearly 100% of the peak current after introduction of protons (Yamamura et al., 2004a).

By comparison to other members of the ENaC/DEG family we start to piece together a picture of δ ENaC and its role, but there are still a lot of missing pieces. In this dissertation I solve the first structure of δβγ ENaC as well as investigate Zn^{2+} and proton modulation of this channel. When solving the structure of δβγ we found unique assemblies of β and γ ENaC that are not present in our structural work with αβγ (Noreng et al., 2018, 2020). The work in this dissertation highlights the importance of subunit assembly on ENaC function and gives insight into how individual subunits come together to form functional heterotrimers.

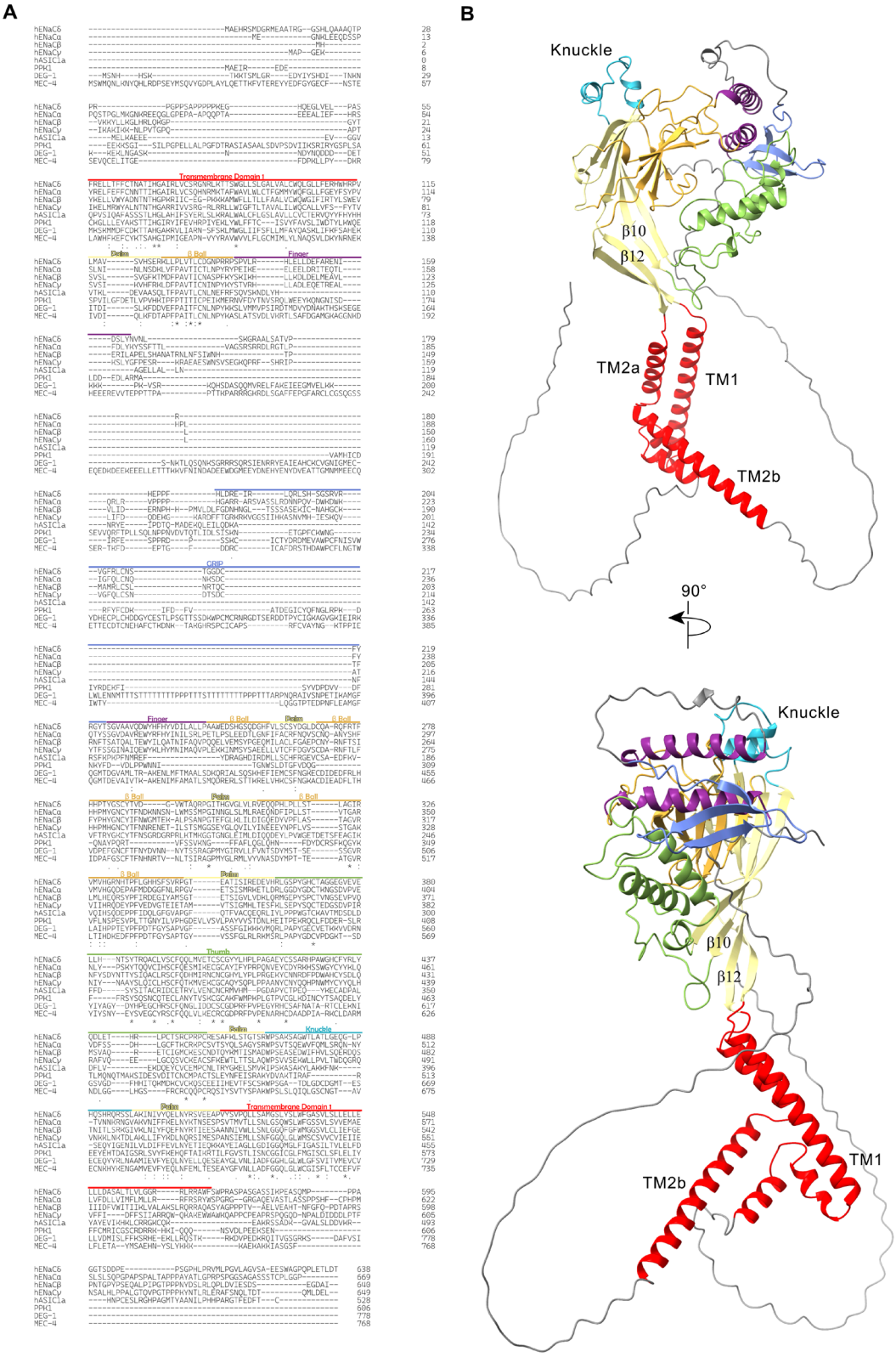

Introductory Figure 1. A. Alignment of δ ENaC to homologues, predicted subdomains from AlphaFold3 model **B.** Alphafold3 model of δ with subdomains colored as in (A)

Chapter Two

Structural Insights into Subunit-Dependent Functional Regulation in Epithelial Sodium Channels

Alexandra Houser and Isabelle Baconguis

This chapter is currently available as a preprint on bioRxiv and is in the final stage of review with Cell Reports

Houser A, Baconguis I. Structural Insights into Subunit-Dependent Functional Regulation in Epithelial Sodium Channels. bioRxiv [Preprint]. 2024 May 30:2024.05.28.595834. doi: 10.1101/2024.05.28.595834. PMID: 38853903; PMCID: PMC11160588.

Summary

Epithelial sodium channels (ENaC) play a crucial role in Na^+ reabsorption in mammals. To date, four subunits have been identified—α, β, γ, and δ—believed to form different heteromeric complexes. Currently, only the structure of the αβγ complex is known. To understand how these channels form with varying subunit compositions and define the contribution of each subunit to distinct properties, we co-expressed human δ, β, and γ. Using single-particle cryo-electron microscopy, we observed three distinct ENaC complexes. The structures unveil a pattern in which β and γ positions are conserved among the different complexes while the α position in αβγ trimer is occupied by either δ or another β. The presence of δ induces structural rearrangements in the γ subunit explaining the differences in channel activity observed between αβγ and δβγ channels. These structures define the mechanism by which ENaC subunit composition tunes ENaC function.

Introduction

The regulation of sodium ion (Na^+) movement and homeostasis within cells is a fundamental biological process. The epithelial sodium channel (ENaC), a member of the diverse Degenerin/ENaC superfamily, plays a pivotal role in Na^+ reabsorption (Kellenberger and Schild, 2002b). Dysfunction of ENaC is linked to various diseases, particularly hypertension, which impacts a billion people globally and continues to be the primary cause of morbidity and mortality (Muntner et al., 2018; Soundararajan et al., 2010). ENaCs are composed of three homologous subunits, are sensitive to the pore blocker amiloride, and exhibit selectivity for Na^+ over K^+(Benos et al., 1980; Bentley, 1968; Jasti et al., 2007; Kellenberger and Schild, 2002b; Palmer, 1982; Staruschenko et al., 2005). Previous studies identified four subunits - α, β, γ, and δ - and demonstrated a preferential heteromeric assembly of ENaC, forming either αβγ or δβγ complexes (Canessa et al., 1994; Lingueglia et al., 1993; Waldmann et al., 1995). The α and δ subunits are most similar in protein sequence with a homology identity of 37% (Waldmann et al., 1995). Each subunit confers at least five known distinct channel characteristics when combined with β and γ subunits. First, δ-containing ENaC channels are found in both epithelial and non-epithelial tissues, with the highest expression in reproductive organs, the pancreas, and the brain (Giraldez et al., 2007; Waldmann et al., 1995; Yamamura et al., 2006; Zhao et al., 2012). On the other hand, α-containing ENaCs are expressed in tight epithelial cells in the kidney, lung, and colon (Garty and Palmer, 1997; Hummler, 1999; Hummler et al., 1996; Mall et al., 2010; Shareghi and Stoner, 1978). Second, while δβγ and αβγ selectively permit Na^+ and Li^+ over K^+, the I_{Li+}/I_{Na+} permeability ratios for each channel are 0.6 and 2.0, respectively (Ji et al., 2004; Ji and

Benos, 2004; Waldmann et al., 1995). Third, the αβγ channel displays higher sensitivity to the blocker amiloride compared to δβγ by an order of magnitude (Ji et al., 2004; Waldmann et al., 1995). Fourth, single channel recordings of the δβγ trimer demonstrate a higher opening probability (P_o) than αβγ (Krueger et al., 2012). As a result, δβγ is largely unaffected by proteases when compared to αβγ which displays increased activity after exposure to proteases (Chraïbi et al., 1998; Haerteis et al., 2009; Kleyman et al., 2009; Vallet et al., 1997; Vuagniaux et al., 2002; Wichmann et al., 2018). Lastly, a phenomenon known as Na^+ self-inhibition is significantly diminished in δβγ, whereas in αβγ, this process reduces channel activity (Bize and Horisberger, 2007; Fuchs et al., 1977).

These variations in expression and channel properties underscore the functional differences between α- and δ-containing ENaCs. While extensive research has been conducted on the structure-function relationship of α-containing ENaC since its identification, there is a significant gap in knowledge concerning δ-containing ENaC. Although all four ENaC subunits are expressed in humans, common mammalian model organisms such as rats and mice do not express δ, hampering in-depth understanding of its function in mammals (Giraldez et al., 2012; Ji et al., 2012). To deepen our understanding of ENaC function and, more specifically, to elucidate the molecular basis of distinct properties between δβγ and αβγ, we employed single-particle cryo-electron microscopy and complemented it with electrophysiology to obtain a three-dimensional reconstruction of the assembly and to identify key structural elements that result in the distinct characteristics exhibited by these two ENaC proteins (Hanukoglu and Hanukoglu, 2016).

Results

Functional characterization of the human δβγ epithelial sodium channel

To investigate the δβγ channel, we designed constructs containing wild-type human δ, β, and γ. To confirm δβγ function, we utilized two-electrode voltage clamp (TEVC) electrophysiology with *Xenopus* oocytes, the standard technique used in the δβγ field (Giraldez et al., 2007; Haerteis et al., 2009; Ji et al., 2004; Ji and Benos, 2004; Rauh et al., 2016; Waldmann et al., 1995; Wesch et al., 2012; Wichmann et al., 2019, 2018; Yamamura et al., 2006; Zhao et al., 2012) Consistent with literature, our construct exhibited the expected ion selectivity pattern of δβγ ENaC (**Figure S1A**). We expanded our functional characterization to compare the response of δβγ to Zn^{2+}, a divalent cation known to elicit a biphasic reaction from αβγ (Chen et al., 2012; Sheng et al., 2000). It has been demonstrated that Zn^{2+} has a stimulatory effect at low concentrations and an inhibitory effect at high concentrations in αβγ. Upon exposure to 100 μM Zn^{2+}, we observed a surprising decrease in δβγ-mediated Na^+ current, which contrasted with the previously characterized increase in Na^+ current with αβγ at the same Zn^{2+} concentration (**Figure 1A, B**). Using a similar range of Zn^{2+} concentrations as in previous studies, we observed a comparable biphasic response in αβγ (**Figure S1B**). However, this behavior was not observed in δβγ; instead, Zn^{2+} exclusively inhibited δβγ at this concentration range, with an IC_{50} of 63 μM (**Figure S1C**). To our knowledge, this experiment marks the first demonstration of the inhibitory effect of Zn^{2+} on δβγ, shedding light on the significance of this cation to ENaC function and underscoring how variations in subunit composition can yield diverse responses to external modulators.

Stabilization of the trimeric δβγ ENaC complex for structure determination

To investigate the differences in channel properties between δβγ and αβγ, we modified our constructs for expression in human embryonic kidney (HEK) cells and isolation, tagging the γ subunit with enhanced green fluorescent protein (eGFP) to enable structure determination by single-particle cryo-EM. The final construct contains wild-type human δ, β, and γ tagged with eGFP, collectively referred to as $\delta\beta\gamma_{WT}$ (**Figure S1D**). Cells expressing $\delta\beta\gamma_{WT}$ exhibited a clear preference for Na^+ over Li^+ by whole-cell patch-clamp electrophysiology, in agreement with prior δβγ research findings and our TEVC results (**Figure 1C and Figure S1A**) (Waldmann et al., 1995). This suggests that $\delta\beta\gamma_{WT}$ retains wild-type properties and confirms that tagging the γ subunit does not disrupt its overall function.

The distinct behavior of the δβγ complex we observed relative to αβγ extends further to its biochemical characteristics (Noreng et al., 2020, 2018). We employed the same purification strategy as the human αβγ, exploiting the high-affinity interaction between a GFP nanobody and the eGFP covalently fused to the γ subunit (Kubala et al., 2010; Rothbauer et al., 2008). When $\delta\beta\gamma_{WT}$ is expressed and purified, two major populations, termed pop1 and pop2, emerge as monitored by fluorescence-detection size-exclusion chromatography (FSEC) (**Figure 1D**) (Kawate and Gouaux, 2006). Pop2 aligns with the expected trimeric ENaC assembly, consistent with the heteromeric αβγ complex. Conversely, pop1 elutes earlier, suggesting a larger complex that is not present in purified human αβγ (**Figure S1E**) (Noreng et al., 2020). To determine whether either population contained relevant conformations of ENaC, we sought out to biochemically and

structurally characterize both populations. We first focused on strategies to isolate and characterize pop2 because its peak position corresponds to the αβγ trimer, and thus, the predicted position of δβγ trimer.

To improve expression and to generate ideal substrates for detailed structural analysis via single-particle cryo-EM, we systematically designed and screened several other mutant candidates. Numerous investigations have identified and characterized protease recognition sites within the extracellular domain of the γ subunit, one of which is recognized by furin (Adebamiro et al., 2007; Bruns et al., 2007; Diakov et al., 2008; Donaldson et al., 2002; Ergonul et al., 2006; Frindt et al., 2008; García-Caballero et al., 2008; Harris et al., 2007; Hughey et al., 2004; Kabra et al., 2008; Passero et al., 2008; Picard et al., 2008; Vallet et al., 1997). To reduce biochemical variability arising from the putative furin-mediated cleavage during expression, a mutation involving a single residue at the presumed furin site of the γ subunit, specifically R138A, was incorporated producing a construct deemed $\delta\beta\gamma_{R138A}$ (**Figure S1D**). $\delta\beta\gamma_{R138A}$ behaved similarly to $\delta\beta\gamma_{WT}$ biochemically (**Figure 1D**). By replacing cysteines located in the pre-transmembrane domain 1 (pre-TM1) with alanines in all three subunits of $\delta\beta\gamma_{R138A}$, we also created a third candidate, termed $\delta\beta\gamma_{CYS}$ (**Figure S1D**). Biochemical analysis unveiled distinct behavior between the three δβγ constructs based on the distribution between pop1 and pop2 (**Figure 1D**). Despite attempts to exclusively collect pop2 with $\delta\beta\gamma_{WT}$ and $\delta\beta\gamma_{R138A}$, there was still contamination from pop1. Successful separation was achieved exclusively with $\delta\beta\gamma_{CYS}$.

Functional characterization of $\delta\beta\gamma_{R138A}$ and $\delta\beta\gamma_{CYS}$ revealed that they exhibited similar amiloride-sensitive inward currents to $\delta\beta\gamma_{WT}$ when expressed in HEK cells.

However, $\delta\beta\gamma_{CYS}$ behaved differently from $\delta\beta\gamma_{WT}$, displaying a small decay in Na^+ inward current over time compared to sustained currents observed in $\delta\beta\gamma_{WT}$ and $\delta\beta\gamma_{R138A}$ (**Figure 1E**). It has been shown that alterations to the cysteines in the preTM1 region result in channels that favor the closed state in αβγ ENaC (Mueller et al., 2010; Mukherjee et al., 2014). The current decay observed in $\delta\beta\gamma_{CYS}$ suggests a similar effect is occurring in $\delta\beta\gamma_{CYS}$. Overall, the three δβγ constructs exhibited functional behavior consistent with a characteristic δβγ channel, showing a preference for Na^+ over Li^+. However, the $\delta\beta\gamma_{CYS}$ construct demonstrated an elevated K^+ current (**Figure 1C, F, and G**). The effective separation of pop1 from pop2 when expressing and purifying δβγCYS prompted us to focus on $\delta\beta\gamma_{CYS}$ for in-depth structural analysis (**Figure 1D**).

Mapping the ENaC subunits in different heteromeric complexes

We utilized the 10d4 fragment-antigen binding domain (Fab) to label the β subunit and to facilitate particle alignment during cryo-EM data processing (Noreng et al., 2018). Reference-free two-dimensional (2D) classification and three-dimensional (3D) reconstruction revealed two different trimeric populations: one with one Fab and the other with two Fabs bound (**Figure S2A**). The trimer with two Fabs bound contains two β, which was an unexpected finding. Beyond just relying on Fab binding, we employed additional strategies to differentiate between the three subunits. The quality of both maps provided sufficient detail to construct the main chain and guide placement of large aromatic residues. Along with the distinct glycosylation pattern of each subunit, this allowed us to confidently determine which subunits belonged to specific positions on the map (**Figure 2A, 2B, and S2B).** After careful inspection of these maps, we determined that the monoFab trimer comprises δ, β, and γ, which we refer to as $\delta\beta\gamma_{CYS}$. The diFab

complex consists of two β and a γ, and we call this trimer $\beta\beta\gamma_{CYS}$ (**Figure 2A-D and S2A**).

The majority of the extracellular domains of $\delta\beta\gamma_{CYS}$ and $\beta\beta\gamma_{CYS}$ were resolved with reported resolutions of 3.4 Å and 3.1 Å, respectively, based on the gold standard Fourier shell correlation (GSFSC) at 0.143 (**Figure 2A, B, S2C-H, and Table S1**). However, like the previous human αβγ cryo-EM studies, the transmembrane domains remain unresolved (Noreng et al., 2020, 2018). Based on the constructed model, the arrangement of the $\delta\beta\gamma_{CYS}$ subunit is consistent with the αβγ arrangement, with the δ-β-γ orientation following a counterclockwise direction when viewed from the extracellular side and down the pore axis (**Figure 2C**) (Noreng et al., 2018). In comparing the three trimers-δβγCYS, ββγCYS, and αβγ-β and γ subunits maintain the same positions, while the δ subunit in δβγCYS and the second β in ββγCYS occupy the equivalent position of the α subunit in αβγ (**Figure 2A-D**).

We did not observe a trimeric complex comprising one β and two γ subunits or a complex consisting of three γ subunits (**Figure S2A**). The presence of 10d4 bound to the β subunit in all trimers indicated that the binding of the Fab is not dependent on the subunit composition of the trimer. To simplify the analysis, we designated the position occupied by α, δ, and β as position 1, and the positions consistently occupied by β and γ subunits as positions 2 and 3, respectively **(Figure 2E).** To distinguish between the two β subunits within the $\beta\beta\gamma_{CYS}$ complex, we denote the β subunit in position 1 as β^1 and the one in position 2 as β^2 (**Figure 2B, D**).

Architecture of the δ subunit

The δ subunit shares a structural resemblance with α, β, and γ, exhibiting subunit domains arranged in a hand-like configuration clenching a ball replete with β strands, first observed in the crystal structure of chicken ASIC1 (**Figure 2F**).(Jasti et al., 2007) Similar to α, β, and γ, δ also comprises extended anti-parallel helices, namely α1 and α2, which form part of the finger domain. These helices resemble a wall positioned between the functionally important β6-β7 loop and the thumb domain (Noreng et al., 2018). Like β, δ is thought to be insensitive to proteases but harbors the **g**ating **r**elief of **i**nhibition by **p**roteolysis domain, or GRIP, which forms extensive contacts with the finger and thumb domains (Noreng et al., 2018). The knuckle sits atop the expansive palm domain and makes contacts with the adjacent γ finger (**Figure 2F)**. While the upper palm domain is well-resolved, the lower palm domain in δ is disordered, hindering precise positioning of the β strands that directly connect to the transmembrane domains and wrist region (**Figure 2A**). This stands in stark contrast to β and γ, which exhibit clear β strands in the lower palm domains. Similarly, the αβγ maps also displayed defined features in the lower palm domain (Noreng et al., 2020, 2018). The disorder observed in the lower palm domain in δ may suggest that this region adopts more conformations compared to the other subunits.

Position 1 subunit modulates conformational changes

To compare the trimers, we leveraged the well-resolved map regions encompassing the α2 helices within the finger domains of each subunit. Our rationale was grounded in the superior map quality in this specific region, allowing us to assign and position residues, particularly the bulky aromatic side chains (**Figure 3A, B, and S3**).

With this approach, we focused on evaluating the distances of the Cα atoms of conserved tryptophans between associated subunits and then compared the relative distance between each position in the three trimers. We chose these key tryptophans—Trp232 (δ), Trp251 (α), Trp218 (β), and Trp229 (γ)—because they are located in a region where domains believed to regulate ENaC activity converge, incorporating the thumb, finger, and GRIP domains (Noreng et al., 2020, 2018). Collectively, these conserved tryptophans form a triangle, which we refer to as TriTrp. The TriTrp triangle exhibited distinct side lengths between the trimers, with the $\delta\beta\gamma_{CYS}$ TriTrp triangle featuring longer sides than those of αβγ (PDB: 6WTH) and $\beta\beta\gamma_{CYS}$ (**Figure 3C-E**)**.** The TriTrp triangle within $\beta\beta\gamma_{CYS}$ forms an isosceles triangle with two sides measuring about 53 Å (**Figure 3D**). The different TriTrp distances between positions 2 and 3, which are consistently occupied by β and γ, in the three trimers suggest that the subunit in position 1 can alter domain positions in the trimer.

To identify regions contributing to changes in the extracellular domain, we systematically compared the corresponding subunit at positions 1-3 of each trimer by superposing them. We observed conformational differences in the finger domains of the subunits occupying positions 1 and 3 (**Figure 4, Table S2**). Conversely, in position 2, the β subunits exhibited almost identical structures, demonstrating an overall root-mean-square-deviation (RMSD) of less than 0.50 Å (**Figure S4A**). The remarkable similarity of the β subunits in position 2 from the three trimers served two distinct purposes. First, it demonstrated that the β subunit undergoes minimal conformational changes even when the subunit in position 1 changes. Second, it confirmed that the cryo-EM maps and resulting models were consistent and on the same map scale. Thus, observed rigid-body

differences between the trimers are valid and not artifacts derived from map scale discrepancies.

Comparing the subunits occupying position 1, α, δ, and β^1 differ in sequence and molecular interactions contributing to variations in the overall trimer conformations. Evaluating the respective domains revealed significant differences, especially the β-ball domains (**Table S2**). Because of the location of the β-ball, nestled between the structurally homogeneous upper palm domain on one side and the gating domains on the other, we opted to concentrate on this region and explore how its architecture could lead to differences in the conformation of the surrounding domains between the three subunits (**Figure 4A**). Positioned beneath the finger domain, a region that is thought to mediate gating in ENaC and encompasses the β6-β7 loop and the α1 and α2 helices, the β-ball in δ displays a distinct arrangement compared to α and β^1 (**Figure 4B-D**). Differences in molecular interaction were observed near the interface between the thumb domain and the β7-β8 loops. In this loop, α and β^1 contain acidic residues while histidines occupy the corresponding positions in δ. With a RMSD of over 3 Å, these loops present distinct conformations and establish varied contacts with the base of the thumb domains. While phenylalanines of both α and β^1 (αPhe361 and β^1Phe328) forge contacts with the base of the α4 helix of the thumb region, the equivalent δPhe337 faces away from the base of α4 and instead forms contacts with the residues in the β-ball (**Figure 4B**).

The conformation of the finger domain remains similar between δ and α, but there are clear sequence variations likely contributing to the differences in functional behavior of channels containing δ or α. For instance, the β6-β7 loop, crucial for mediating Na^+-self inhibition in αβγ, features a putative cation site near Asp338 in the structure (**Figure 4D**)

(Kashlan et al., 2015; Noreng et al., 2020; Sheng et al., 2006). However, in the δ loop, the corresponding residue is a proline, which lacks a negative charge to directly interact with Na^+ based on the structure (**Figure 4B**). In this region, δ differs in conformation from α, where δ-His315 points toward the pore axis while α-Phe339 is oriented away (**Figure 4E**). The β6-β7 loop of δ closely resembles that of β^1, which is akin to those found in position 2 β and γ in all three trimers suggesting that the swapped conformation observed in α-Asp338 and Phe339 is not unique to the subunit occupying position 1 but more specific to α (**Figure 4E, F, and S4B**) (Noreng et al., 2020).

To ascertain the importance of His315 for δβγ function we used TEVC to test the effect of mutating His315. Interestingly, no measurable current was observed for H315F, suggesting that this site is not interchangeable with the corresponding residue found in α (Phe339) (**Figure 4E, S4C**). A smaller aliphatic residue, such as alanine in H315A, resulted in measurable but markedly reduced currents, while the isosteric substitution H315Q was better tolerated, displaying statistically significant larger currents than H315A (**Figure S4C**). These findings indicate that this region in δ is sensitive to perturbation. The adjacent proline likely contributes to a more rigid conformation that favors the orientation of the His315 sidechain to participate in polar interactions within the β6-β7 loop, which phenylalanine and alanine cannot perform (**Figure 4E**).

The β6-β7 loop conformation must affect the position of the α-helical segments of the finger domain (Kashlan et al., 2015). Comparison of the Cα positions of the core finger domain in the three subunits occupying position 1 demonstrated that β^1 is the most different (**Table S2**, **Figure 4A-D**). This difference observed in β^1 is likely influenced by the interaction between the β6-β7 loop and the α1 helix, facilitated by the presence of

bulkier side chains such as Phe309 and Met119, respectively. In contrast, the equivalent residues in δ and α involve smaller side chains, such as leucine, alanine, and threonine (**Figure 4B-D and S4D**). The conformational differences are more pronounced when shifting away from the central pore axis toward the periphery, where the thumb domain is located. While α and β^1 exhibit similar conformations, δ displays the most distinct conformation, characterized by a roughly 15° rotation of the α5 helix within the thumb domain (**Figure S4E**).

We also inspected the knuckle domains of each subunit as these domains establish extensive contacts with the neighboring finger domains. We focused on understanding how the knuckle domain at position 1 might mediate variations in the domain positions surrounding it. The knuckle domain in position 1 abuts the finger domain of the γ subunit in position 3. We discovered that a conserved tryptophan in the knuckle domain that assumes similar rotamers packs tightly against the α6 helix in α, β, and γ (**Figure 4G, H and S4F).** However, the tryptophan found in δ exhibits a rotamer that extends away from the helix main chain, likely affecting the position1-position3 interface (**Figure 4G and S3A**).

The γ subunit finger domains adopt different conformations

To identify conformational shifts in the subunits at position 3, we aligned the γ subunits, examined the resulting RMSD values for each subunit domain, and found the finger domain exhibited the greatest difference (**Table S2**). Within the finger domain, we identified variations in the positions of three components: the β6-β7 loop, α1, and α2 helices (**Figure 5A**). The β6-β7 loops displayed marked differences, with the main chain involving Val322 and Ser323 adopting swapped positions in γ-δβγ_{CYS} relative to γ-ββγ_{CYS}

and γ-αβγ_{6WTH} (**Figure 5B-D, S3C, and S5A**). This alteration influences the position of Phe320, which directly interacts with the α1 and α2 helices of the finger domain. When assessing the angle formed by the two helices within each subunit, we observed that α1 and α2 create a 23° angle in γ-αβγ_{6WTH}, while the equivalent helices in γ-δβγ_{CYS} and γ-ββγ_{CYS} form 11° and 16° angles (**Figure 5B-D**). Examining this angular change within the context of a trimer revealed that the α2 helices in the γ-δβγ_{CYS} and γ-ββγ_{CYS} are pushed outward from the pore axis when compared to that of γ-αβγ_{6WTH} by about 10° and 4°, respectively (**Figure 5E, F**). The substantial rotation of the finger helices stands in stark contrast to the positioning of the thumb domains in γ. We did not observe substantial rotations of the thumb domains across all three γ subunits (**Figure S5B**).

Comparison of the maps among the three trimers unveils differences in the GRIP domains of the γ subunit (**Figure S5C**). The γ subunits in the δβγ_{CYS} and ββγ_{CYS} complexes have similar map characteristics in the GRIP domain, featuring an additional element not observed in the αβγ_{6WTH} complex. To determine the identity of this map feature, we generated a model of the δβγ trimer using AlphaFold3 (Abramson et al., 2024). In the predicted model, the γ-GRIP contains additional β strands, with the unmodeled features likely representing one of the predicted short β strands (**Figure S5D**). Among the three trimeric complexes resolved thus far, only αβγ_{6WTH} displays a unique γ-GRIP conformation. The γ-GRIP of αβγ_{6WTH} extends approximately 10 Å further towards the C-terminal end of α2 compared to the γ-GRIP of δβγ_{CYS} and ββγ_{CYS} (**Figure S5C**). While our observation is limited to a portion of the γ-GRIP within the context of the ENaC trimeric assemblies, functional data from prior studies have indicated differences between δβγ and αβγ. Specifically, the γ-GRIP in γ-αβγ exhibits sensitivity to proteases,

whereas that in γ-δβγ does not (Wichmann et al., 2018). Additionally, our study unveils contrasting reactions of δβγ and αβγ to 100 μM Zn^{2+} (**Figure 1A-B**). Previous investigations into the influence of Zn^{2+} on αβγ activity have highlighted binding sites in the γ finger, GRIP, and palm domains (Chen et al., 2012; Sheng et al., 2004). Specifically, histidines in the γ-GRIP of αβγ were implicated in mediating the stimulatory Zn^{2+} site. These sites are currently not resolved in any of the cryo-EM maps (Noreng et al., 2020, 2018).

Furthermore, the lack of structural information in the pore domain limits our understanding of how differences in each subunit could lead to overall structural rearrangements in the extracellular domain. While we can utilize predicted pore domain structures from AlphaFold, regions with high confidence scores show minimal conformational differences. The most significant conformational differences are predicted in TM2 and the pre-TM1 region, where the TM2 helices of δ and β^1 are rotated by approximately 10° and 14°, respectively, relative to that of α. This predicted conformational change in ββγ could be attributed to a helical structure in β^1 that might displace the TM2 helix. However, this interpretation should be approached with caution, as AlphaFold assigns low confidence scores to this region (**Figure S5E**). Nevertheless, the distinct positions of the finger domain of γ and differences in map features in the GRIP segment between δβγCYS and αβγ6WTH offer insights into how these heteromeric complexes could manifest divergent functional responses to various stimuli.

The β subunit as a structural scaffold

The superposition of the trimers demonstrated positional differences in the gating domains, which are most discernible in position 1 (**Table S2**). We took advantage of the

uniform conformation of the β subunits in position 2 and used them as references for aligning the trimers to precisely pinpoint how the subunits in position 1 and 3 rearrange in relation to position 2. This allowed us to effectively identify sites that consist structural variability within both position 1 and 3 (**Table S2**). For clarity and to distinguish between the two ends of the finger domain, we adopted the conventions of (+) and (-). We designated the region of the finger domain making extensive contacts with the thumb as the "+" end and the area interacting with the neighboring knuckle domain as the "-" end (**Figure 6A**). We observed the most significant differences in position 1, especially when comparing the δ and β^1 domains with the α subunit. While δ and β^1 have differences in helical positions comprising primarily of rotational components, it is when comparing these subunits with α that striking differences are observed (**Figure 6B**). The finger and thumb helices of δ and β^1—α1, α2, α3, and α4—sit higher than those of α, and exhibit a rotation relative to α, with the "-" end acting as the pivot point (**Figure 6C, D**). Consequently, the "+" end exhibits the greatest difference in position. Interacting with the "+" end, the thumb domain positions of δ and β^1 are also different compared to α. These distinct domain placements can be summarized by determining the position of the centers of mass of the helical components of the finger and thumb domains from each subunit. The resulting position is located beneath α2. A comparison of these positions shows that the greatest difference is between α and β^1, with a distance of 5 Å (**Figure 6B-D**). While the "+" region of the finger in δ and β^1 shows the greatest variation in position, the corresponding areas in position 3 remain stationary (**Figure 6B-D**). Instead, it is the "-" end of the finger domain that demonstrates the largest positional difference, rotating away

from the protein core, akin to observations seen when individual subunits are superimposed (**Figure 5**).

Overall, each position within the trimer serves distinct structural roles. The subunit in position 1 influences the overall conformation of the trimer while the position 2 β subunit acts as a structural scaffold. The larger differences of domain positions observed in position 1 likely contribute to the functional differences observed in electrophysiological experiments. Position 3, occupied by the γ subunit, comprises two regions: one anchored by its interaction with the position 2 β subunit, and another adapting to the subunit at position 1 (**Figure 6A**).

The structural rigidity seen in β^2 subunits is mirrored in the β^1 subunit, showing a remarkably similar conformation. Although there are minor distinctions between them, the overall resemblance is striking (**Figure 6E**). While subtle changes were identified in the finger domain, the most observable change is in the α5 thumb domain helix (**Figure 6F**). Here, the middle segment of the helix is rotated by approximately 9°, while its N- and C-termini remain fixed, establishing connections with the α4 and finger domain at the N-terminal end, and the wrist region at the C-terminal end.

We observed small rigid-body rearrangements in the palm domains of β^1 and β^2. However, the most striking observation near the lower palm domain is a feature resembling a peptide. This molecule wraps around β^1 and forms multiple contacts with β^2 (**Figure 6G, S6A, and S6B**). Due to limitations in map quality, we cannot fully trace this new feature. However, when we examined similar regions in $\delta\beta\gamma_{CYS}$ and $\alpha\beta\gamma_{6WTH}$, we found that $\delta\beta\gamma_{CYS}$ contained a smaller but similar feature, while $\alpha\beta\gamma_{6WTH}$ showed no equivalent feature near the lower palm domain (**Figure 6H, I**). The presence of this

peptide-like feature in both $\delta\beta\gamma_{CYS}$ and $\beta\beta\gamma_{CYS}$ could partly explain the conformational differences observed in these trimers compared to $\alpha\beta\gamma_{6WTH}$. The location of this molecule is strategic as it binds in the lower palm domain poised to influence the arrangement of β strands connected to the transmembrane helices. Further research is required to identify the molecule and to characterize its role in ENaC function.

To test whether the ββγ trimer could contribute to the Na^+ currents we recorded from δβγ-expressing HEK293 cells, we infected cells with a construct containing only β and γ (**Figure 1C, E-G**). We did not detect meaningful amiloride-sensitive currents (**Figure S6C)**. These infected cells behaved similarly to uninfected HEK293 cells (**Figure S6D**). Immunofluorescence light microscopy experiments that leverage our 10d4 antibody aligned with our electrophysiology data demonstrating no surface expression when only β and γ were expressed in HEK cells (**Figure S6E, F**). This confirms that previously described amiloride-sensitive currents were solely a reflection of δβγ activity (**Figure 1C, E-G**). While it has been reported that oocytes injected with β and γ elicit measurable currents, the physiological relevance of ββγ heterotrimers remains to be determined(Baldin et al., 2020).

The βγ dimer provides structural insight into ENaC assembly

Functional and biochemical examinations into ENaC processing have shed light on the specific pathways taken during ENaC protein expression (de la Rosa et al., 2002; Frindt et al., 2008; Hager et al., 2001; Loffing et al., 2000; Masilamani et al., 1999; May et al., 1997). Studies have shown that ENaC subunits are present in both immature and mature forms, distinguished by observed glycosylation patterns (de la Rosa et al., 2002; Hughey et al., 2003). Furthermore, it is also known that despite abundant ENaC

expression, only a small fraction reaches the plasma membrane (Frindt et al., 2022). However, the precise oligomeric assembly of ENaC when it resides intracellularly remains elusive. We identified a complex within the earlier eluted peak, pop1, which does not assemble as a trimer (**Figure 1B**). Upon closer examination of pop1 from $\delta\beta\gamma_{WT}$ by cryo-EM, it became evident that its larger size by FSEC compared to the trimers is attributed to the presence of two βγ dimers interacting via the γ subunit, with each β subunit associated with one 10d4 Fab (**Figure 7A**). The dimer-dimer complex lacks a subunit in position 1 (**Figure 7B**). Instead, the space is partially occupied by the γ subunit belonging to the neighboring dimer. The interdimer contact between the two γ subunits is mediated by a segment not observed in any of the trimers—$\alpha\beta\gamma_{6WTH}$, $\delta\beta\gamma_{CYS}$, and $\beta\beta\gamma_{CYS}$—likely because this region is no longer stabilized when assembled in a trimer. Close inspection of this region revealed that the features emanate from each γ-GRIP and resemble stretches of β strands. These long β strands from both γ-GRIP interlock stabilizing the dimer-dimer interface (**Figure 7A**). Drawing the putative membrane bilayer plane based on the micelle position and the extracellular domain of the two dimers indicates that the planes are not parallel. This suggests that the dimer-dimer complex is unlikely to interact in this configuration if embedded in the membrane, and the observed interaction might be an artifact resulting from sample concentration before grid preparation. However, the presence of the βγ dimer indicates that two ENaC subunits can assemble and remain together even without a third subunit.

The βγ dimer provides an opportunity to investigate assembly in ENaC. Although there appears to be a loop emanating from the γ GRIP domain that could obstruct access to position 1, we speculate that this loop is present in our data primarily because it is

stabilized by its interaction with the second βγ dimer. Assuming this loop is flexible and can move aside when a position 1 subunit joins to form the trimer, we focused on one dimer for the rest of the structural analysis. Implementing symmetry expansion to enhance map quality of one dimer, βγ, we achieved a reported resolution of 3.7 Å (**Figure S7**). The map quality improvement enabled us to trace the main chain in regions that were previously unmodeled in the γ-GRIP domain (**S7C**). Using this model, we measured the distance between the β and γ Cα TriTrp, and this distance was approximately 53.5 Å, which is longer than the distances measured in the $\alpha\beta\gamma_{6WTH}$ and $\beta\beta\gamma_{CYS}$ trimers but slightly shorter than the $\delta\beta\gamma_{CYS}$ (**Figures 7C, D, and 3A-C**). This suggests that to accommodate a subunit in position 1, the γ finger must rearrange (**Figure 3A**). We tested this hypothesis by aligning the position 2 β subunits of all trimers and the βγ dimer and compared the positions of the finger and thumb domains of γ. We found that the finger and thumb domains of γ subunits from all three trimers adopt different positions when compared to the γ-βγ. With a calculated RMSD of 6 Å, the finger and thumb of γ-$\alpha\beta\gamma_{6WTH}$ are most different from γ-βγ (**Figure 7E**).

Examining the three trimers has allowed us to measure the conformational changes the γ subunit undergoes to accommodate various subunits in position 1. The predominant conformational shifts occurring in the finger domain suggest that, while not as rigid as β, γ in position 3 accommodates α, β, and δ subunits. It is worth noting that the pore and cytosolic domains may also influence subunit stoichiometry and trimer conformation. However, the lack of information in these areas limits our understanding of their impact on trimeric assembly. Nevertheless, the observed trimers and dimer

complexes in our study offer valuable structural insights into the diverse assemblies of ENaC.

Main Figures

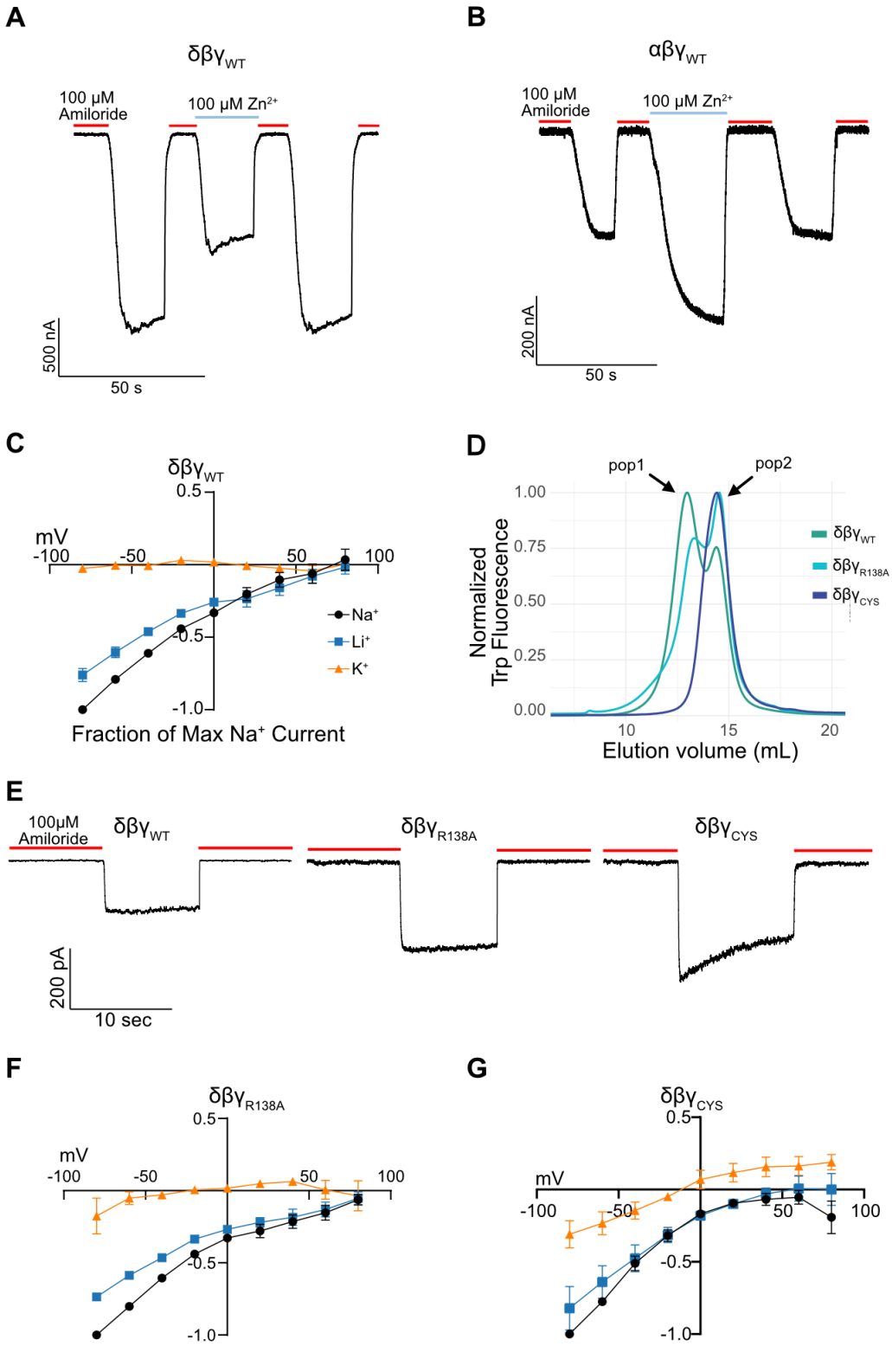

Figure 1. Functional and biochemical characterization of the δβγ complex.

A, B. Representative traces of δβγ (A) and αβγ (B) with and without 100 μM Zn^{2+}. The red and blue lines indicate application of 100 μM amiloride and 100 μM Zn^{2+}, respectively. **C.** Current-voltage experiment in HEK293 cells demonstrating that $\delta\beta\gamma_{WT}$ is Na^+-selective, permeable to Li^+ and impermeable to K^+. Voltage potential range used for the experiment is -80 mV to 80 mV in 20 mV increments. The external solutions contained equimolar concentration of Na^+, Li^+, and K^+. Internal solution contained K^+. Each point is represented as mean ± SEM (n = 7). **D.** Normalized FSEC traces of purified $\delta\beta\gamma_{WT}$, $\delta\beta\gamma_{R138A}$, and $\delta\beta\gamma_{CYS}$ monitored on the tryptophan fluorescence channel. Traces were normalized to the height of the peak at 14 mL. **E.** Representative current traces of $\delta\beta\gamma_{WT}$, $\delta\beta\gamma_{R138A}$, and $\delta\beta\gamma_{CYS}$ expressed in HEK cells and in whole-cell patch-clamp experiments. Holding potential at -60 mV. **F, G.** Current-voltage experiments of $\delta\beta\gamma_{R138A}$ (F) and $\delta\beta\gamma_{CYS}$ (G) using the same conditions in C. Data are represented as mean SEM (n = 5 for $\delta\beta\gamma_{R138A}$ and n=5 for $\delta\beta\gamma_{CYS}$).

See also Figure S1.

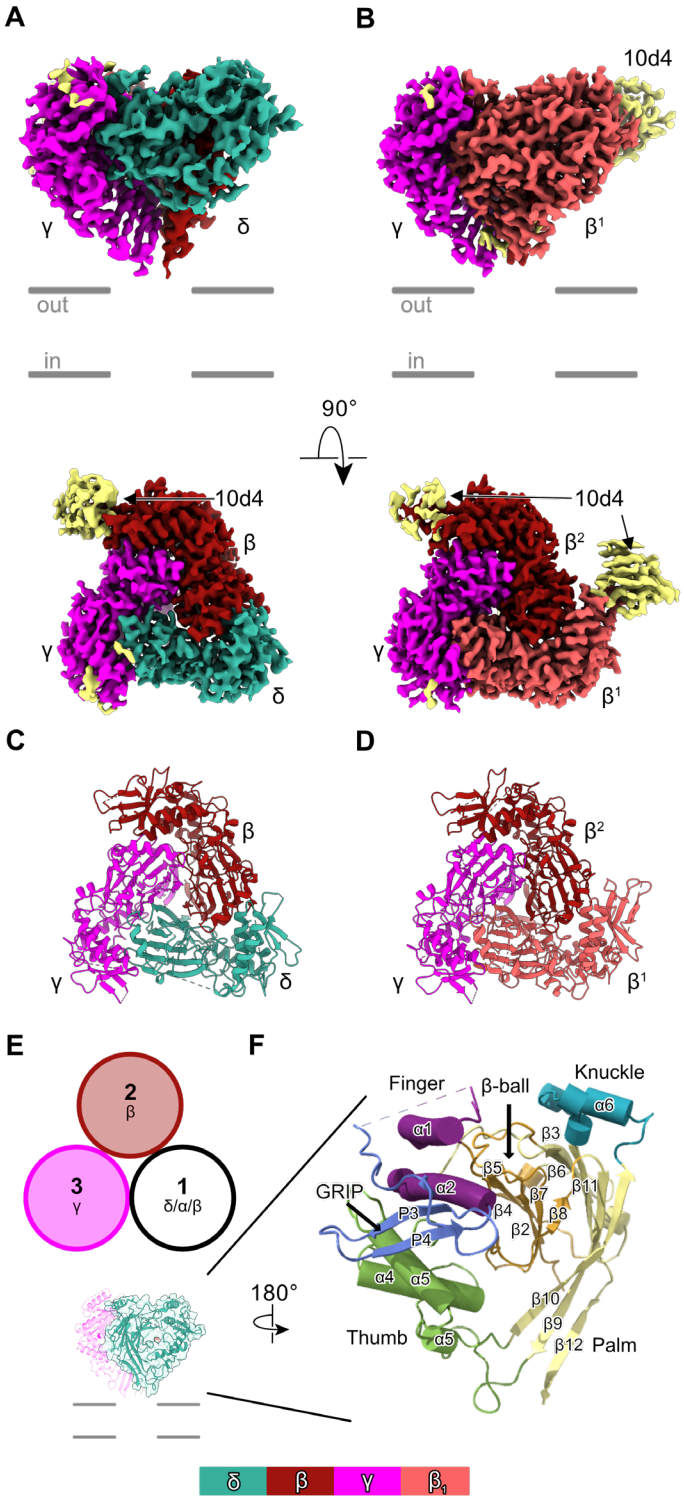
A
B
10d4
γ
δ
β¹
out
in
90°
10d4
β
β²
γ
δ
β¹
C
D
β
β²
γ
δ
γ
β¹
E
F
2
β
3
γ
1
δ/α/β
180°
Finger
β-ball
Knuckle
α6
α1
β3
β5
β6
β11
GRIP
α2
β7
P3
β4
β8
β2
P4
α4
α5
β10
β9
Thumb
α5
β12
Palm
δ
β
γ
β₁

Figure 2. Cryo-EM analysis reveal two different heteromeric complexes.

A. Cryo-EM map of the extracellular domain of $\delta\beta\gamma_{CYS}$ viewed parallel and perpendicular to the membrane plane viewed from the extracellular side, and in surface representation. The subunits δ, β, and γ are colored teal, red, and magenta, respectively. The 10d4 Fab bound to the β subunit and other unmodeled densities are colored yellow. **B.** Cryo-EM map of $\beta\beta\gamma_{CYS}$ viewed similarly as in A. The β^1 subunit is colored salmon. Only a small segment of the 10d4 Fab, colored yellow, is resolved after local refinement. **C, D.** The models of the extracellular domains of $\delta\beta\gamma_{CYS}$ (A) and $\beta\beta\gamma_{CYS}$ (B) viewed from the extracellular side and down the pore axis. They are in cartoon representation and colored as in Figure 2A and B **E.** Schematic illustration viewed from the extracellular side and looking down the pore axis of the three positions of the subunits in ENaC denoted as positions 1, 2, and 3. **F.** Inset: An overall view of the $\delta\beta\gamma_{CYS}$ extracellular domain in cartoon representation. The close-up view of δ is rotated 180° relative to the view in the inset. The δ subunit follows a similar architecture as other ENaC subunits consisting of domains arranged like a hand grasping a ball. The unique domain first characterized in the human αβγ structure, the GRIP domain colored blue, is conserved in δ. The knuckle, finger, thumb, palm, and β-ball are colored cyan, purple, green, yellow, and orange, respectively.

See also Figure S2.

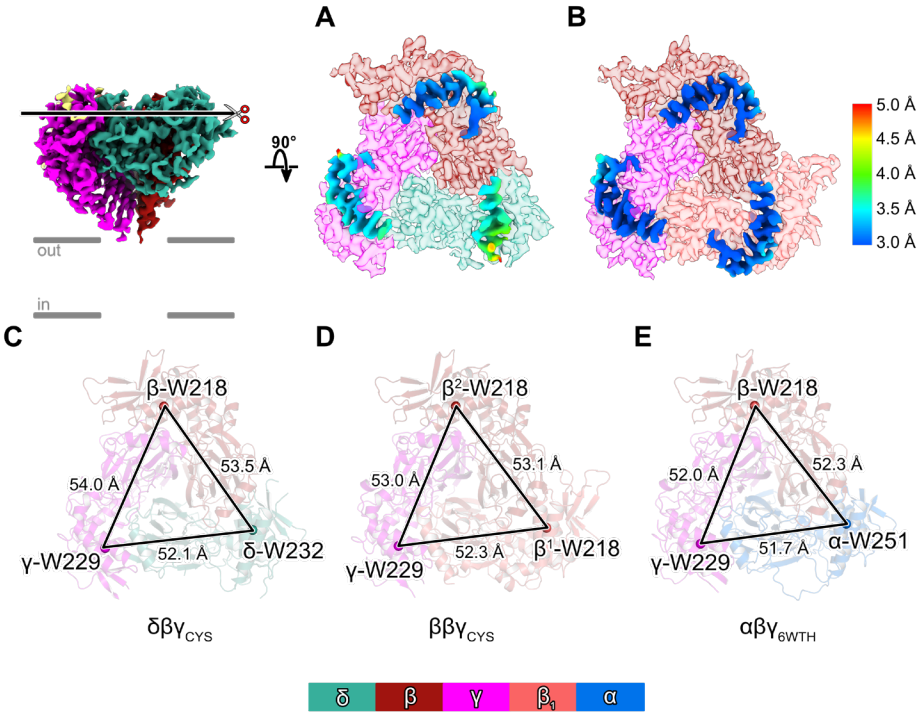

Figure 3. Position 1 subunit mediates changes in the extracellular domain

A, B. Cryo-EM maps of $\delta\beta\gamma_{CYS}$ (A) and $\beta\beta\gamma_{CYS}$ (B) showing the position and local map resolution of α2 helices, which include the tryptophans forming the TriTrp triangle. Only the α2 helix map features are shown and colored according to the estimated local resolution. The rest of the map features are colored as in Figure 2. For clarity, the knuckle and α1 helices are removed in the views looking down the pore axis. **C-E.** Comparison of the extracellular domains of $\delta\beta\gamma_{CYS}$ (C), $\beta\beta\gamma_{CYS}$ (D), and αβγ (E, PDB: 6WTH). The Cα positions of the tryptophans belonging to the TriTrp are shown as spheres. The distances between the Cα atoms are shown in Å.

See also Figure S3.

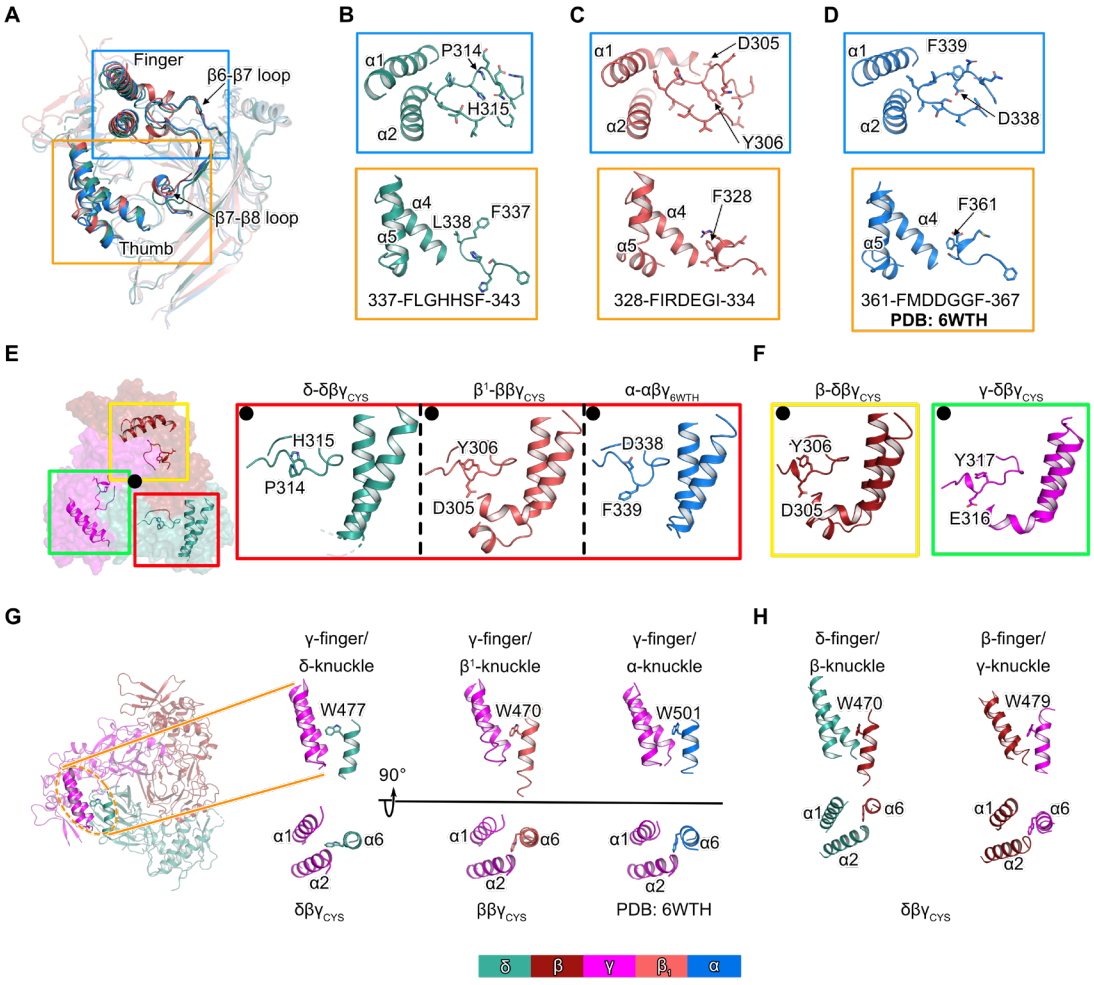
A
Finger
β6-β7 loop
β7-β8 loop
Thumb
B
α1
P314
H315
α2
α4
L338
F337
α5
337-FLGHHSF-343
C
α1
D305
α2
Y306
F328
α4
α5
328-FIRDEGI-334
D
α1
F339
α2
D338
F361
α4
α5
361-FMDDGGF-367
PDB: 6WTH
E
δ-δβγCYS
β1-ββγCYS
α-αβγ6WTH
H315
P314
Y306
D305
D338
F339
F
β-δβγCYS
γ-δβγCYS
Y306
D305
Y317
E316
G
γ-finger/
δ-knuckle
γ-finger/
β1-knuckle
γ-finger/
α-knuckle
W477
W470
W501
90°
α1
α6
α2
δβγCYS
ββγCYS
PDB: 6WTH
H
δ-finger/
β-knuckle
β-finger/
γ-knuckle
W470
W479
α1
α6
α2
δβγCYS
δ
β
γ
β1
α

Figure 4. Unique conformational features in δ contribute to changes in the extracellular domains.

A. Superposition of all position 1 subunits show differences in the finger and β-ball domains. The δ, β^1, and α are colored teal, salmon, and blue. The subunits are shown in cartoon representation. **B-D.** Close-up view of boxed regions in A belonging to δ (B), β^1 (C), and α (D). The sidechains of β6-β7 and β7-β8 loop residues are shown in sticks representation. A 7-residue segment of the β7-β8 loop is shown along with the corresponding sequence. **E.** View looking down the pore axis to show relative positions of the finger domains in positions 1-3. The close-up views of the boxed area in position 1 are displayed. The sidechains of residues at corresponding positions in δ, β1, and α are depicted in stick form to illustrate the orientation of their side chains. The black dot marks the relative direction of the pore axis position. **F.** Close-up views of the boxed regions in E of positions 2 and 3 in the $\delta\beta\gamma_{CYS}$ structure. The views are rotated ~120° clockwise (yellow) or counterclockwise (green) relative to the panels in E highlighted with a red box. **G.** Illustration of the position 1/position 3 interface focusing on the knuckle/finger domain contacts. Only the sidechain of the conserved tryptophan in the knuckle domain is displayed in stick form while the rest of the region is shown in cartoon. **H.** Equivalent interfaces in position 1/position 2 and position 2/position 3 in $\delta\beta\gamma_{CYS}$ are shown and represented similarly as in G.

See also Figure S4.

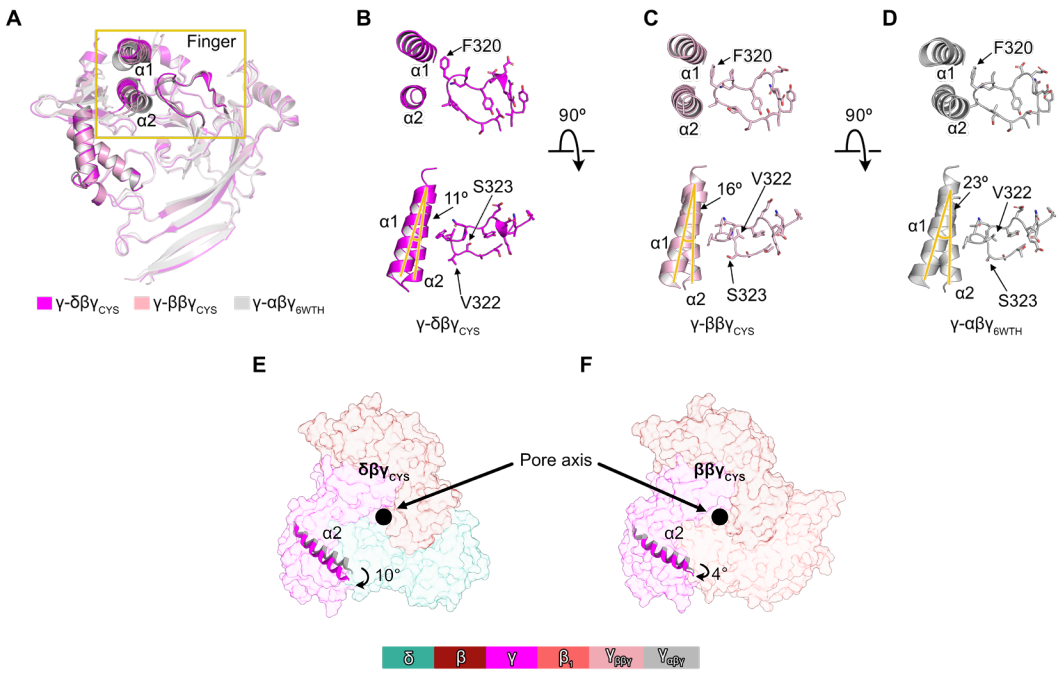

Figure 5. The γ finger domain is altered in the presence of δ.

A. Superposition of all γ subunits in position 3 from the three trimers. The subunits are displayed in cartoon representation and colored magenta ($\delta\beta\gamma_{CYS}$), light pink ($\beta\beta\gamma_{CYS}$), and gray ($\alpha\beta\gamma_{6WTH}$). **B-D.** Close-up views of the boxed region in A. The sidechains of residues in β6-β7 loop in the finger domain are shown in stick form to demonstrate the positions of the side chains. **E, F.** Surface representation of the $\delta\beta\gamma_{CYS}$ (E) and $\beta\beta\gamma_{CYS}$ (F) models is shown. The positions of the γ-α2 helices in $\delta\beta\gamma_{CYS}$ and $\beta\beta\gamma_{CYS}$ relative to those of $\alpha\beta\gamma_{6WTH}$ are displayed.

See also Figure S5.

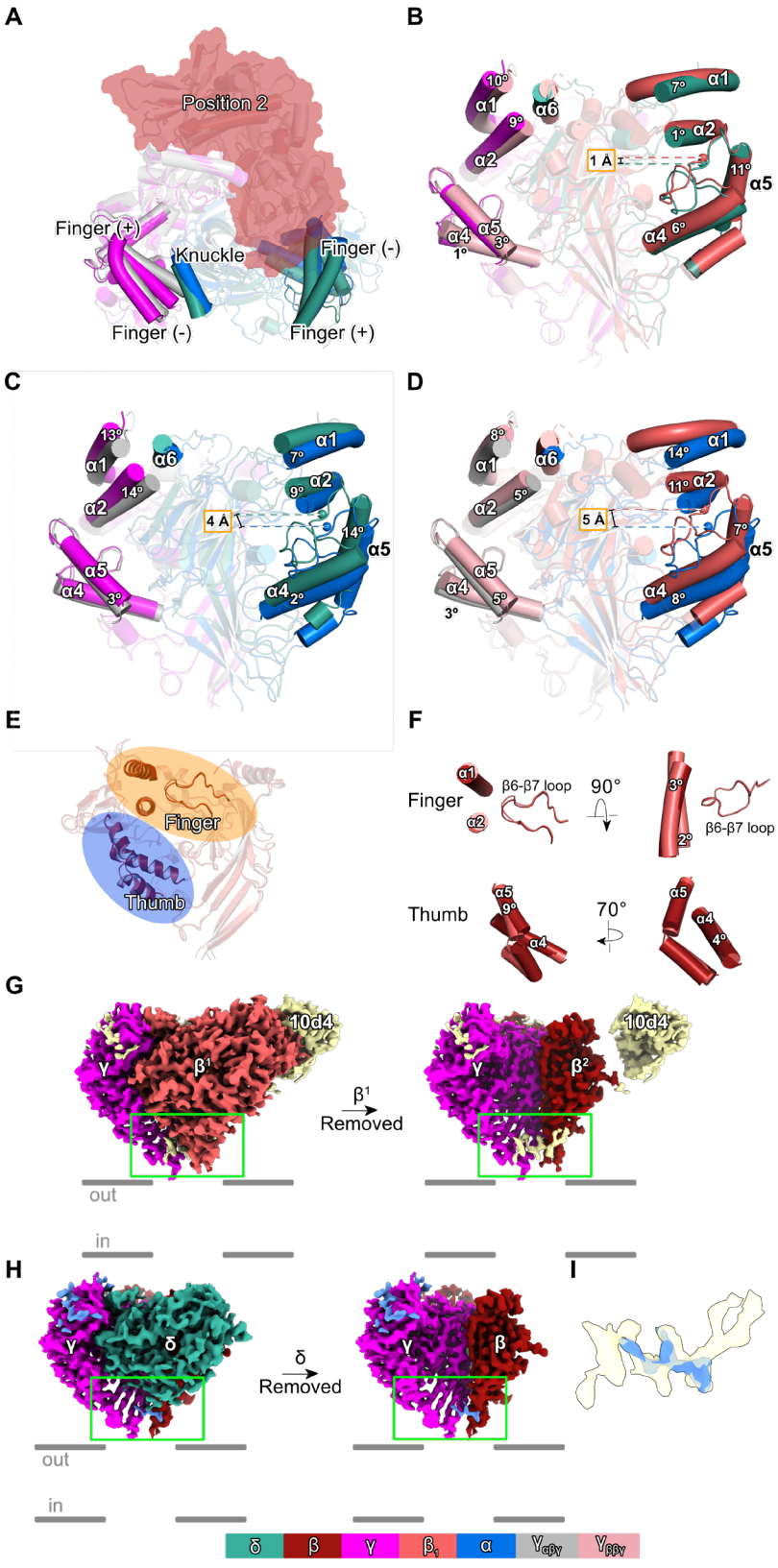
A
Position 2
Finger (+)
Knuckle
Finger (-)
Finger (-)
Finger (+)
B
10°
α1
7°
α1
α6
9°
1°
α2
α2
1 Å
11°
α5
α4
α5
3°
α4
6°
1°
C
13°
α1
α1
7°
α6
α2
9°
α2
14°
4 Å
14°
α5
α5
α4
3°
α4
2°
D
8°
α1
α1
14°
α6
11°
α2
α2
5°
5 Å
7°
α5
α5
α4
5°
α4
8°
3°
E
Finger
Thumb
F
Finger
α1
β6-β7 loop
90°
3°
2°
β6-β7 loop
α2
Thumb
α5
9°
70°
α5
α4
α4
4°
G
10d4
γ
β1
β1
Removed
10d4
γ
β2
out
in
H
I
γ
δ
δ
Removed
γ
β
out
in
δ
β
γ
β1
α
Vαβγ
Vββγ

Figure 6. Trimer superpositions using the β subunit in position 2 as reference reveal global rearrangements in position 1.

A. View looking down the pore axis from the extracellular side. The $\delta\beta\gamma_{CYS}$ and $\alpha\beta\gamma_{6WTH}$ trimers are shown in cartoon and subunits are colored as in figures 4 and 5. The helices are shown as cylinders. The β subunit occupying position 2 is colored red. The knuckle, finger, and thumb are opaque while the rest of the extracellular domains are transparent for clarity. **B-D.** Comparison of the finger and thumb domains of position 1 and 3 subunits in $\delta\beta\gamma_{CYS}$ vs $\beta\beta\gamma_{CYS}$ (B), $\delta\beta\gamma_{CYS}$ vs $\alpha\beta\gamma_{6WTH}$ (C), and $\beta\beta\gamma_{CYS}$ vs $\alpha\beta\gamma_{6WTH}$ (D). The β subunit in position 2 is omitted for clarity. The centers of mass of the finger and thumb domain helices, calculated using Pymol, are represented as spheres. The solid bars indicate the distances between the centers of mass. Angle between corresponding helices of the finger and thumb domains are shown. **E.** Overlay of β^1 and β^2 subunits in cartoon representation. **F.** Close-up views of the finger and thumb domains shown in E shown as cylinders. **G, H.** Cryo-EM maps of $\beta\beta\gamma_{CYS}$ (G) and $\delta\beta\gamma_{CYS}$ (H) showing a peptide-like map feature in the palm domain that is not observed in αβγ. Position 1 subunits are removed for clarity (right image). The molecules and other modeled densities in $\beta\beta\gamma_{CYS}$ (G) and $\delta\beta\gamma_{CYS}$ (H) are colored yellow and blue, respectively. **I.** Close-up view and superposition of the features observed in the lower palm domain shown in G and H.

See also Figure S6.

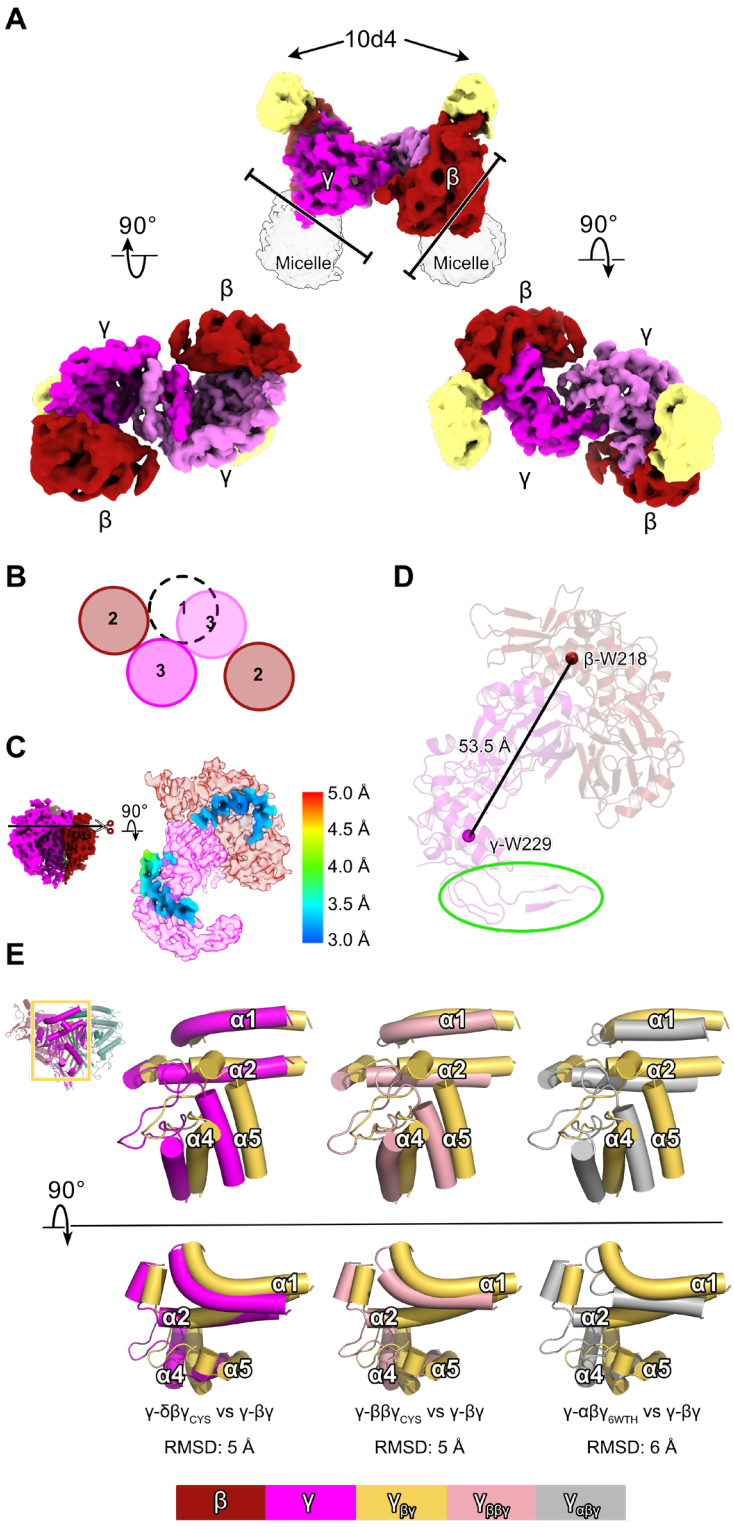
A
10d4
γ
β
Micelle
Micelle
90°
90°
β
γ
γ
β
β
γ
γ
β
B
2
1
3
3
2
C
90°
5.0 Å
4.5 Å
4.0 Å
3.5 Å
3.0 Å
D
β-W218
53.5 Å
γ-W229
E
α1
α2
α4
α5
90°
γ-δβγCYS vs γ-βγ
RMSD: 5 Å
γ-ββγCYS vs γ-βγ
RMSD: 5 Å
γ-αβγ6WTH vs γ-βγ
RMSD: 6 Å
β
γ
γβγ
γββγ
γαβγ

Figure 7. Heteromeric ENaC assembly intermediate shows β and γ assemble as dimers.

A. Cryo-EM map of the βγ-dimer with subunits and Fab colored as in figure 2. The second γ subunit is colored in light pink for clarity. Solid bars indicate the direction of the putative membrane plane. **B.** Schematic illustration of the dimer-dimer interaction shown in A with the missing position 1 subunit shown as dashed circle. **C.** Close-up view of the α2 helices, which include the tryptophans forming the TriTrp triangle, in the βγ complex. The α2 helix map features are shown as a surface representation and are colored according to the estimated local resolution. **D.** Cartoon representation of the βγ dimer with distances of the Cα atoms of conserved tryptophans in the α2 helices. The highlighted region in green is the γ-GRIP portion that is not resolved in ENaC trimers. This region mediates extensive interdimer contacts. **E.** Inset: An overall view of the $\delta\beta\gamma_{CYS}$ extracellular domain in cartoon representation. The region highlighted with a yellow rectangle includes the finger and thumb domains of γ. Close-up views of the boxed region showing comparison of the α1, α2, α4, and α5 positions in the finger and thumb domains of γ from trimers to the γ from βγ-dimer. The γ from trimers are colored as in figures 4 and 5, while γ from the dimer is colored yellow. All helices are shown in cylinders.

See also Figure S7.

Supplementary Figures and Tables

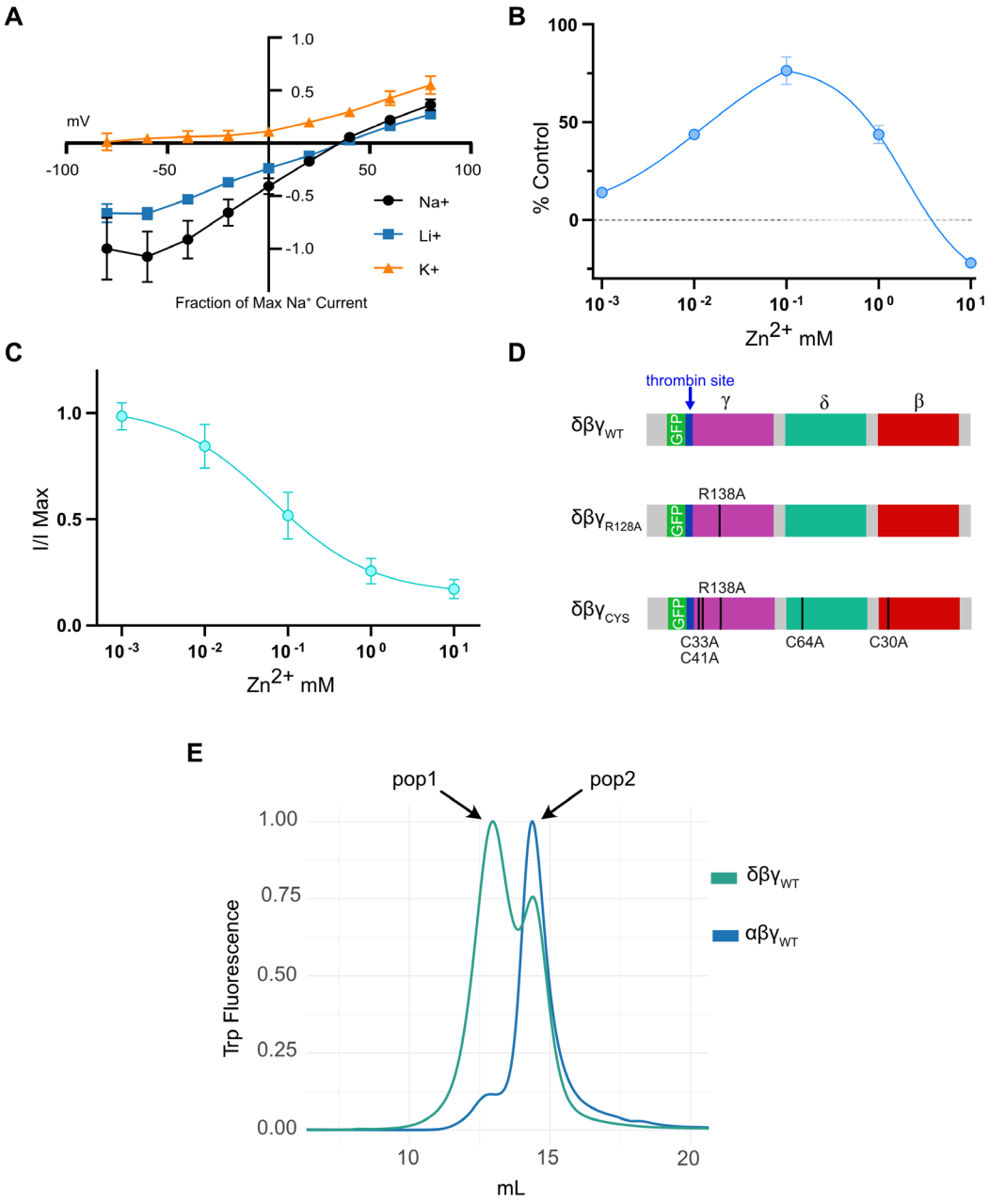

Figure S1. Design and optimization of δβγ constructs for structural investigations by cryo-EM, related to Figure 1.

A. Current-voltage experiment demonstrating that $\delta\beta\gamma_{WT}$ is Na^+-selective, permeable to Li^+, and impermeable to K^+ when expressed in *Xenopus laevis* oocytes. Voltage potential range used for the experiment is -80 mV to 80 mV in 20 mV increments. The external solutions contained equimolar concentration of Na^+, Li^+, and K^+. The pipettes contained 3M KCl. Each point is represented as mean ± SEM (n = 5). **B.** Dose-response of αβγ to Zn^{2+}. Current ratios were determined by measuring current amplitudes before and after application of Zn^{2+}. Data are represented as mean ± SEM (n=3). **C.** Dose-response of δβγ to Zn^{2+} using the same concentration range as in B. Data are represented as mean ± SEM (n=12). **D.** Schematic illustration of the three δβγ constructs: $\delta\beta\gamma_{WT}$, $\delta\beta\gamma_{R138A}$, and $\delta\beta\gamma_{CYS}$. **E.** Normalized FSEC traces comparing the biochemical behavior of purified $\delta\beta\gamma_{WT}$ and $\alpha\beta\gamma_{WT}$. Traces were normalized to the height of the peak at 14 mL.

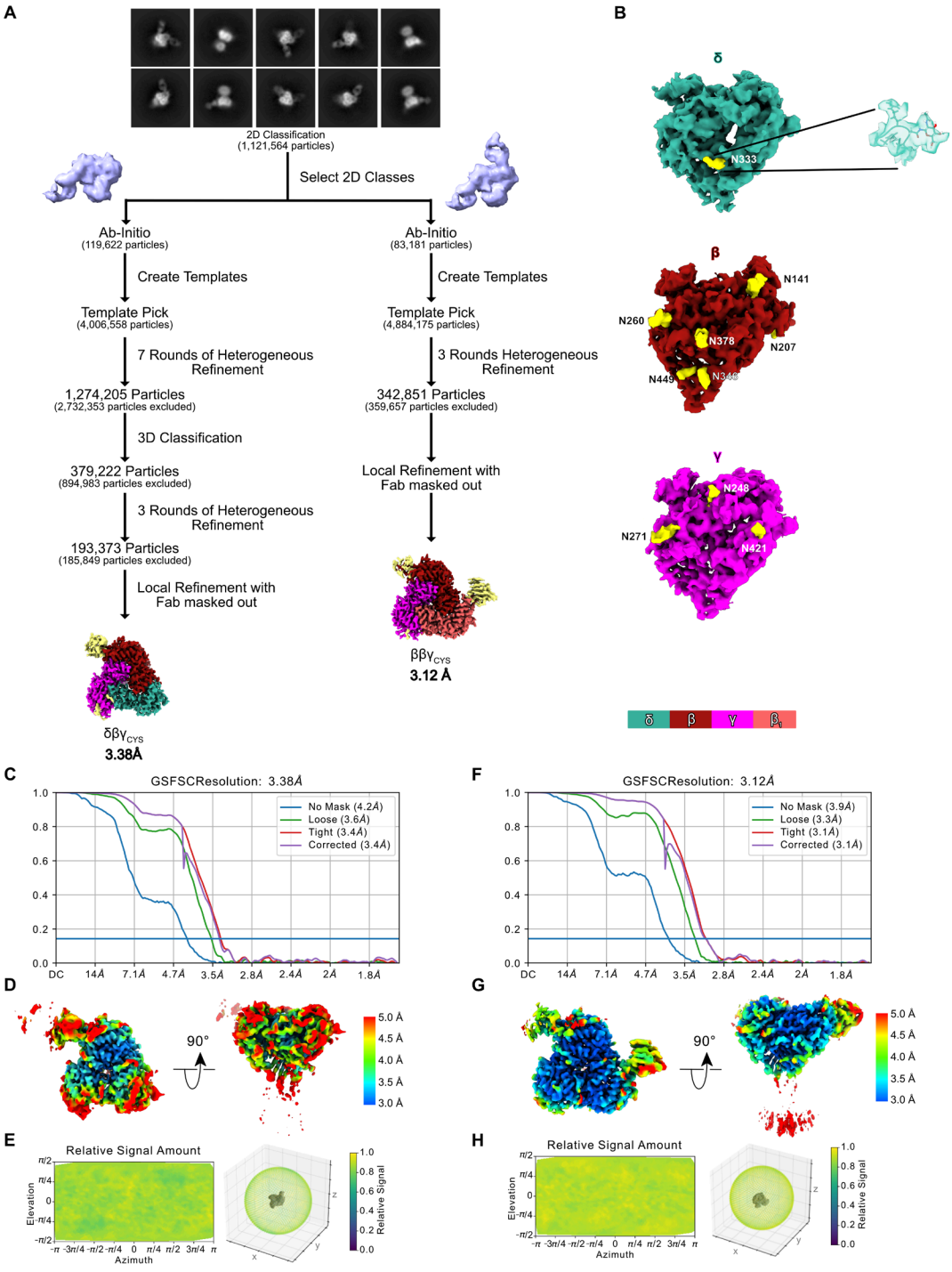
A
2D Classification
(1,121,564 particles)
Select 2D Classes
Ab-Initio
(119,622 particles)
Create Templates
Template Pick
(4,006,558 particles)
7 Rounds of Heterogeneous Refinement
1,274,205 Particles
(2,732,353 particles excluded)
3D Classification
379,222 Particles
(894,983 particles excluded)
3 Rounds of Heterogeneous Refinement
193,373 Particles
(185,849 particles excluded)
Local Refinement with Fab masked out
δβγCYS
3.38Å
Ab-Initio
(83,181 particles)
Create Templates
Template Pick
(4,884,175 particles)
3 Rounds Heterogeneous Refinement
342,851 Particles
(359,657 particles excluded)
Local Refinement with Fab masked out
ββγCYS
3.12 Å
B
δ
N333
β
N141
N260
N378
N207
N449
N348
γ
N248
N271
N421
δ
β
γ
βt
C
GSFSCResolution: 3.38Å
No Mask (4.2Å)
Loose (3.6Å)
Tight (3.4Å)
Corrected (3.4Å)
DC
14Å
7.1Å
4.7Å
3.5Å
2.8Å
2.4Å
2Å
1.8Å
D
90°
5.0 Å
4.5 Å
4.0 Å
3.5 Å
3.0 Å
E
Relative Signal Amount
Elevation
Azimuth
Relative Signal
F
GSFSCResolution: 3.12Å
No Mask (3.9Å)
Loose (3.3Å)
Tight (3.1Å)
Corrected (3.1Å)
G
90°
H
Relative Signal Amount

Figure S2. Three-dimensional reconstruction details of $\delta\beta\gamma_{CYS}$ and $\beta\beta\gamma_{CYS}$, related to Figure 2.

A. Overview of the cryo-EM data processing workflow that revealed two trimeric complexes: $\delta\beta\gamma_{CYS}$ and $\beta\beta\gamma_{CYS}$. **B.** Cryo-EM maps of the subunits in $\delta\beta\gamma_{CYS}$. The glycosylation sites are colored yellow, and the subunits are colored as in Figure 2.

C-H. Fourier Shell Correlation curves, local resolution maps, and angular distribution plots for $\delta\beta\gamma_{CYS}$ and $\beta\beta\gamma_{CYS}$.

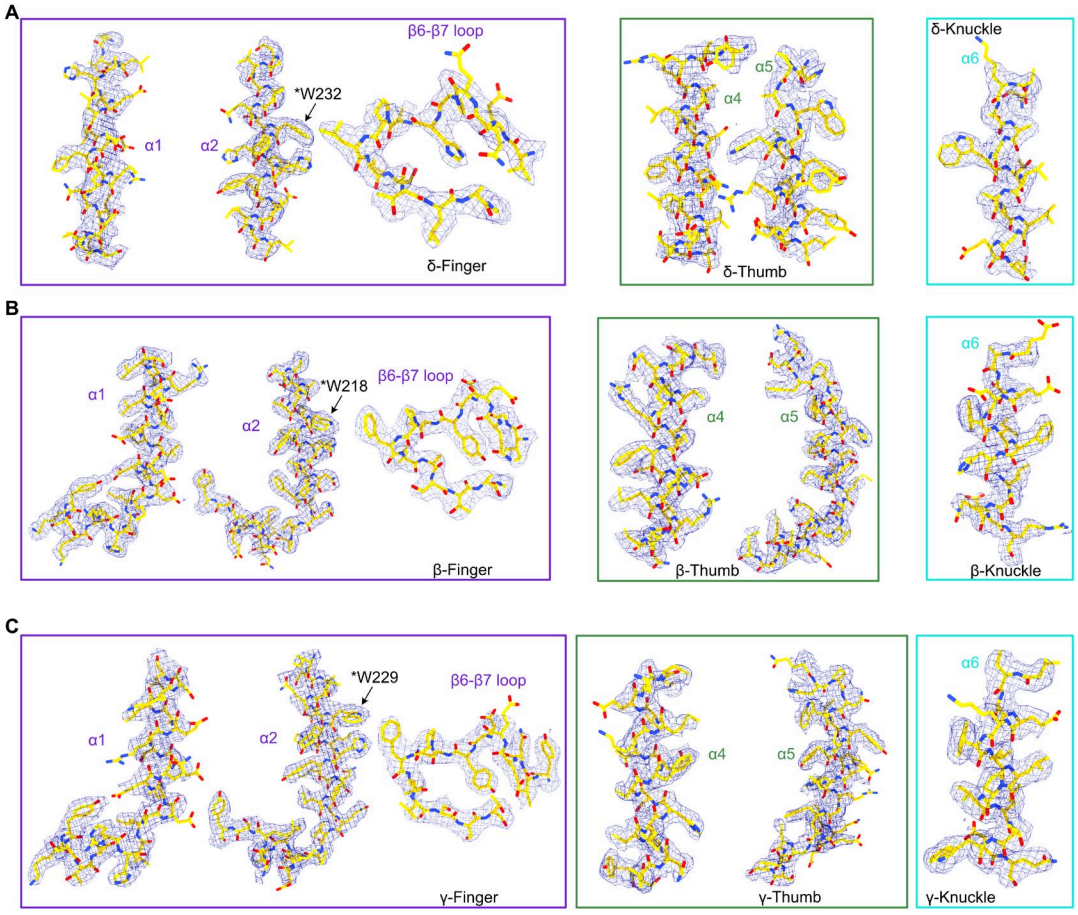

Figure S3. Cryo-EM maps of the gating domains in δβγ$_{CYS}$, related to Figure 3.

A-C. Cryo-EM maps of the finger, thumb, and knuckle domains of δ (A), β (B), and γ (C) subunits and the corresponding models.

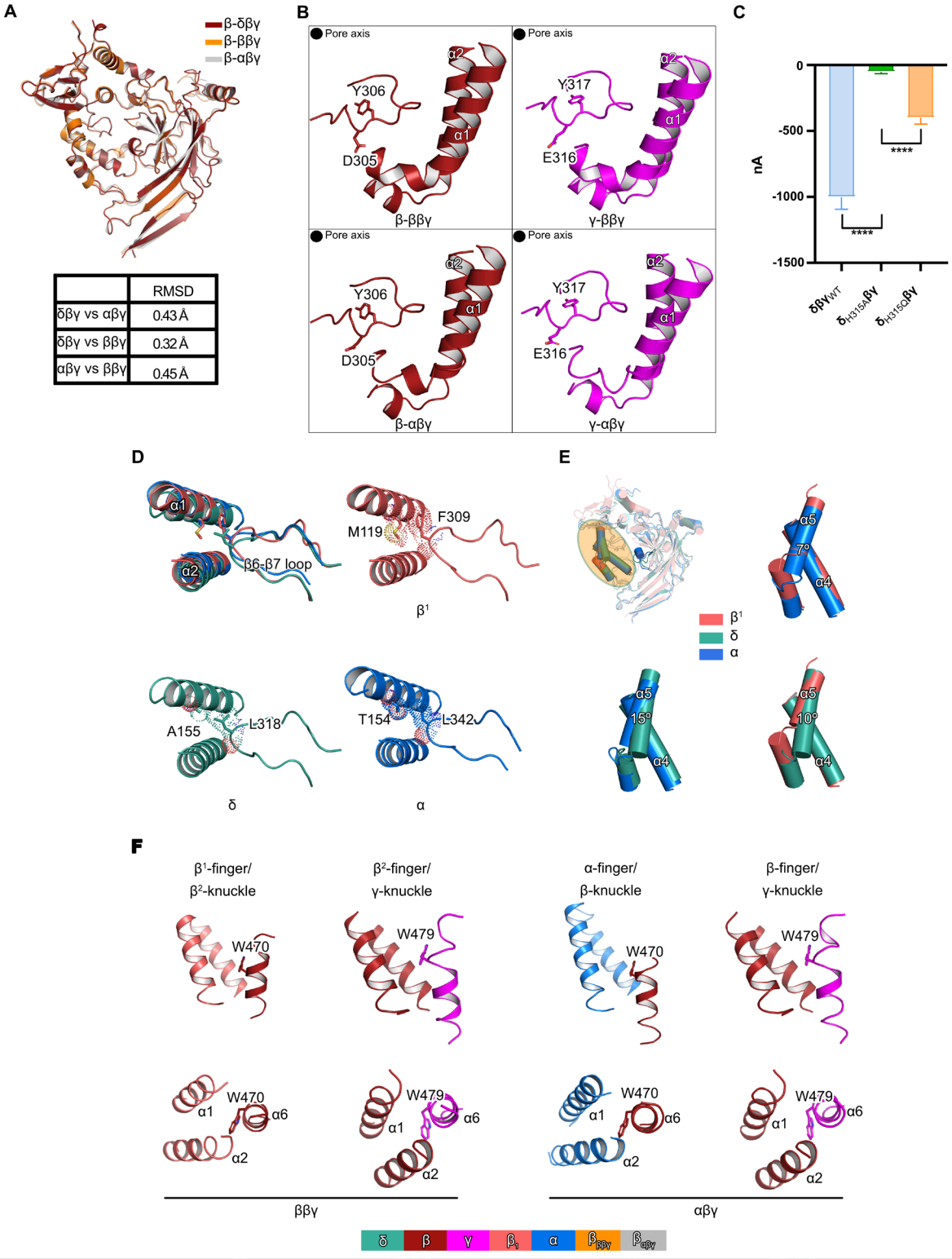

	RMSD
δβγ vs αβγ	0.43 Å
δβγ vs ββγ	0.32 Å
αβγ vs ββγ	0.45 Å

Figure S4. Comparison of the finger, thumb, and knuckle domains and interfaces of subunits, related to Figure 4.

A. Superposition of the β subunits occupying position 2 from $\delta\beta\gamma_{CYS}$, $\beta\beta\gamma_{CYS}$, and $\alpha\beta\gamma_{6WTH}$. **B.** The close-up views of the boxed area in positions 2 and 3 from figure 4E are displayed. Sidechains of residues at corresponding positions in β and γ from $\beta\beta\gamma_{CYS}$ and $\alpha\beta\gamma_{6WTH}$ are shown in stick form to illustrate the orientation of their side chains relative to the pore axis, symbolized as a black circle in the upper left corner of the view. The black circle marks the relative direction of the pore axis position. **C.** Comparison of amiloride sensitive Na^+ current amplitude from $\delta\beta\gamma_{WT}$ (blue, n=17), $\delta\beta\gamma_{H315A}$ (green, n=9), $\delta\beta\gamma_{H315Q}$ (orange, n=10) expressed in *Xenopus* oocytes. ****P<0.0001 determined by unpaired t test, error bars indicate SEM **D.** A view of the finger domain showing residues that form contacts between β6-β7 loop and the helical segments. Sidechains are shown in sticks and dots representation to provide visualization of sidechain packing. **E.** Superposition of the position 1 subunits and comparison of the thumb domains. **F.** Views of the position 1/position 2 and position 2/position 3 interfaces in $\beta\beta\gamma_{CYS}$ and $\alpha\beta\gamma_{6WTH}$.

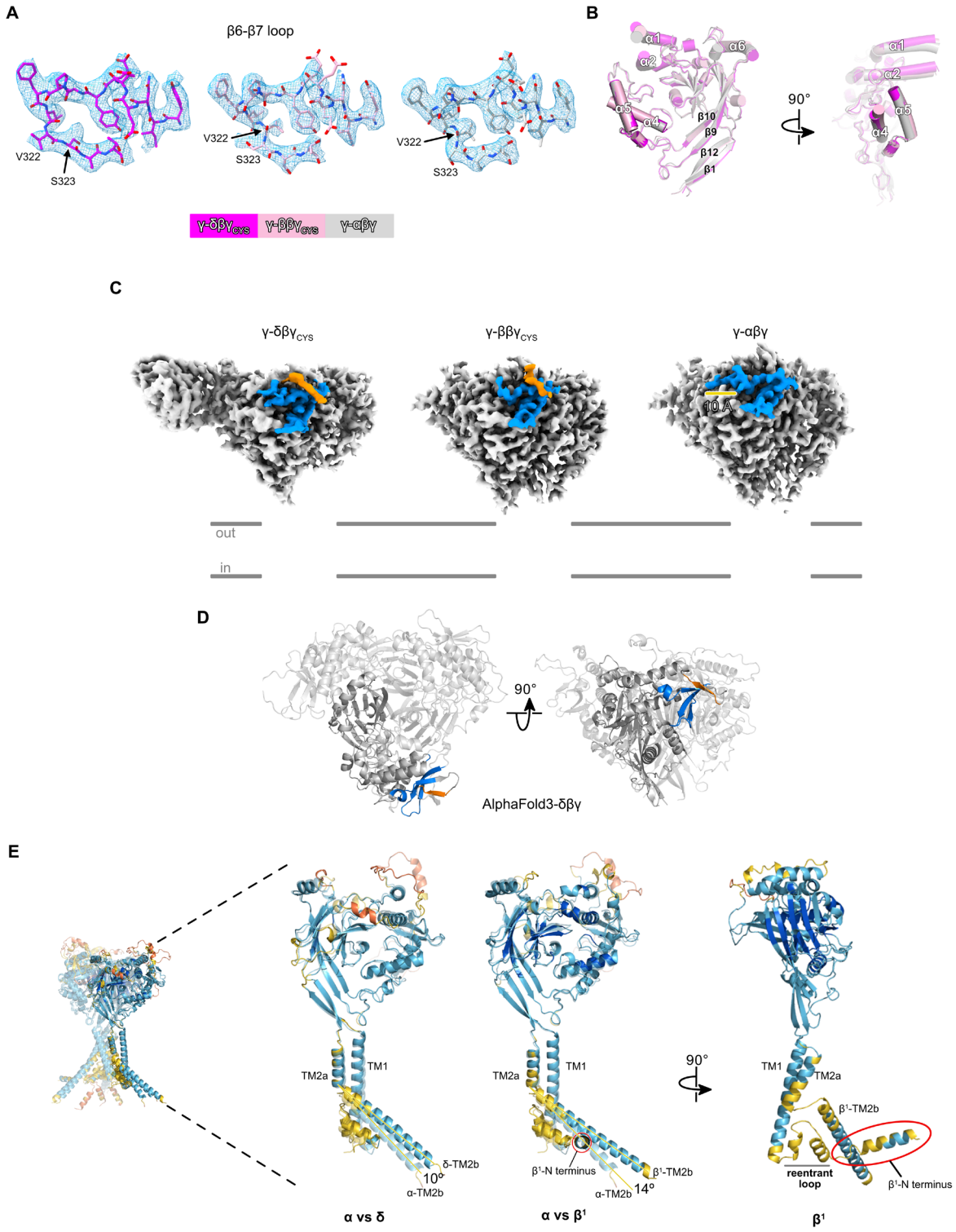
A
β6-β7 loop
V322
S323
V322
S323
V322
S323
γ-δβγCYS
γ-ββγCYS
γ-αβγ
B
α1
α2
α6
α5
α4
β10
β9
β12
β1
90°
α1
α2
α5
α4
C
γ-δβγCYS
γ-ββγCYS
γ-αβγ
10 Å
out
in
D
90°
AlphaFold3-δβγ
E
TM1
TM2a
δ-TM2b
10°
α-TM2b
α vs δ
TM1
TM2a
β¹-N terminus
β¹-TM2b
α-TM2b
14°
α vs β¹
90°
TM1
TM2a
β¹-TM2b
reentrant loop
β¹-N terminus
β¹

Figure S5. The γ subunit finger domain rearranges in the presence of δ and β in position 1, related to Figure 5.

A. Cryo-EM map of the β6-β7 loop in $\delta\beta\gamma_{CYS}$, $\beta\beta\gamma_{CYS}$, and $\alpha\beta\gamma_{6WTH}$ and the corresponding residues. **B.** Superposition of the γ subunits from $\delta\beta\gamma_{CYS}$, $\beta\beta\gamma_{CYS}$, and $\alpha\beta\gamma_{6WTH}$. **C.** Cryo-EM maps of $\delta\beta\gamma_{CYS}$, $\beta\beta\gamma_{CYS}$, and $\alpha\beta\gamma_{6WTH}$. The γ-GRIP domains are colored blue while the rest of the map is shown in gray. The new map features observed in $\delta\beta\gamma_{CYS}$ and $\beta\beta\gamma_{CYS}$ are colored orange. **D.** The model generated by AlphaFold3 for δβγ reveals that the γ-GRIP region consists of several β strands. Among these strands, one positioned close to the upper part of the GRIP segment is likely the novel feature detected in the $\delta\beta\gamma_{CYS}$ and $\beta\beta\gamma_{CYS}$ maps. **E.** AlphaFold3 models show the predicted conformation and positions of the transmembrane domains. The models for position 1 ENaC subunits, α, δ, and β^1 illustrating predicted differences in TM2b between each subunit.

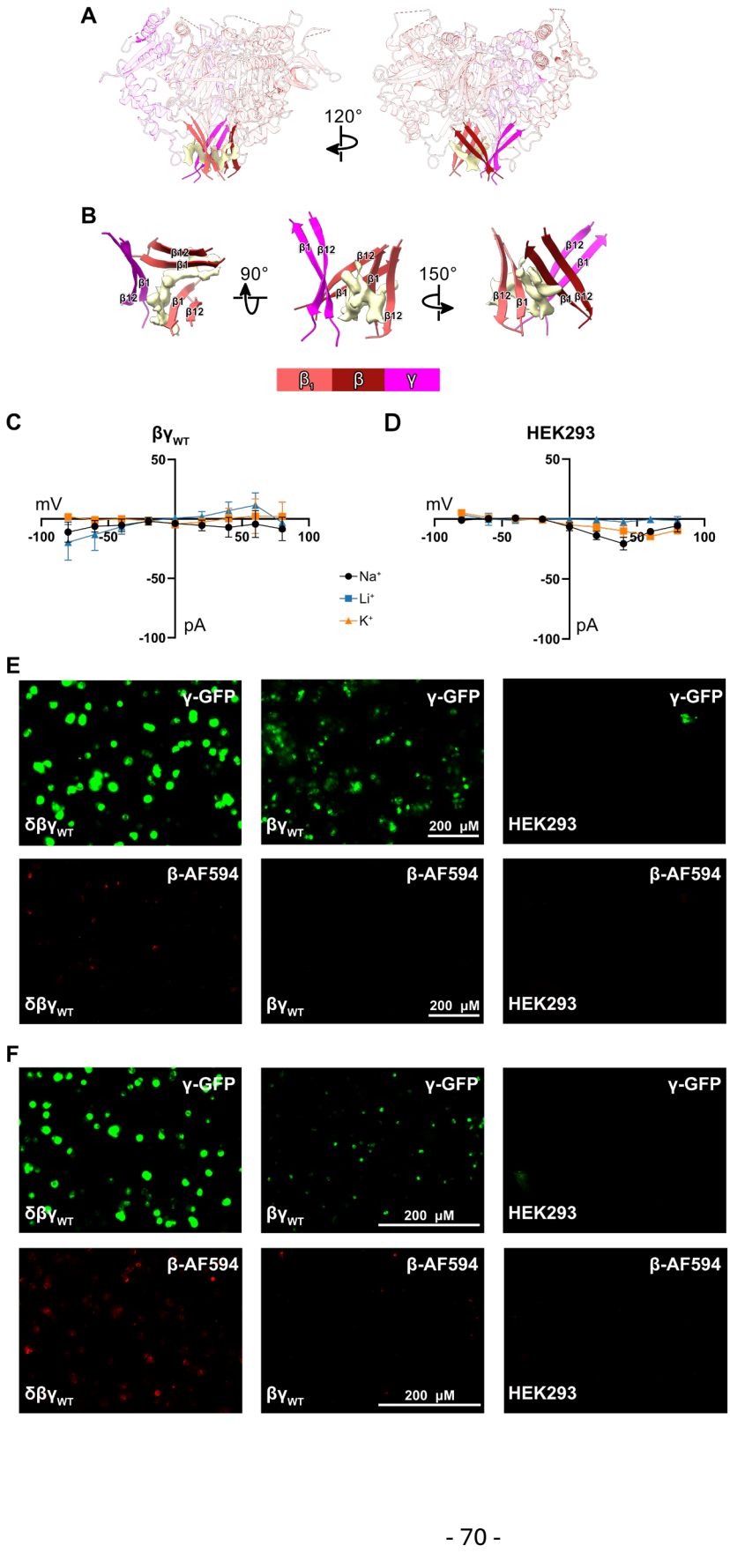
A
120°
B
90°
150°
β12
β1
β
γ
C
βγWT
50
-50
-100
mV
pA
-100
-50
50
100
Na+
Li+
K+
D
HEK293
E
γ-GFP
δβγWT
βγWT
200 μM
HEK293
β-AF594
F

Figure S6. Cryo-EM analysis, functional, and biochemical characterization of $\beta\beta\gamma_{CYS}$, related to Figure 6.

A. Model of $\beta\beta\gamma_{CYS}$. The region forming contacts with the peptide-like feature in the palm domain is highlighted. **B.** Close-up view of the colored region in A. **C, D.** Current-voltage relationship of cells infected with β and γ baculovirus (C) and uninfected cells (D). **E, F.** Immunofluorescence staining of unpermeabilized (E) and permeabilized (F) cells infected with δβγ (left), βγ (middle), or left uninfected (right). Surface expression of ENaC was monitored using the 10d4 monoclonal antibody directed against the β subunit. A secondary antibody labeled with Alexa Fluor 594 was used for fluorescence labeling.

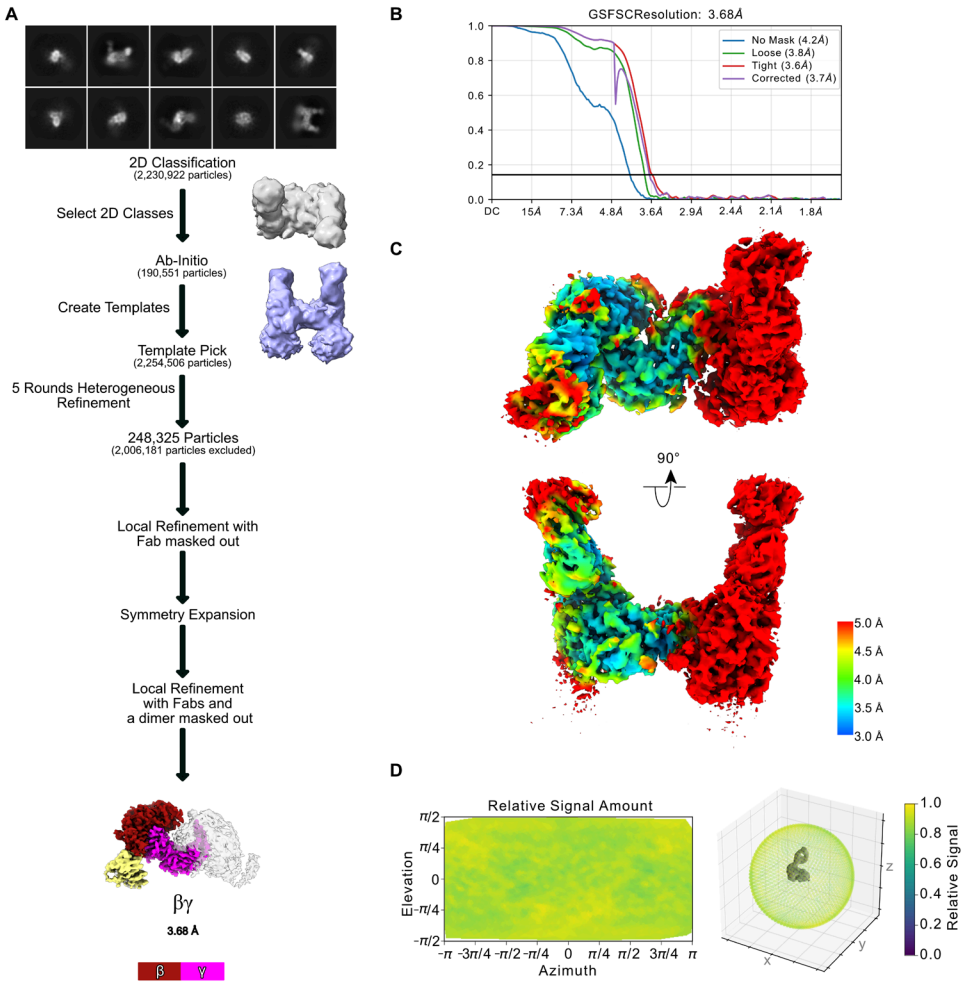

Figure S7. Cryo-EM analysis of the pop1 peak from δβγWT-expressing HEK cells, related to Figure 7.

A. Illustration of the cryo-EM workflow used to generate the final βγ dimer map. **B-D.** FSC curves, local resolution estimation, and angular distribution plot of βγ dimer.

Table S1. Cryo-EM data collection, refinement, and validation statistics

	δβγ (EMD-44674) (PDB: 9BLR)	ββγ (EMD-44889) (PDB: 9BTG)	βγ-βγ (EMD-44896) (PDB: 9BTU)
Data Collection and processing			
Magnification (kX)	165	165	165
Voltage (kV)	300	300	300
Electron exposure (e-/Å^2)	50	50	50
Defocus range (μm)	-0.8 to -2.5	-0.8 to -2.5	-0.8 to -2.5
Raw pixel size (Å)	0.40075	0.40075	0.413
Symmetry imposed	C1	C1	C1
Initial particle images (no.)	4,884,175	4,884,175	1,121,564
Final particle images (no.)	192,941	342,011	248,323
Map resolution (Å)	3.38	3.12	3.68
FSC threshold	0.143	0.143	0.143
Map resolution range (Å)	3.56 - 3.18	3.24 - 2.90	3.86 - 3.44
Refinement			
Initial model used (PDB code)	6WTH	6WTH	6WTH
Model resolution (Å)	3.5	3.3	3.9
FSC threshold	0.5	0.5	0.5
Map sharpening B factor (Å^2)	-99	-101	-147
Model composition			
Non-hydrogen atoms	9,477	9,869	7,859
Protein residues	1,155	1,207	837
Ligands	17	12	16
B factors (Å^2)			
Protein	76.56	64.15	146.73
Ligand	100.36	83.25	135.71
Root mean square deviations			
Bond lengths (Å)	0.004	0.005	0.005
Bond angles (°)	0.746	0.744	0.807
Validation			
MolProbity score	0.96	0.65	1.14
Clashscore	0.92	0.41	1.63
Poor rotamers (%)	0.20	0.28	0.13
Ramachandran plot			
Favored (%)	96.89	97.97	96.48
Allowed (%)	3.11	2.03	3.52
Disallowed (%)	0.00	0.00	0.00

Table S2. Root-mean-square deviation of Cα atoms in each subunit domains

	RMSD (subunit superposition)	RMSD (trimer superposition)	RMSD (trimer superposition with β as reference)	
δ-δβγ$_{CYS}$ vs α-αβγ$_{6WTH}$	1.0	1.1	1.8	Upper palm
	2.4	2.3	2.4	Knuckle
	2.2	2.6	3.3	β-ball
	1.4	2.1	3.1	Finger
	1.7	3.5	5.1	Thumb
β-δβγ$_{CYS}$ vs β-αβγ$_{6WTH}$	0.4	0.8	0.4	
	1.2	1.0	1.2	
	0.4	0.8	0.4	
	0.4	0.6	0.4	
	0.5	1.0	0.5	
γ-δβγ$_{CYS}$ vs γ-αβγ$_{6WTH}$	0.6	0.6	0.5	
	0.7	0.6	0.5	
	0.5	0.5	0.8	
	1.8	1.8	2.2	
	0.9	1.1	1.6	
δ-δβγ$_{CYS}$ vs β^{1}-ββγ$_{CYS}$	0.9	0.7	0.9	
	1.9	2.0	2.0	
	2.1	2.1	2.1	
	1.7	1.8	2.2	
	3.0	3.6	3.5	
β-δβγ$_{CYS}$ vs β^{2}-ββγ$_{CYS}$	0.4	0.5	0.4	
	1.0	1.0	1.0	
	0.3	0.5	0.3	
	0.3	0.4	0.3	
	0.3	0.4	0.4	
γ-δβγ$_{CYS}$ vs γ-ββγ$_{CYS}$	0.5	0.3	0.4	
	0.7	0.5	0.4	
	0.4	0.5	0.8	
	1.3	1.4	1.5	
	0.7	0.9	1.2	
β^{1}-ββγ$_{CYS}$ vs α-αβγ$_{6WTH}$	0.8	1.0	1.6	
	1.8	1.0	1.4	
	1.9	2.5	3.1	
	1.7	2.3	3.3	
	2.4	5.3	6.6	
β^{2}-ββγ$_{CYS}$ vs β-αβγ$_{6WTH}$	0.5	0.7	0.5	
	1.1	1.4	1.1	
	0.4	0.7	0.4	
	0.4	0.5	0.4	
	0.4	0.9	0.4	
γ-ββγ$_{CYS}$ vs γ-αβγ$_{6WTH}$	0.4	0.5	0.3	
	0.9	0.4	0.4	
	0.6	0.6	0.7	
	1.1	0.9	1.23	
	0.8	1.4	2.1	

Table S2. Using the rmsd command in ChimeraX, RMSD values were calculated by comparing the Cα positions of each subunit domain between two subunits. The three columns represent RMSD values obtained through three different superpositioning methods: individual subunit superposition, trimer superposition, and trimer superposition using the position 2 β subunit as a reference. The values are color-coded according to the subunit domain: the upper palm, knuckle, β-ball, finger, and thumb domains are colored yellow, cyan, orange, purple, and green, respectively.

Discussion

The trimeric organization of ENaC is evident in three ENaC trimer structures: the previously determined structure of human αβγ trimer, and in this study, the $\delta\beta\gamma_{CYS}$, and $\beta\beta\gamma_{CYS}$ trimers. The selective isolation method implemented in this research prioritizes γ-containing assemblies, potentially overlooking other ENaC proteins with different subunit compositions (Baldin et al., 2020; Chung et al., 2013; Drummond, 2012; Drummond et al., 2000, 1998). Interestingly, this bias towards γ-containing proteins did not result in observable capture of homomeric assemblies or proteins with two γ subunits. While this observation is consistent with previous studies indicating that oocytes expressing only γ do not elicit measurable currents, we cannot rule out limitations in the recombinant system that may inhibit assembly with multiple γ subunits.

This study describes a list of observations that either ground decades of functional experiments in three dimension or unveil novel insights that will serve as foundations for future experiments to understand ENaC function. First, the structure of the human δβγ offers insights into the δ-containing heteromeric assembly. A consistent pattern emerges in these diverse trimers, where β and γ subunits consistently occupy positions 2 and 3, while δ or α takes position 1. The impact of the subunit in position 1 is evident through variations in TriTrp distances; the presence of δ leads to an expanded TriTrp triangle compared to the trimer containing α. Second, while the functional relevance of the ββγ trimer is currently obscured by its failure to traffic to the plasma membrane in HEK cells, the obtained structure provides the first evidence of how a trimer can form containing only β and γ subunits. Understanding the functional impact of the β subunit in position 1 is challenging. Although a study reported that co-expression of β and γ subunits resulted

in channels that respond to shear stress, further investigation is needed to understand the functional role of βββγ (Baldin et al., 2020).

Fourth, the homogeneous conformation observed in the β subunits in position 2 of all three trimers is striking and suggests a scaffolding role of β when occupying position 2. Fifth, this study marks the initial characterization of human δβγ modulation by Zn^{2+}. The opposite responses of δβγ and αβγ to specific concentrations of Zn^{2+} underscore the functional diversity of ENaC. Obtaining a structure of δβγ and αβγ in the presence of Zn^{2+} could shed light on how divalent cations modulate ENaC activity.

Sixth, the presence of a molecule in the palm domains of $\beta\beta\gamma_{CYS}$ and $\delta\beta\gamma_{CYS}$ is surprising, offering a new opportunity to explore the function of ENaC. In $\delta\beta\gamma_{CYS}$, the molecule feature is not as well-defined as in $\beta\beta\gamma_{CYS}$. The map quality in this region in δβγCYS is poor. The lower palm region in αβγ is well-defined and does not display a similar feature suggesting that this peptide-like molecule does not favorably bind to the αβγ trimer (Noreng et al., 2020, 2018). Perhaps, the compact nature of αβγ as demonstrated in its TriTrp distances may hinder access to this unidentified molecule. The positions of the β strands in the lower palm domain in αβγ is incompatible with peptide binding. For the molecule to bind, rearrangement of the β sheets would be required. The potential binding of a peptide-like molecule to ENaC is reminiscent of interactions observed in other ENaC/Deg members, such as the binding of Phe-Met-Arg-Phe-amide (FMRFamide) to FMRFamide-activated sodium channels (FaNaC). However, the binding site in the lower palm domain of ββγCYS and δβγCYS ENaC is distinct from that of FMRFamide in FaNaC, which is located between the finger domain of one subunit and the knuckle domain of the adjacent subunit (Kalienkova et al., 2024; Liu et al., 2023).

Lastly, the βγ dimer implies the potential assembly of the two subunits. Previous studies indicate abundant expression of β and γ subunits in the kidneys at the protein level (Frindt et al., 2022; Hager et al., 2001; Masilamani et al., 1999). Whether these subunits exist in monomeric or dimeric forms remains unclear. However, our findings suggest that they have the capacity to assemble into dimers, possibly serving as assembly intermediates. Currently, there is no *in vivo* evidence for the presence of these dimers, and they may be artifacts of purification. However, their potential relevance to channel assembly cannot be entirely ruled out. Similar intermediates have been previously observed in pentameric cys-loop receptors (Zhu and Gouaux, 2021). In cys-loop receptors, a subset of particles derived from a mouse tissue sample consisting of only three and four subunits was identified, suggesting the presence of assembly intermediates (Zhu and Gouaux, 2021). We acknowledge that the lack of information on the pore domain prevents assigning a functional state to our structures. Nevertheless, the three structures outlined in this study lay the groundwork for future investigations, enabling us to further explore the molecular mechanisms governing the diverse responses driven by the compositional differences in ENaC channels.

Methods

Key resources table

REAGENT or RESOURCE	SOURCE	IDENTIFIER
Antibodies		
10D4 mouse monoclonal	OHSU VGTI, Monoclonal Antibody Core	AB_2744526
Goat anti-Mouse IgG (H+L) Cross-Adsorbed Secondary Antibody, Alexa Fluor™ 594	Invitrogen	A-11005
Bacterial and virus strains		
DH10Bac Competent Cells	Invitrogen	10361012
XL1-Blue competent cells	Agilent	200249
Biological samples		
Xenopus laevis oocytes	Ecocyte Biosciences	https://ecocyte-us.com/
Chemicals, peptides, and recombinant proteins		
Amiloride hydrochloride hydrate	Sigma	Cat#: A7410
Human alpha-Thrombin	Prolytix	HCT-0020
Critical commercial assays		
mMessage mMachine T7 mRNA kit	Invitrogen	AM1344
PureLink™ HiPure Plasmid Miniprep Kit	Invitrogen	K210002
Deposited data		
Human SCNN1D-SCNN1B-SCNN1G ENaC trimer map and coordinates	This paper	PDB: 9BLR EMD-44674 https://doi.org/10.2210/pdb9BLR/pdb
Human SCNN1B-SCNN1B-SCNN1G ENaC trimer map and coordinates	This paper	PDB: 9BTG EMD-44889
Human SCNN1B-SCNN1G ENaC dimer map and coordinates	This paper	PDB: 9BTU EMD-44896
Experimental models: Cell lines		
HEK293S GnTI-	ATCC	Cat #ATCC CRL-3022
Recombinant DNA		
Plasmid: pEG BacMam	Gift from Eric Gouaux	doi: 10.1038/nprot.2014.173
Amiloride-sensitive sodium channel subunit alpha isoform 1	Genscript	NCBI Reference Sequence: NP_001123885.2
Amiloride-sensitive sodium channel subunit beta	Genscript	NCBI Reference Sequence: NP_000327.2
Amiloride-sensitive sodium channel subunit gamma	Genscript	NCBI Reference Sequence: NP_001030.2
Software and algorithms		

CryoSPARC	Doi:10.1038/nmeth.4169	RRID:SCR_016501
Pymol	Pymol Molecular Graphics System, Schrodinger, LLC	RRID:SCR_000305
UCSF ChimeraX	Doi:10.1002/pro.3235	RRID:SCR_015872
Phenix	Doi:10.1107/S2059798318006551	RRID:SCR_014224
ISOLDE	Doi:10.1107/S2059798318002425	https://isolde.cimr.cam.ac.uk/
MolProbity	Doi:10.1107/S0907444909042073	RRID:SCR_014226
Serial EM	Doi:10.1016/j.jsb.2005.07.007	http://bio3d.colorado.edu/SerialEM
Appia	Doi:10.1371/journal.pone.0280255	https://github.com/PlethoraChutney/Appia
TEVC Helper	Dr. Richard Posert	https://github.com/PlethoraChutney/tevc_helper
pClamp	Molecular Devices	RRID:SCR_011323
GraphPad Prism	https://www.graphpad.com/	RRID:SCR_002798

Resource availability

Lead contact

Further information and requests for resources and reagents should be directed to and will be fulfilled by the lead contact, Isabelle Baconguis (bacongui@ohsu.edu).

Materials availability

For any correspondence or requests related to the materials used in this study, please contact the lead contact.

Data and code availability

- Cryo-EM maps and atomic models for δβγCYS, ββγCYS, and βγDimer have been deposited in the Protein Data Bank and Electron Microscopy Data Bank and are publicly

available as of the date of publication. The PDB IDs are 9BLR, 9BTG, and 9BTU. The EMDB IDs are EMD-44674, EMD-44889, and EMD-44896.

- This study does not employ any original code.
- Any additional information required to reanalyze the data reported in this work is available from the lead contact upon request.

Experimental model and study participant details

The cells used for generating baculovirus are Sf9 cells (Spodoptera frugiperda, Cat# CRL-1711) and cultured in 27° C. HEK293S GnTI- suspension cells used for expression of all ENaC proteins in this study were obtained from the ATCC (Cat# CRL-3022) and cultured at 37°C and 8% CO2.

Method details

Construct design

The gene encoding the wild-type human δ ENaC subunit was codon optimized, synthesized, and cloned in the pEG BacMam vector by Genscript (Goehring et al., 2014). The wild-type sequences of the human β and γ subunits from previous structural studies of human αβγ were used. The γ construct consists of an octa-histidine tag, eGFP, and a Thrombin cleavage site at the N-terminus (Noreng et al., 2020). ENaC subunit mutants were also generated by Genscript by site-directed mutagenesis to introduce mutations in cysteine residues within the preTM1 region of each ENaC subunit, along with the R138A mutation in the γ subunit to render it furin-resistant. The δ subunit, along with its own CMV promoter, was then isolated as a cassette using restriction enzymes PmeI and AvrII

and integrated into a pEG BacMam vector containing the N-terminally eGFP tagged γ subunit. This process was repeated with the β subunit so all three genes encoding the δ, β, and γ subunits of ENaC were present in a single plasmid, each with its own CMV promoter. The presence of all ENaC subunit genes were verified by agarose gel electrophoresis following selected restriction enzyme digestion and DNA sequencing. Subsequently, these plasmids were employed to generate bacmid, followed by the production of P1 and P2 viruses for the expression of ENaC (Goehring et al., 2014). The generated viruses were used for various purposes, including electrophysiology studies, expression analysis, and purification.

Small-scale expression and solubilization

For expression optimization, we performed small-scale expression by infecting 20 mL suspension cultures of HEK293 GnTI- at a density of 3x106 cells/mL with baculovirus at an MOI of 2. Baculovirus generation is described in the Construct design section. Following an incubation at 37℃ for 8 hours, 100μM amiloride and 10μM sodium butyrate final concentration were added, and the cells were transferred to an incubator set at 30℃ for protein expression over 24 hours. Then 2 mL aliquots of cells were centrifuged at 5000g for 10 minutes. The resulting pellets were flash-frozen and stored at 80℃. On the day of the experiment, the frozen samples were thawed on ice, and the pellets were washed with 1 mL of HEPES Buffered Saline (pH7.4). Then, 150μl of either DDM solubilization buffer (20 mM n-dodecyl-β-D-maltoside, 3 mM cholesteryl hemisuccinate, 200 mM NaCl, 20 mM HEPES, pH 7.4 and Thermo Fisher Halt Protease Inhibitor Cocktail at a volume ratio of 1:100) or digitonin solubilization buffer (7% digitonin, 200 mM NaCl, 20 mM HEPES pH 7.4 and Thermo Fisher Halt Protease

Inhibitor Cocktail at a volume ratio of 1:100) was used to resuspend the washed pellet, which were then allowed to nutate at 4℃ for 1 hour. Samples were then spun at 71,680g for 20 minutes. The resulting supernatant was loaded into 0.22μm filter tubes and spun at 4000g for 5 minutes at 4℃. Afterward, the samples underwent another round of centrifugation for 40 minutes at 71,680g before proceeding with FSEC or western blot analysis.

Patch-Clamp Electrophysiology

Suspension-adapted HEK293 GnTI- cells were prepared at a density of 3x106 cells/mL and infected with baculovirus, generated as described in Construct design section, at a multiplicity of infection (MOI) of 2. Cells were incubated at 37°C with agitation for 12 hours. Subsequently, amiloride and sodium butyrate were added with a final concentration of 100 μM and 10μM, respectively. The cells were transferred to an incubator set at 30℃. Twenty-four hours post-infection, the cells were plated on glass cover slips in DMEM with 10% FBS at a volume ratio of 1:4 for cells to media.

Whole-cell patch-clamp recordings were carried out 12 hours post-plating the cells in DMEM. Patch pipettes were pulled and polished to 2–3 MΩ resistance using the Sutter Instrument P-97 and Narishige MF-830 Microforge. Pipettes were filled with an internal solution containing 150 mM KCl, 2 mM MgCl2, 5 mM EGTA, and 10 mM HEPES (pH 7.4). For the recording of whole-cell amiloride-sensitive currents, the cells were placed in a bath solution containing 100 μM amiloride, 150 mM NaCl, 2 mM MgCl2, 2 mM CaCl2, and buffered with 10 mM HEPES (pH 7.4). To measure amiloride-sensitive currents, cells were perfused with an external solution that was the same as the bath solution followed by a second external solution lacking amiloride. The amplitude of the

amiloride-sensitive current was determined by the difference between conditions with and without amiloride. For bi-ionic experiments, NaCl was replaced with 150 mM LiCl or 150 mM KCl in the external solution. To generate current-voltage (I-V) trace, currents were recorded while the cell was held at voltage potentials ranging from -80mV to 80mV in 20mV increments while the external solutions containing Na+, Li+, or K+ with or without amiloride were perfused onto the cell. Data was acquired with the Axon Instruments Molecular Devices Axoclamp 200B and Axon DigiData 1550B. Data was analyzed with pClamp, GraphPad Prism, and ABF Plotter (Posert, 2023).

Two-electrode voltage-clamp electrophysiology

Individual wild-type ENaC subunit constructs were cloned into the pcDNA3.1 vector modified to contain a T7 promoter by GenScript. These vectors were linearized and transcribed to generate mRNA using Invitrogen's mMessage mMachine T7 mRNA kit. Oocytes from Ecocyte Bio Science were injected with a total volume of 50 nL containing 1.5 ng of each ENaC subunit. Following injection, oocytes were then incubated at 19℃ in MBSH (88 mM NaCl, 1 mM KCl, 2.4 mM NaHCO3, 10 mM HEPES (pH 7.4), 0.33 mM Ca(NO3)2, 0.41 mM CaCl2, 0.82 mM MgSO4) and supplemented with 150 µg/mL Gentamycin, 250 µg/mL Amikacin, and 100 µM Amiloride. ENaC activity was recorded 18-24 hours post-injection using electrodes filled with 3 M KCl. Bath solutions used were variations of Ringer solution containing 110mM of cation, 1mM KCl, 1.8 mM CaCl2, 5 mM HEPES (pH 7.4). Data was acquired with the Axon CNS Molecular Devices Axoclamp 900A and Digidata 1440A. Data was analyzed with pClamp, GraphPad Prism, and TEVC Helper (Posert, 2023).

Large-scale ENaC expression and purification

Suspension-adapted HEK293 GnTI- cells were prepared at a density of 3x106 cells/mL and infected with baculovirus. Following an incubation at 37℃ for 8 hours, 100 μM amiloride and 10 μM sodium butyrate were added, and the cells were transferred to an incubator set at 30℃ for protein expression over 72 hours. Post-infection, the cells were spun at 5000g for 20 minutes, the supernatant was discarded, and the pellet was flash frozen and stored at -80℃. To begin the purification process, the frozen cell pellet was slowly thawed on ice followed by homogenization in a solubilization buffer consisting of 1% digitonin, 20 mM HEPES pH 7.2, 200 mM NaCl, 2 tablets of Thermo Fisher Protease Inhibitor Cocktail, 2 mM ATP, and 2 mM MgSO4. The solubilization was achieved by stirring the solution at 350 rpm at 4℃ for 1.5 hours, followed by centrifugation at 125,440g for 1 hour to collect the supernatant.

The supernatant was then passed through a GFP Nanobody (GNB) resin packed into an XK 16/40 column for binding. The column underwent successive washing steps: first with 5 column volumes of buffer A containing 0.1% digitonin, 200 mM NaCl, and 20 mM HEPES pH 7.4, then with 2 column volumes of Buffer A supplemented with 2 mM ATP and 2 mM MgCl2, followed by an additional 5 column volumes of Buffer A. For elution, the column was incubated in Buffer A supplemented with 5 mM CaCl2 and 34 μg/mL of Thrombin for 15 minutes at room temperature, from which one column volume separated into fractions were collected. After an additional 30-minute incubation with Thrombin, an additional column volume was collected in fractions. Fractions were run on SDS-PAGE and A260/A280 was measured on a Thermo Scientific NanoDrop One. Samples containing high levels of protein were concentrated with Millipore Amicon Ultra-15 Centrifugal Filters, 100 kDa molecular weight cut-off. Subsequently, the 10d4

Fab was added to the concentrated sample at a molar ratio of 1.5:1 of Fab:ENaC before undergoing centrifugation at 71,680g for 40 minutes. This step was followed by size-exclusion chromatography using a Superose 6 increase 10/300 GL column. Peak fractions were collected. Samples obtained at various purification steps were subjected to examination by SDS-PAGE and assayed by FSEC40. SEC fractions verified to contain ENaC by SDS-PAGE and FSEC were pooled and concentrated to 3-4 mg/mL for grid preparation.

Cryo-EM data acquisition and analysis

The concentrated sample was subjected to centrifugation at 71,680g for 10 minutes at 4℃ followed by addition of fluorinated octyl maltoside to 10 μM. Then, 3 μl of the sample was applied to glow-discharged (15 mA for 60 seconds) Quantifoil holey carbon grids (Au 2 μm/1 μm 200 mesh). The grid was manually blotted followed by a second application of 3 μl, which was then blotted using a Vitrobot Mark IV (FEI). The Vitrobot blot parameters were set to a wait time of 0s, blot time of 2s, and a blot force of 1 with the temperature maintained at 22℃ and humidity at 70%. Grids were then flash frozen in liquid ethane.

Data was collected on a 300 KeV Titan Krios equipped with K3 direct electron detector at the Pacific Northwest Cryo-EM Center (PNCC). Acquisition was automated using SerialEM to find holes with suitable ice thickness using the hole finder feature and combined to produce multishot–multihole targets (Mastronarde, 2005; Schorb et al., 2019). A total dose of 50 e−/Å2 was divided into 50 frames, with a pixel size of 0.8015 Å/pix (0.40075 Å/pix with super resolution) and a defocus range of -0.8 to -2.5 μm. During data collection, CryoSPARC Live was employed initially to handle preliminary

processing and provide an overview of the data collection progress (Punjani et al., 2017). Once the data collection finished, the acquired movies were imported into CryoSPARC for further processing, including motion correction and CTF estimation. Particles were initially picked using blob picker and cleaned using rounds of 2D classification. The selected particles were used for ab-initio reconstruction to generate templates for subsequent template-based particle picking. Template-picked particles underwent additional rounds of refinement including heterogeneous refinement and 3D classification aimed at producing a set of "good" classes representing recognizable ENaC classes. Subsequently, the final particle set was then subjected to local refinement using masks to exclude Fab regions. Multiple rounds of local refinement were performed using different masks to optimize the final reconstructions (Punjani et al., 2020, 2017; Rubinstein and Brubaker, 2015). Finally, the generated maps underwent manual inspection to ensure their quality met the standards necessary for model-building. Additionally, this inspection aimed to assess any limitations that may affect interpretation in subsequent structure analysis.

Model building

The preliminary models of the β and γ subunits derived from PDB 6WTH were initially fitted into the experimental maps. Conversely, for the δ subunit, its initial model was generated utilizing AlphaFold2 (Jumper et al., 2021). Before docking into the map, both the pore and cytosolic domains were removed. Following this, all three subunit models underwent rigid body fitting, accompanied by the removal of loops within disordered regions using Coot (Emsley and Cowtan, 2004). A series of iterative model-building employing ISOLDE and Coot, along with real-space refinement in Phenix, were

conducted until the final models were considered to have satisfactory stereochemistry, as defined by MolProbity (Adams et al., 2002; Croll, 2018; Davis et al., 2004; Emsley et al., 2010; Emsley and Cowtan, 2004). The final model of the $\delta\beta\gamma_{CYS}$ trimer contains residues 126-516 with regions unmodeled in the α2-β4 loop, α6-β11 loop, and the GRIP domain for the δ subunit, residues 78-512 with a region unmodeled in the GRIP domain for the β subunit, and residues 80-521 with regions unmodeled in GRIP domain for the γ subunit. The $\beta\beta\gamma_{CYS}$ trimer model contains residues 78-512 with regions unmodeled in the GRIP and knuckle for the β1 and β2 subunits, and residues 79-522 with regions unmodeled in the GRIP domain of the γ subunit. The βγ contains residues 80-510 with a region unmodeled in the GRIP domain β subunit, and residues 85-516 with regions unmodeled in the GRIP domain for the γ subunit. For structure analysis, angle_between_helices and center_of_mass plugin function in PyMOL Molecular Graphics System (Version 3.0 Schrödinger, LLC) and the rmsd command in ChimeraX were implemented (Goddard et al., 2018; Meng et al., 2023; Pettersen et al., 2021). To generate figures for this study, both PyMOL and ChimeraX were used.

Immunofluorescence Staining

HEK293 GnTI- cells, infected at 3x106 cells/ml, were plated in DMEM supplemented with 10% FBS on a glass bottom 35mm dish resulting in a final cell density of 0.45 x106 cells/ml. The cells were allowed to settle at 30°C for 5 hours. Subsequently, they were rinsed with 1mL PBS and fixed with 4% PFA in PBS for 10 minutes at room temperature with gentle agitation. After fixation, the cells were rinsed twice with 1mL PBS. For permeabilization, 0.1% Triton X-100 in PBS was added and incubated for 20 minutes at room temperature on a nutator. Following this step, the cells were washed twice with

PBS. To reduce non-specific binding, 3% BSA in PBS was applied to all samples and left at 4°C overnight. The next morning, the monoclonal antibody 10d4, directed against the β subunit, was applied at a concentration of 4µg/ml in 3% BSA PBS and incubated for 2 hours at room temperature while nutating. Subsequently, the cells were washed with PBS three times for 5 minutes each. For fluorescent labeling, Alexa Fluor 594 goat anti-mouse antibody, diluted in 3% BSA in PBS at a volume ratio of 1:1000 of antibody to total volume, was added for 1 hour at room temperature on a nutator while being covered in foil to prevent photobleaching. After staining, the cells were washed three times with PBS for 15 minutes each while being kept covered in foil. Images were collected with a Leica DMi8 inverted microscope and analyzed with Leica Application Suite Version 4.12.0.

Chapter Three

Concluding Remarks

Summary

The structure of the δβγ heterotrimer was solved at a resolution of 3.8Å. Although the transmembrane domain was not resolved, a lot of information was gleaned from the resulting model. This work demonstrated that δ ENaC can form a complex with the β and γ subunits and that co-expressing all three subunits together elicits amiloride sensitive currents that are consistent with previous work on δβγ ENaC (Waldmann et al., 1995). In addition to the δβγ structure, ββγ and βγ-βγ complexes were found. This was surprising since these complexes have not been visualized with heterologously expressed αβγ ENaC despite having an identical purification technique. While no amiloride sensitive currents were detected when HEK293 cells were infected with β and γ alone, we were not able to determine whether these novel complexes are functional or not. Based on our immunofluorescence results, the lack of amiloride sensitive currents in whole cell patch clamped HEK293 cells infected with β and γ is in large part due to almost no β being trafficked to the cell membrane in the absence of δ.

As to why our group has not seen ββγ or βγ-βγ in αβγ purifications, this could suggest δ having a low preference to associate with β and γ or an issue with expression of δ itself. The cDNA for δ was inserted into a tricistronic vector with β and γ, a nearly identical vector for αβγ under the same drivers, so an issue with the transcription of δ in HEK293 cells is not likely. It is possible that once transcribed the mRNA for δ is regulated, or even a substantial amount of δ is degraded after translation, or not trafficked to the cell surface at the same rate as β and γ. Unfortunately, without an antibody or a tag for δ we are not able to determine whether an issue with δ regulation in HEK293 cells is to blame. It is also possible that δ preferentially forms a homotrimer, thereby leaving

more free β and γ than co-expressing with α does. It has been suggested in the literature that the δ subunit preferentially forms a homotrimer, especially the δ_2 isoform (Wesch et al., 2012; Yamamura et al., 2004a).

While many unanswered questions remain, a lot of structural information was gathered from our structures. From this work we established for ENaC trimers a naming system for the subunit positions of 1, 2, and 3, with positions 2 and 3 always being occupied by β and γ respectively. By comparing channels with either α, δ, or β in position 1 we were able to visualize the changes that are necessary to accommodate each subunit. Massive changes have to occur in the γ subunit finger and thumb domains in order to accommodate α, δ, or β in position 1. Basing the conformation of the γ subunit in the βγ dimers as the "starting" position, the γ finger and thumb domains swing out away from the distal pore axis to accommodate a subunit in position 1. As different subunits enter position 1, γ has to stretch outward in varying degrees of magnitude for each subunit with an order of $\delta > \beta_1 > \alpha$, with the movements required to accommodate δ in position 1 being the greatest. Interestingly, the conformation of the β subunit when in position 2 in αβγ, δβγ, ββγ, and βγ has very minimal changes, suggesting it may act as a structural scaffold for the channel.

The changes seen in the structure of δβγ and ββγ when compared to αβγ may also be due to a small peptide-like feature between the lower palm domain in nearly the center of the pore axis. This feature has not been seen with αβγ, and while it is better resolved in ββγ, when aligning δβγ and ββγ these features occupy the same space and have the same outline of shape. Since we were not able to visualize the channel pore we are not able to say whether these channels are in an open, closed, or desensitized state. It is possible

though that the presence of this feature is from ββγ and δβγ being in different state than αβγ and that the insertion of this feature either opens or closes the channel. Based on the αβγ structure the beta sheets from each subunit in the lower palm are too close together to accommodate this unidentified molecule (Noreng et al., 2020).

There was also a new feature visible in the γ subunit GRIP domain in the δβγ and ββγ heterotrimers that is not present in αβγ ENaC. This density was not at a high enough resolution to build into, but there is a large portion of the GRIP domain that we are not able to visualize so it is possible that this density is a part of the GRIP domain as opposed to a separate peptide or molecule. Based on work done in mice, the region of the GRIP domain that is predicted to be cleaved for the γ subunit for increased open probability of the ENaC is R153-F163 in mice, these residues in human γ are not yet resolved in any structure of ENaC (Noreng et al., 2020, 2018; Passero et al., 2010). Due to this we are not able to say whether this new density is from a difference in the GRIP being cleaved or not. It has been hypothesized though that the cleavage of the α GRIP inhibitory peptide by furin allows a structural rearrangement of the γ GRIP that allows cleavage (Hughey et al., 2003; Wichmann et al., 2018). From this it is tempting to consider whether the new density in the γ GRIP domain when δ and β occupy position 1 is a result of δ and β not being proteolytically cleaved, leading to a different conformation of the γ GRIP compared to when a furin processed α subunit occupies position 1. This is most likely not the case though because this density is not present in the first αβγ structure where both furin protease sites in the α subunit are removed, inhibiting cleavage of the α GRIP (Noreng et al., 2018). In addition to δβγ and ββγ, the βγ-βγ dimers have this feature in the γ GRIP domain. This suggests the rearrangement of this portion of the γ GRIP domain is

specific to α occupying position 1, even if it is not likely tied to the cleavage of the α GRIP.

This dissertation also describes the first work on Zn^{2+} modulation of δβγ. We demonstrated, what is to our knowledge, the first instance of Zn^{2+} inhibiting δβγ ENaC with an IC_{50} of 63μM. When looking at the structure of δ, in the region corresponding to the acidic pocket in ASIC there are a cluster of histidine residues that are not present in the α subunit (Noreng et al., 2020, 2018; Yoder et al., 2018). Through a series of mutations in this region it was found that perturbing this area leads to a biphasic response of δβγ to Zn^{2+} with low micromolar concentrations activating the channel but then inhibition occurring as concentrations reach millimolar levels (Appendix Figure 1). The biphasic response is reminiscent of αβγ and heterotrimeric ASIC channels (Chen et al., 2012; Sun et al., 2023). The biphasic response in αβγ ENaC has been attributed to a balance of inhibiting and activating Zn^{2+} binding sites in the γ and α subunits (Chen et al., 2012; Sheng et al., 2004). Since concentrations of Zn^{2+} lower than 1μM were not tested, it is possible that at lower concentrations of Zn^{2+} in $\delta\beta\gamma_{WT}$ a biphasic response is present with Zn^{2+} activating δβγ at nanomolar concentrations. If this were true, the increase of current at low micromolar concentrations of Zn^{2+} seen in the histidine pocket mutants could be a result of disrupting a Zn^{2+} binding site and therefore shifting the balance between inhibiting and activating sites for Zn^{2+}.

Lastly, we addressed the controversy of whether human δβγ ENaC is modulated by protons or not. We found that in the presence of low pH solutions the amiloride sensitive current is indeed increased for human δβγ, albeit not to the levels previously claimed (Appendix Figure 8) (Ji and Benos, 2004; Yamamura et al., 2004a). It is curious

that the Althaus lab was not able to visualize the effects of protons on human δβγ or on human αβγ that has previously been established (Zhang et al., 1999). One possibility for the discrepancy could be a difference in the β subunit isoform used. They did not list which isoforms or the sequences they used for human β and γ, but based on the human δ sequence listed in their supplementary table they used isoform 3 of δ (Wichmann et al., 2019). It was not specified anywhere in the text that they used isoform 3 of human δ, so it is possible they used isoform 2 of the β subunit but similarly did not disclose it.

Future Directions

Structure of δβγ ENaC

While a lot of information was garnered from the structure of δβγ ENaC, there are still a lot of questions left unanswered. Most notable is the inability to resolve the transmembrane domains. Without this data it is not possible to determine what state the channel is in or address the differences in selection between α and δ containing ENaC. There are a multitude of possible molecules or associated proteins that could be necessary to stabilize the transmembrane domains. One potential molecule needed for stabilization of the TMs is the presence of PIP2, which has been long established as being involved of gating αβγ ENaC (Abd El-Aziz et al., 2022; Pochynyuk et al., 2006; Yue et al., 2002). Work has been done in our lab reconstituting αβγ ENaC into lipid nanodiscs containing PIP2, though no improvement has been seen in the TMs. Perhaps this means PIP2 is not required for stabilization of the TMs, or perhaps an additional molecule must be present as well. Rather than screening through all of the possible combinations of associating factors that ENaC could require to stabilize the TMs, a next step could be optimizing SMA nanodiscs (styrene maleic acid nanodiscs) or a similar method to maintain the

native lipid environment. It has been established that the δβγ channel is functional when expressed in HEK293 cells. Using SMA could ensure that any necessary lipids or molecules for TM stabilization were present. Alternatively, removal of sections from the N- and C- terminus of δ, β, and γ could be another way to stabilize the TMs. Noreng and colleagues used truncated ENaC to solve the first structure of the αβγ heterotrimer (Noreng et al., 2018). This structure had densities present for the transmembrane domains, though they were not at a high enough resolution to model build with. Utilizing a similar construct design for δβγ, with the improvements in microscopes and data processing software, the transmembrane domains for δβγ may start to be visualized.

Another unanswered question is why there was such a large amount free β and γ when co-expressed with δ ENaC. As mentioned previously, it has been suggested that δ preferentially forms homotrimers (Wesch et al., 2012; Yamamura et al., 2004a). To determine whether δ preferentially forms homotrimers or whether it was an issue with δ expression or regulation, the δ subunit could be tagged. It has already been demonstrated that the *Xenopus* δ subunit tolerates an HA tag on the N terminus (Wichmann et al., 2018). Using affinity purification with agarose beads conjugated to HA antibodies, only complexes containing δ could be pulled down. Following purification, one could quickly test whether the β subunit was present in FSEC by incubating with the β antibody 10d4 to identify whether a shift occurs or not. Using western blots, one could also compare staining for the HA tag to stains for β and γ to see if any large discrepancy in expression is visible for the subunits. An even better alternative would be development of a δ antibody. Even though our work shows that δ can associate with β and γ we still do not know whether that happens in the human brain. With a δ specific antibody, purification

from native tissue could be performed leaving us with a much better understanding of what proteins form a channel with δ ENaC *in vivo*.

Zn^{2+} modulation of δβγ

To further understand the modulation of δβγ by Zn^{2+}, mutations in the residues proposed to be involved in Zn^{2+} modulation in αβγ can be made for functional testing in *Xenopus* oocytes. In the γ subunit H188, H195, and H233 have been suggested as Zn^{2+} interacting sites responsible for channel activation whereas H88 and D510 has been suggested as being involved in Zn^{2+} inhibition of αβγ (Chen et al., 2012; Sheng et al., 2004). I propose creating the γ H88A and D510 mutations from the Chen and colleagues paper as single and double mutants in the γ RNA and then co-express each γ mutant with wild type δ and β ($\delta\beta\gamma_{WT}$) or with the δ histidine pocket mutants ($\delta\beta\gamma_{H252A\ H315Q\ R139Y}$). Using TEVC we would be able to test whether H88 and D510 play in the Zn^{2+} inhibition of δβγ. It would also be interesting to see how a H188A, H195A, and H233A triple mutant γ would affect the biphasic response seen in the δ histidine pocket triple mutant or if increased inhibition by Zn^{2+} would be seen when the γ triple mutant is co-expressed with wild type δ ENaC.

Appendix

A

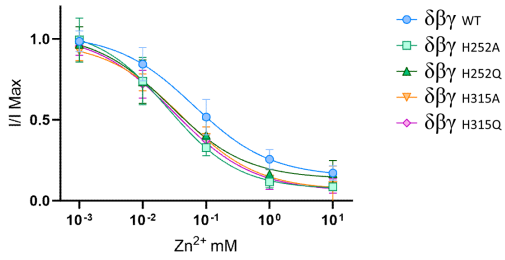

B

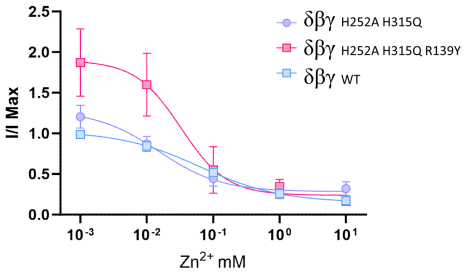

C

	Zn^{2+} IC50 μM
$\delta\beta\gamma_{WT}$	63.0
$\delta\beta\gamma_{H252A}$	26.2
$\delta\beta\gamma_{H252Q}$	27.4
$\delta\beta\gamma_{H315A}$	40.9
$\delta\beta\gamma_{H315Q}$	30.1
$\delta\beta\gamma_{H252A\ H315Q}$	12.9
$\delta\beta\gamma_{H252A\ H315Q\ R139Y}$	44.5

D

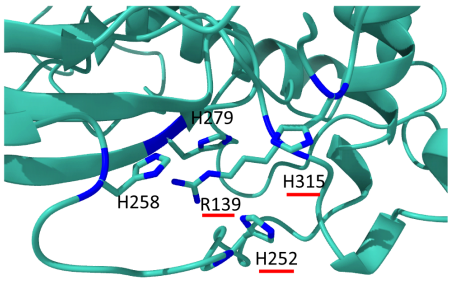

E

β2-α2 loop

α 134 TLNPYRYPEIK 144
δ 135 DGNPRRPSPVL 145

α2

α 244 GVDAVREWYRFHYINILSRLPETLPSLEEDTLGNFIFA 281
δ 225 GVAAVQDWYHFHYVDILALLPAAWEDSHGSQDGHFVLS 262

β4-β5

α 295 SHFHHPMYGNCYT 307
δ 276 RTFHHPTYGSCYT 288

β6-β7 loop

α 333 RAEQNDFIPLLSTVTGA 349
δ 309 RVEQQPHLPLLSTLAGI 325

F

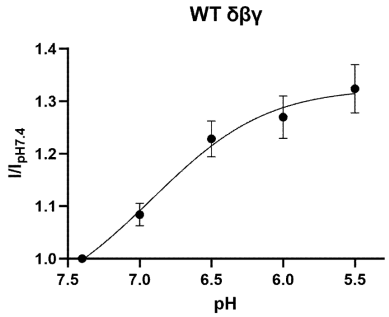

Figure 1. Zn^{2+} and pH modulation of δβγ ENaC. Related to Figures 1 and S1.

Two electrode voltage clamp data from *Xenopus* oocytes **A.** Dose-response of δβγ single mutants to Zn^{2+}. Current ratios were determined by measuring current amplitudes before and after application of Zn^{2+}. Data are represented as mean ± SEM ($\delta\beta\gamma_{WT}$ n=12, $\delta\beta\gamma_{H252A}$ n=9, $\delta\beta\gamma_{H252Q}$ n=7, $\delta\beta\gamma_{H315A}$ n=9, $\delta\beta\gamma_{H315Q}$ n=10). **B.** Dose-response of δβγ single mutants to Zn^{2+}. Current ratios were determined by measuring current amplitudes before and after application of Zn^{2+}. Data are represented as mean ± SEM ($\delta\beta\gamma_{WT}$ n=12, $\delta\beta\gamma_{H252A\ H315Q}$ n=5, $\delta\beta\gamma_{H252A\ H315Q\ R139Y}$ n=6). **C.** Zn^{2+} IC_{50} values for $\delta\beta\gamma_{WT}$ and the single and double mutants from (A) and (B). **D.** Model highlighting residues mutated in the histidine pocket from (A-C). **E.** Sequence alignment of α and δ ENaC of regions from the histidine pocket shown in (D). Residues that were mutated in the δ subunit and their corresponding residues in α are bolded. **F.** Amiloride sensitive currents of $\delta\beta\gamma_{WT}$ when the bath is at varying pH values normalized to the current when the bath is at pH 7.4. Data is represented as mean ± SEM (n=14).

References

Abd El-Aziz, T.M., Kaur, A., Shapiro, M.S., Stockand, J.D., Archer, C.R., 2022. Optogenetic Control of PIP2 Interactions Shaping ENaC Activity. Int. J. Mol. Sci. 23, 3884. https://doi.org/10.3390/ijms23073884

Abramson, J., Adler, J., Dunger, J., Evans, R., Green, T., Pritzel, A., Ronneberger, O., Willmore, L., Ballard, A.J., Bambrick, J., Bodenstein, S.W., Evans, D.A., Hung, C.-C., O'Neill, M., Reiman, D., Tunyasuvunakool, K., Wu, Z., Žemgulytė, A., Arvaniti, E., Beattie, C., Bertolli, O., Bridgland, A., Cherepanov, A., Congreve, M., Cowen-Rivers, A.I., Cowie, A., Figurnov, M., Fuchs, F.B., Gladman, H., Jain, R., Khan, Y.A., Low, C.M.R., Perlin, K., Potapenko, A., Savy, P., Singh, S., Stecula, A., Thillaisundaram, A., Tong, C., Yakneen, S., Zhong, E.D., Zielinski, M., Žídek, A., Bapst, V., Kohli, P., Jaderberg, M., Hassabis, D., Jumper, J.M., 2024. Accurate structure prediction of biomolecular interactions with AlphaFold 3. Nature 630, 493–500. https://doi.org/10.1038/s41586-024-07487-w

Adams, C.M., Anderson, M.G., Motto, D.G., Price, M.P., Johnson, W.A., Welsh, M.J., 1998. Ripped pocket and pickpocket, novel Drosophila DEG/ENaC subunits expressed in early development and in mechanosensory neurons. J. Cell Biol. 140, 143–152. https://doi.org/10.1083/jcb.140.1.143

Adams, P.D., Grosse-Kunstleve, R.W., Hung, L.-W., Ioerger, T.R., McCoy, A.J., Moriarty, N.W., Read, R.J., Sacchettini, J.C., Sauter, N.K., Terwilliger, T.C., 2002. PHENIX: building new software for automated crystallographic structure determination. Acta Crystallogr. D Biol. Crystallogr. 58, 1948–1954. https://doi.org/10.1107/S0907444902016657

Adebamiro, A., Cheng, Y., Rao, U.S., Danahay, H., Bridges, R.J., 2007. A Segment of γ ENaC Mediates Elastase Activation of Na+ Transport. J. Gen. Physiol. 130, 611–629. https://doi.org/10.1085/jgp.200709781

Alexander, S., Mathie, A., Peters, J., 2011. Ion Channels. Br. J. Pharmacol. 164, S137–S174. https://doi.org/10.1111/j.1476-5381.2011.01649_5.x

Alvarez de la Rosa, D., Zhang, P., Shao, D., White, F., Canessa, C.M., 2002. Functional implications of the localization and activity of acid-sensitive channels in rat peripheral nervous system. Proc. Natl. Acad. Sci. U. S. A. 99, 2326–2331. https://doi.org/10.1073/pnas.042688199

Amin, M.S., Wang, H.-W., Reza, E., Whitman, S.C., Tuana, B.S., Leenen, F.H.H., 2005. Distribution of epithelial sodium channels and mineralocorticoid receptors in cardiovascular regulatory centers in rat brain. Am. J. Physiol.-Regul. Integr. Comp. Physiol. 289, R1787–R1797. https://doi.org/10.1152/ajpregu.00063.2005

Anderson, P.A.V., Greenberg, R.M., 2001. Phylogeny of ion channels: clues to structure and function. Comp. Biochem. Physiol. B Biochem. Mol. Biol. 129, 17–28. https://doi.org/10.1016/S1096-4959(01)00376-1

Babini, E., Geisler, H.-S., Siba, M., Gründer, S., 2003. A New Subunit of the Epithelial Na+ Channel Identifies Regions Involved in Na+ Self-inhibition*. J. Biol. Chem. 278, 28418–28426. https://doi.org/10.1074/jbc.M301315200

Baconguis, I., Bohlen, C.J., Goehring, A., Julius, D., Gouaux, E., 2014. X-Ray Structure of Acid-Sensing Ion Channel 1–Snake Toxin Complex Reveals Open State of a Na+-Selective Channel. Cell 156, 717–729. https://doi.org/10.1016/j.cell.2014.01.011

Baer, J.E., Jones, C.B., Spitzer, S.A., Russo, H.F., 1967. The Potassium-Sparing and Natriuretic Activity of N-Amidino-3,5-Diamino-6-Chloropyrazinecar-Boxamide Hydrochloride Dihydrate (amiloride Hydrochloride). J. Pharmacol. Exp. Ther. 157, 472–485.

Baldin, J.-P., Barth, D., Fronius, M., 2020. Epithelial Na+ Channel (ENaC) Formed by One or Two Subunits Forms Functional Channels That Respond to Shear Force. Front. Physiol. 11.

Benos, D.J., Mandel, L.J., Simon, S.A., 1980. Cationic selectivity and competition at the sodium entry site in frog skin. J. Gen. Physiol. 76, 233–247. https://doi.org/10.1085/jgp.76.2.233

Bentley, P.J., 1968. Amiloride: a potent inhibitor of sodium transport across the toad bladder. J. Physiol. 195, 317–330.

Bentley, P.J., 1958. The effects of neurohypophysial extracts on the water transfer across the wall of the isolated urinary bladder of the toad Bufo marinus. J. Endocrinol. 17, 201–209. https://doi.org/10.1677/joe.0.0170201

Biasio, W., Chang, T., McIntosh, C.J., McDonald, F.J., 2004. Identification of Murr1 as a Regulator of the Human δ Epithelial Sodium Channel. J. Biol. Chem. 279, 5429–5434. https://doi.org/10.1074/jbc.M311155200

Bize, V., Horisberger, J.-D., 2007. Sodium self-inhibition of human epithelial sodium channel: selectivity and affinity of the extracellular sodium sensing site. Am. J. Physiol.-Ren. Physiol. 293, F1137–F1146. https://doi.org/10.1152/ajprenal.00100.2007

Bortner, C.D., Cidlowski, J.A., 2014. Ion channels and apoptosis in cancer. Philos. Trans. R. Soc. B Biol. Sci. 369, 20130104. https://doi.org/10.1098/rstb.2013.0104

Brockway, L.M., Zhou, Z.-H., Bubien, J.K., Jovov, B., Benos, D.J., Keyser, K.T., 2002. Rabbit retinal neurons and glia express a variety of ENaC/DEG subunits. Am. J. Physiol.-Cell Physiol. 283, C126–C134. https://doi.org/10.1152/ajpcell.00457.2001

Bruns, J.B., Carattino, M.D., Sheng, S., Maarouf, A.B., Weisz, O.A., Pilewski, J.M., Hughey, R.P., Kleyman, T.R., 2007. Epithelial Na+ Channels Are Fully Activated by Furin- and Prostasin-dependent Release of an Inhibitory Peptide from the γ-Subunit*. J. Biol. Chem. 282, 6153–6160. https://doi.org/10.1074/jbc.M610636200

Canessa, C.M., Horisberger, J.-D., Rossier, B.C., 1993. Epithelial sodium channel related to proteins involved in neurodegeneration. Nature 361, 467–470. https://doi.org/10.1038/361467a0

Canessa, C.M., Schild, L., Buell, G., Thorens, B., Gautschi, I., Horisberger, J.-D., Rossier, B.C., 1994. Amiloride-sensitive epithelial Na + channel is made of three homologous subunits. Nature 367, 463–467. https://doi.org/10.1038/367463a0

Chalfant, M.L., Denton, J.S., Berdiev, B.K., Ismailov, I.I., Benos, D.J., Stanton, B.A., 1999. Intracellular H+ regulates the alpha-subunit of ENaC, the epithelial Na+ channel. Am. J. Physiol. 276, C477-486. https://doi.org/10.1152/ajpcell.1999.276.2.C477

Chalfie, M., Au, M., 1989. Genetic Control of Differentiation of the Caenorhabditis elegans Touch Receptor Neurons. Science 243, 1027–1033. https://doi.org/10.1126/science.2646709

Chalfie, M., Wolinsky, E., 1990. The identification and suppression of inherited neurodegeneration in Caenorhabditis elegans. Nature 345, 410–416. https://doi.org/10.1038/345410a0

Champigny, G., Voilley, N., Waldmann, R., Lazdunski, M., 1998. Mutations causing neurodegeneration in Caenorhabditis elegans drastically alter the pH sensitivity and

inactivation of the mammalian H+-gated Na+ channel MDEG1. J. Biol. Chem. 273, 15418–15422. https://doi.org/10.1074/jbc.273.25.15418
Chang, T., Ke, Y., Ly, K., McDonald, F.J., 2011. COMMD1 regulates the delta epithelial sodium channel (δENaC) through trafficking and ubiquitination. Biochem. Biophys. Res. Commun. 411, 506–511. https://doi.org/10.1016/j.bbrc.2011.06.149
Chen, J., Winarski, K.L., Myerburg, M.M., Pitt, B.R., Sheng, S., 2012. Probing the Structural Basis of Zn2+ Regulation of the Epithelial Na+ Channel. J. Biol. Chem. 287, 35589–35598. https://doi.org/10.1074/jbc.M112.394734
Chraïbi, A., Vallet, V., Firsov, D., Hess, S.K., Horisberger, J.-D., 1998. Protease Modulation of the Activity of the Epithelial Sodium Channel Expressed in Xenopus Oocytes. J. Gen. Physiol. 111, 127–138. https://doi.org/10.1085/jgp.111.1.127
Chung, W.-S., Weissman, J.L., Farley, J., Drummond, H.A., 2013. βENaC is required for whole cell mechanically gated currents in renal vascular smooth muscle cells. Am. J. Physiol.-Ren. Physiol. 304, F1428–F1437. https://doi.org/10.1152/ajprenal.00444.2012
Crabbé, J., 1961. STIMULATION OF ACTIVE SODIUM TRANSPORT BY THE ISOLATED TOAD BLADDER WITH ALDOSTERONE IN VITRO*. J. Clin. Invest. 40, 2103–2110.
Croll, T.I., 2018. ISOLDE: a physically realistic environment for model building into low-resolution electron-density maps. Acta Crystallogr. Sect. Struct. Biol. 74, 519–530. https://doi.org/10.1107/S2059798318002425
Darboux, I., Lingueglia, E., Pauron, D., Barbry, P., Lazdunski, M., 1998. A new member of the amiloride-sensitive sodium channel family in Drosophila melanogaster peripheral nervous system. Biochem. Biophys. Res. Commun. 246, 210–216. https://doi.org/10.1006/bbrc.1998.8183
Davis, I.W., Murray, L.W., Richardson, J.S., Richardson, D.C., 2004. MolProbity: structure validation and all-atom contact analysis for nucleic acids and their complexes. Nucleic Acids Res. 32, W615–W619. https://doi.org/10.1093/nar/gkh398
de la Rosa, D.A., Krueger, S.R., Kolar, A., Shao, D., Fitzsimonds, R.M., Canessa, C.M., 2003. Distribution, subcellular localization and ontogeny of ASIC1 in the mammalian central nervous system. J. Physiol. 546, 77–87. https://doi.org/10.1113/jphysiol.2002.030692
de la Rosa, D.A., Li, H., Canessa, C.M., 2002. Effects of Aldosterone on Biosynthesis, Traffic, and Functional Expression of Epithelial Sodium Channels in A6 Cells. J. Gen. Physiol. 119, 427–442. https://doi.org/10.1085/jgp.20028559
Diakov, A., Bera, K., Mokrushina, M., Krueger, B., Korbmacher, C., 2008. Cleavage in the γ-subunit of the epithelial sodium channel (ENaC) plays an important role in the proteolytic activation of near-silent channels. J. Physiol. 586, 4587–4608. https://doi.org/10.1113/jphysiol.2008.154435
Donaldson, S.H., Hirsh, A., Li, D.C., Holloway, G., Chao, J., Boucher, R.C., Gabriel, S.E., 2002. Regulation of the Epithelial Sodium Channel by Serine Proteases in Human Airways*. J. Biol. Chem. 277, 8338–8345. https://doi.org/10.1074/jbc.M105044200
Downs, C.A., Johnson, N.M., Coca, C., Helms, M.N., 2018. Angiotensin II regulates δ-ENaC in human umbilical vein endothelial cells. Microvasc. Res. 116, 26–33. https://doi.org/10.1016/j.mvr.2017.10.001
Driscoll, M., Chalfie, M., 1991. The mec-4 gene is a member of a family of Caenorhabditis elegans genes that can mutate to induce neuronal degeneration. Nature 349, 588–593. https://doi.org/10.1038/349588a0

Drummond, H.A., 2012. βENaC is a molecular component of a VSMC mechanotransducer that contributes to renal blood flow regulation, protection from renal injury, and hypertension. Front. Physiol. 3. https://doi.org/10.3389/fphys.2012.00341
Drummond, H.A., Abboud, F.M., Welsh, M.J., 2000. Localization of β and γ subunits of ENaC in sensory nerve endings in the rat foot pad. Brain Res. 884, 1–12. https://doi.org/10.1016/S0006-8993(00)02831-6
Drummond, H.A., Gebremedhin, D., Harder, D.R., 2004. Degenerin/epithelial Na+ channel proteins: components of a vascular mechanosensor. Hypertens. Dallas Tex 1979 44, 643–648. https://doi.org/10.1161/01.HYP.0000144465.56360.ad
Drummond, H.A., Price, M.P., Welsh, M.J., Abboud, F.M., 1998. A Molecular Component of the Arterial Baroreceptor Mechanotransducer. Neuron 21, 1435–1441. https://doi.org/10.1016/S0896-6273(00)80661-3
Duggan, A., Garcia-Anoveros, J., Corey, D.P., 2002. The PDZ domain protein PICK1 and the sodium channel BNaC1 interact and localize at mechanosensory terminals of dorsal root ganglion neurons and dendrites of central neurons. J. Biol. Chem. 277, 5203–5208. https://doi.org/10.1074/jbc.M104748200
Emsley, P., Cowtan, K., 2004. Coot: model-building tools for molecular graphics. Acta Crystallogr. D Biol. Crystallogr. 60, 2126–2132. https://doi.org/10.1107/S0907444904019158
Emsley, P., Lohkamp, B., Scott, W.G., Cowtan, K., 2010. Features and development of Coot. Acta Crystallogr. D Biol. Crystallogr. 66, 486–501. https://doi.org/10.1107/S0907444910007493
Ergonul, Z., Frindt, G., Palmer, L.G., 2006. Regulation of maturation and processing of ENaC subunits in the rat kidney. Am. J. Physiol.-Ren. Physiol. 291, F683–F693. https://doi.org/10.1152/ajprenal.00422.2005
Fedorovich, S.V., Dubouskaya, T.G., Waseem, T.V., 2020. Synaptic receptors for low pH in extracellular space: metabotropic receptors are an underestimated factor in stroke. Neural Regen. Res. 15, 2033–2034. https://doi.org/10.4103/1673-5374.282249
Feldman, D.H., Horiuchi, M., Keachie, K., Mccauley, E., Bannerman, P., Itoh, A., Itoh, T., Pleasure, D., 2008. Characterization of acid-sensing ion channel expression in oligodendrocyte-lineage cells. Glia 56, 1238–1249. https://doi.org/10.1002/glia.20693
Frindt, G., Ergonul, Z., Palmer, L.G., 2008. Surface Expression of Epithelial Na Channel Protein in Rat Kidney. J. Gen. Physiol. 131, 617–627. https://doi.org/10.1085/jgp.200809989
Frindt, G., Meyerson, J.R., Satty, A., Scandura, J.M., Palmer, L.G., 2022. Expression of ENaC subunits in epithelia. J. Gen. Physiol. 154, e202213124. https://doi.org/10.1085/jgp.202213124
Fuchs, W., Larsen, E.H., Lindemann, B., 1977. Current-voltage curve of sodium channels and concentration dependence of sodium permeability in frog skin. J. Physiol. 267, 137–166. https://doi.org/10.1113/jphysiol.1977.sp011805
Fuhrman, F.A., Ussing, H.H., 1951. A characteristic response of the isolated frog skin potential to neurohypophysial principles and its relation to the transport of sodium and water. J. Cell. Comp. Physiol. 38, 109–130. https://doi.org/10.1002/jcp.1030380109
García-Añoveros, J., Derfler, B., Neville-Golden, J., Hyman, B.T., Corey, D.P., 1997. BNaC1 and BNaC2 constitute a new family of human neuronal sodium channels related to

degenerins and epithelial sodium channels. Proc. Natl. Acad. Sci. U. S. A. 94, 1459–1464. https://doi.org/10.1073/pnas.94.4.1459
García-Caballero, A., Dang, Y., He, H., Stutts, M.J., 2008. ENaC Proteolytic Regulation by Channel-activating Protease 2. J. Gen. Physiol. 132, 521–535. https://doi.org/10.1085/jgp.200810030
Garty, H., Palmer, L., 1997. Epithelial sodium channels: function, structure, and regulation. Physiol. Rev. 77, 359–396. https://doi.org/10.1152/physrev.1997.77.2.359
Giraldez, T., Afonso-Oramas, D., Cruz-Muros, I., Garcia-Marin, V., Pagel, P., González-Hernández, T., Rosa, D.A.D.L., 2007. Cloning and functional expression of a new epithelial sodium channel δ subunit isoform differentially expressed in neurons of the human and monkey telencephalon. J. Neurochem. 102, 1304–1315. https://doi.org/10.1111/j.1471-4159.2007.04622.x
Giraldez, T., Rojas, P., Jou, J., Flores, C., Alvarez de la Rosa, D., 2012. The epithelial sodium channel δ-subunit: new notes for an old song. Am. J. Physiol. Renal Physiol. 303, F328-338. https://doi.org/10.1152/ajprenal.00116.2012
Goehring, A., Lee, C.-H., Wang, K.H., Michel, J.C., Claxton, D.P., Baconguis, I., Althoff, T., Fischer, S., Garcia, K.C., Gouaux, E., 2014. Screening and large-scale expression of membrane proteins in mammalian cells for structural studies. Nat. Protoc. 9, 2574–2585. https://doi.org/10.1038/nprot.2014.173
Gonzales, E.B., Kawate, T., Gouaux, E., 2009. Pore architecture and ion sites in acid sensing ion channels and P2X receptors. Nature 460, 599–604. https://doi.org/10.1038/nature08218
Goulet, C.C., Volk, K.A., Adams, C.M., Prince, L.S., Stokes, J.B., Snyder, P.M., 1998. Inhibition of the epithelial Na+ channel by interaction of Nedd4 with a PY motif deleted in Liddle's syndrome. J. Biol. Chem. 273, 30012–30017. https://doi.org/10.1074/jbc.273.45.30012
Haerteis, S., Krueger, B., Korbmacher, C., Rauh, R., 2009. The δ-Subunit of the Epithelial Sodium Channel (ENaC) Enhances Channel Activity and Alters Proteolytic ENaC Activation*. J. Biol. Chem. 284, 29024–29040. https://doi.org/10.1074/jbc.M109.018945
Hager, H., Kwon, T.-H., Vinnikova, A.K., Masilamani, S., Brooks, H.L., Frøkiaer, J., Knepper, M.A., Nielsen, S., 2001. Immunocytochemical and immunoelectron microscopic localization of α-, β-, and γ-ENaC in rat kidney. Am. J. Physiol.-Ren. Physiol. 280, F1093–F1106. https://doi.org/10.1152/ajprenal.2001.280.6.F1093
Hanukoglu, I., Hanukoglu, A., 2016. Epithelial sodium channel (ENaC) family: Phylogeny, structure–function, tissue distribution, and associated inherited diseases. Gene 579, 95–132. https://doi.org/10.1016/j.gene.2015.12.061
Harris, M., Firsov, D., Vuagniaux, G., Stutts, M.J., Rossier, B.C., 2007. A Novel Neutrophil Elastase Inhibitor Prevents Elastase Activation and Surface Cleavage of the Epithelial Sodium Channel Expressed in *Xenopus laevis* Oocytes*. J. Biol. Chem. 282, 58–64. https://doi.org/10.1074/jbc.M605125200
Hong, K., Driscoll, M., 1994. A transmembrane domain of the putative channel subunit MEC-4 influences mechanotransduction and neurodegeneration in C. elegans. Nature 367, 470–473. https://doi.org/10.1038/367470a0
Huang, C., Hu, Z.-L., Wu, W.-N., Yu, D.-F., Xiong, Q.-J., Song, J.-R., Shu, Q., Fu, H., Wang, F., Chen, J.-G., 2010. Existence and distinction of acid-evoked currents in rat astrocytes. Glia 58, 1415–1424. https://doi.org/10.1002/glia.21017

Huang, M., Chalfie, M., 1994. Gene interactions affecting mechanosensory transduction in Caenorhabditis elegans. Nature 367, 467–470. https://doi.org/10.1038/367467a0
Hughey, R.P., Bruns, J.B., Kinlough, C.L., Harkleroad, K.L., Tong, Q., Carattino, M.D., Johnson, J.P., Stockand, J.D., Kleyman, T.R., 2004. Epithelial Sodium Channels Are Activated by Furin-dependent Proteolysis*. J. Biol. Chem. 279, 18111–18114. https://doi.org/10.1074/jbc.C400080200
Hughey, R.P., Mueller, G.M., Bruns, J.B., Kinlough, C.L., Poland, P.A., Harkleroad, K.L., Carattino, M.D., Kleyman, T.R., 2003. Maturation of the Epithelial Na+ Channel Involves Proteolytic Processing of the α- and γ-Subunits*. J. Biol. Chem. 278, 37073–37082. https://doi.org/10.1074/jbc.M307003200
Hummler, E., 1999. Implication of ENaC in salt-sensitive hypertension. J. Steroid Biochem. Mol. Biol. 69, 385–390. https://doi.org/10.1016/S0960-0760(99)00073-4
Hummler, E., Barker, P., Gatzy, J., Beermann, F., Verdumo, C., Schmidt, A., Boucher, R., Rossier, B.C., 1996. Early death due to defective neonatal lung liquid clearance in αENaC-deficient mice. Nat. Genet. 12, 325–328. https://doi.org/10.1038/ng0396-325
Jasti, J., Furukawa, H., Gonzales, E.B., Gouaux, E., 2007. Structure of acid-sensing ion channel 1 at 1.9 Å resolution and low pH. Nature 449, 316–323. https://doi.org/10.1038/nature06163
Ji, H.-L., Benos, D.J., 2004. Degenerin Sites Mediate Proton Activation of δβγ-Epithelial Sodium Channel. J. Biol. Chem. 279, 26939–26947. https://doi.org/10.1074/jbc.M401143200
Ji, H.-L., Bishop, L.R., Anderson, S.J., Fuller, C.M., Benos, D.J., 2004. The Role of Pre-H2 Domains of α- and δ-Epithelial Na+ Channels in Ion Permeation, Conductance, and Amiloride Sensitivity*. J. Biol. Chem. 279, 8428–8440. https://doi.org/10.1074/jbc.M312012200
Ji, H.-L., Zhao, R.-Z., Chen, Z.-X., Shetty, S., Idell, S., Matalon, S., 2012. δ ENaC: a novel divergent amiloride-inhibitable sodium channel. Am. J. Physiol.-Lung Cell. Mol. Physiol. 303, L1013–L1026. https://doi.org/10.1152/ajplung.00206.2012
Jumper, J., Evans, R., Pritzel, A., Green, T., Figurnov, M., Ronneberger, O., Tunyasuvunakool, K., Bates, R., Žídek, A., Potapenko, A., Bridgland, A., Meyer, C., Kohl, S.A.A., Ballard, A.J., Cowie, A., Romera-Paredes, B., Nikolov, S., Jain, R., Adler, J., Back, T., Petersen, S., Reiman, D., Clancy, E., Zielinski, M., Steinegger, M., Pacholska, M., Berghammer, T., Bodenstein, S., Silver, D., Vinyals, O., Senior, A.W., Kavukcuoglu, K., Kohli, P., Hassabis, D., 2021. Highly accurate protein structure prediction with AlphaFold. Nature 596, 583–589. https://doi.org/10.1038/s41586-021-03819-2
Kabra, R., Knight, K.K., Zhou, R., Snyder, P.M., 2008. Nedd4-2 Induces Endocytosis and Degradation of Proteolytically Cleaved Epithelial Na+ Channels*. J. Biol. Chem. 283, 6033–6039. https://doi.org/10.1074/jbc.M708555200
Kalienkova, V., Dandamudi, M., Paulino, C., Lynagh, T., 2024. Structural basis for excitatory neuropeptide signaling. Nat. Struct. Mol. Biol. 31, 717–726. https://doi.org/10.1038/s41594-023-01198-y
Kashlan, O.B., Blobner, B.M., Zuzek, Z., Tolino, M., Kleyman, T.R., 2015. Na+ Inhibits the Epithelial Na+ Channel by Binding to a Site in an Extracellular Acidic Cleft*. J. Biol. Chem. 290, 568–576. https://doi.org/10.1074/jbc.M114.606152
Kawate, T., Gouaux, E., 2006. Fluorescence-detection size-exclusion chromatography for precrystallization screening of integral membrane proteins. Struct. Lond. Engl. 1993 14, 673–681. https://doi.org/10.1016/j.str.2006.01.013

Ke, Y., Butt, A.G., Swart, M., Liu, Y.F., McDonald, F.J., 2010. COMMD1 downregulates the epithelial sodium channel through Nedd4–2. Am. J. Physiol.-Ren. Physiol. 298, F1445–F1456. https://doi.org/10.1152/ajprenal.00257.2009

Kellenberger, S., Auberson, M., Gautschi, I., Schneeberger, E., Schild, L., 2001. Permeability Properties of Enac Selectivity Filter Mutants. J. Gen. Physiol. 118, 679–692. https://doi.org/10.1085/jgp.118.6.679

Kellenberger, S., Gautschi, I., Schild, L., 1999a. A single point mutation in the pore region of the epithelial Na+ channel changes ion selectivity by modifying molecular sieving. Proc. Natl. Acad. Sci. 96, 4170–4175. https://doi.org/10.1073/pnas.96.7.4170

Kellenberger, S., Hoffmann-Pochon, N., Gautschi, I., Schneeberger, E., Schild, L., 1999b. On the Molecular Basis of Ion Permeation in the Epithelial Na+ Channel. J. Gen. Physiol. 114, 13–30. https://doi.org/10.1085/jgp.114.1.13

Kellenberger, S., Schild, L., 2002a. Epithelial Sodium Channel/Degenerin Family of Ion Channels: A Variety of Functions for a Shared Structure. Physiol. Rev. 82, 735–767. https://doi.org/10.1152/physrev.00007.2002

Kellenberger, S., Schild, L., 2002b. Epithelial Sodium Channel/Degenerin Family of Ion Channels: A Variety of Functions for a Shared Structure. Physiol. Rev. 82, 735–767. https://doi.org/10.1152/physrev.00007.2002

Kemendy, A.E., Kleyman, T.R., Eaton, D.C., 1992. Aldosterone alters the open probability of amiloride-blockable sodium channels in A6 epithelia. https://doi.org/10.1152/ajpcell.1992.263.4.C825. https://doi.org/10.1152/ajpcell.1992.263.4.C825

Kleyman, T.R., Carattino, M.D., Hughey, R.P., 2009. ENaC at the Cutting Edge: Regulation of Epithelial Sodium Channels by Proteases. J. Biol. Chem. 284, 20447–20451. https://doi.org/10.1074/jbc.R800083200

Koefoed-Johnsen, V., Ussing, H.H., 1958. The Nature of the Frog Skin Potential.

Konstas, A.-A., Mavrelos, D., Korbmacher, C., 2000. Conservation of pH sensitivity in the epithelial sodium channel (ENaC) with Liddle's syndrome mutation. Pflüg. Arch. 441, 341–350. https://doi.org/10.1007/s004240000430

Krueger, B., Schlötzer-Schrehardt, U., Haerteis, S., Zenkel, M., Chankiewitz, V.E., Amann, K.U., Kruse, F.E., Korbmacher, C., 2012. Four subunits (αβγδ) of the epithelial sodium channel (ENaC) are expressed in the human eye in various locations. Invest. Ophthalmol. Vis. Sci. 53, 596–604. https://doi.org/10.1167/iovs.11-8581

Kubala, M.H., Kovtun, O., Alexandrov, K., Collins, B.M., 2010. Structural and thermodynamic analysis of the GFP:GFP-nanobody complex. Protein Sci. 19, 2389–2401. https://doi.org/10.1002/pro.519

Leaf, A., Anderson, J., Page, L.B., 1958. ACTIVE SODIUM TRANSPORT BY THE ISOLATED TOAD BLADDER. J. Gen. Physiol. 41, 657–668.

Lemmens-Gruber, R., Tzotzos, S., 2023. The Epithelial Sodium Channel—An Underestimated Drug Target. Int. J. Mol. Sci. 24, 7775. https://doi.org/10.3390/ijms24097775

Li, J., Sheng, S., Perry, C.J., Kleyman, T.R., 2003. Asymmetric Organization of the Pore Region of the Epithelial Sodium Channel*. J. Biol. Chem. 278, 13867–13874. https://doi.org/10.1074/jbc.M300149200

Lingueglia, E., de Weille, J.R., Bassilana, F., Heurteaux, C., Sakai, H., Waldmann, R., Lazdunski, M., 1997. A modulatory subunit of acid sensing ion channels in brain and dorsal root ganglion cells. J. Biol. Chem. 272, 29778–29783. https://doi.org/10.1074/jbc.272.47.29778

Lingueglia, E., Voilley, N., Waldmann, R., Lazdunski, M., Barbry, P., 1993. Expression cloning of an epithelial amiloride-sensitive Na+ channel. FEBS Lett. 318, 95–99. https://doi.org/10.1016/0014-5793(93)81336-X

Liu, F., Dang, Y., Li, L., Feng, H., Li, J., Wang, H., Zhang, X., Zhang, Z., Ye, S., Tian, Y., Chen, Q., 2023. Structure and mechanism of a neuropeptide-activated channel in the ENaC/DEG superfamily. Nat. Chem. Biol. 19, 1276–1285. https://doi.org/10.1038/s41589-023-01401-7

Loffing, J., Pietri, L., Aregger, F., Bloch-Faure, M., Ziegler, U., Meneton, P., Rossier, B.C., Kaissling, B., 2000. Differential subcellular localization of ENaC subunits in mouse kidney in response to high- and low-Na diets. Am. J. Physiol.-Ren. Physiol. 279, F252–F258. https://doi.org/10.1152/ajprenal.2000.279.2.F252

Ly, K., McIntosh, C.J., Biasio, W., Liu, Y., Ke, Y., Olson, D.R., Miller, J.H., Page, R., Snyder, P.M., McDonald, F.J., 2013. Regulation of the delta and alpha epithelial sodium channel (ENaC) by ubiquitination and Nedd8. J. Cell. Physiol. 228, 2190–2201. https://doi.org/10.1002/jcp.24390

Mall, M.A., Button, B., Johannesson, B., Zhou, Z., Livraghi, A., Caldwell, R.A., Schubert, S.C., Schultz, C., O'Neal, W.K., Pradervand, S., Hummler, E., Rossier, B.C., Grubb, B.R., Boucher, R.C., 2010. Airway Surface Liquid Volume Regulation Determines Different Airway Phenotypes in Liddle Compared with βENaC-overexpressing Mice *. J. Biol. Chem. 285, 26945–26955. https://doi.org/10.1074/jbc.M110.151803

Masilamani, S., Kim, G.H., Mitchell, C., Wade, J.B., Knepper, M.A., 1999. Aldosterone-mediated regulation of ENaC alpha, beta, and gamma subunit proteins in rat kidney. J. Clin. Invest. 104, R19-23. https://doi.org/10.1172/JCI7840

Mastronarde, D.N., 2005. Automated electron microscope tomography using robust prediction of specimen movements. J. Struct. Biol. 152, 36–51. https://doi.org/10.1016/j.jsb.2005.07.007

May, A., Puoti, A., Gaeggeler, H.P., Horisberger, J.D., Rossier, B.C., 1997. Early effect of aldosterone on the rate of synthesis of the epithelial sodium channel alpha subunit in A6 renal cells. J. Am. Soc. Nephrol. 8, 1813. https://doi.org/10.1681/ASN.V8121813

McDonald, F.J., Price, M.P., Snyder, P.M., Welsh, M.J., 1995. Cloning and expression of the beta- and gamma-subunits of the human epithelial sodium channel. https://doi.org/10.1152/ajpcell.1995.268.5.C1157. https://doi.org/10.1152/ajpcell.1995.268.5.C1157

Mueller, G.M., Maarouf, A.B., Kinlough, C.L., Sheng, N., Kashlan, O.B., Okumura, S., Luthy, S., Kleyman, T.R., Hughey, R.P., 2010. Cys Palmitoylation of the β Subunit Modulates Gating of the Epithelial Sodium Channel. J. Biol. Chem. 285, 30453–30462. https://doi.org/10.1074/jbc.M110.151845

Mukherjee, A., Mueller, G.M., Kinlough, C.L., Sheng, N., Wang, Z., Mustafa, S.A., Kashlan, O.B., Kleyman, T.R., Hughey, R.P., 2014. Cysteine Palmitoylation of the γ Subunit Has a Dominant Role in Modulating Activity of the Epithelial Sodium Channel. J. Biol. Chem. 289, 14351–14359. https://doi.org/10.1074/jbc.M113.526020

Muntner, P., Carey, R.M., Gidding, S., Jones, D.W., Taler, S.J., Wright, J.T., Whelton, P.K., 2018. Potential U.S. Population Impact of the 2017 American College of Cardiology/American Heart Association High Blood Pressure Guideline. Circulation 137, 109–118. https://doi.org/10.1161/CIRCULATIONAHA.117.032582

Noreng, S., Bharadwaj, A., Posert, R., Yoshioka, C., Baconguis, I., 2018. Structure of the human epithelial sodium channel by cryo-electron microscopy. eLife 7, e39340. https://doi.org/10.7554/eLife.39340

Noreng, S., Posert, R., Bharadwaj, A., Houser, A., Baconguis, I., 2020. Molecular principles of assembly, activation, and inhibition in epithelial sodium channel. eLife 9, e59038. https://doi.org/10.7554/eLife.59038

Ota, T., Suzuki, Y., Nishikawa, T., Otsuki, T., Sugiyama, T., Irie, R., Wakamatsu, A., Hayashi, K., Sato, H., Nagai, K., Kimura, K., Makita, H., Sekine, M., Obayashi, M., Nishi, T., Shibahara, T., Tanaka, T., Ishii, S., Yamamoto, J., Saito, K., Kawai, Y., Isono, Y., Nakamura, Yoshitaka, Nagahari, K., Murakami, K., Yasuda, T., Iwayanagi, T., Wagatsuma, M., Shiratori, A., Sudo, H., Hosoiri, T., Kaku, Y., Kodaira, H., Kondo, H., Sugawara, M., Takahashi, M., Kanda, K., Yokoi, T., Furuya, T., Kikkawa, E., Omura, Y., Abe, K., Kamihara, K., Katsuta, N., Sato, K., Tanikawa, M., Yamazaki, Makoto, Ninomiya, K., Ishibashi, T., Yamashita, H., Murakawa, K., Fujimori, K., Tanai, H., Kimata, M., Watanabe, Motoji, Hiraoka, S., Chiba, Y., Ishida, S., Ono, Y., Takiguchi, S., Watanabe, S., Yosida, M., Hotuta, T., Kusano, J., Kanehori, K., Takahashi-Fujii, A., Hara, H., Tanase, T., Nomura, Y., Togiya, S., Komai, F., Hara, R., Takeuchi, K., Arita, M., Imose, N., Musashino, K., Yuuki, H., Oshima, A., Sasaki, N., Aotsuka, S., Yoshikawa, Y., Matsunawa, H., Ichihara, T., Shiohata, N., Sano, S., Moriya, S., Momiyama, H., Satoh, N., Takami, S., Terashima, Y., Suzuki, O., Nakagawa, S., Senoh, A., Mizoguchi, H., Goto, Y., Shimizu, F., Wakebe, H., Hishigaki, H., Watanabe, T., Sugiyama, A., Takemoto, M., Kawakami, B., Yamazaki, Masaaki, Watanabe, K., Kumagai, A., Itakura, S., Fukuzumi, Y., Fujimori, Y., Komiyama, M., Tashiro, H., Tanigami, A., Fujiwara, T., Ono, T., Yamada, K., Fujii, Y., Ozaki, K., Hirao, M., Ohmori, Y., Kawabata, A., Hikiji, T., Kobatake, N., Inagaki, H., Ikema, Y., Okamoto, S., Okitani, R., Kawakami, T., Noguchi, S., Itoh, T., Shigeta, K., Senba, T., Matsumura, K., Nakajima, Y., Mizuno, T., Morinaga, M., Sasaki, M., Togashi, T., Oyama, M., Hata, H., Watanabe, Manabu, Komatsu, T., Mizushima-Sugano, J., Satoh, T., Shirai, Y., Takahashi, Y., Nakagawa, K., Okumura, K., Nagase, T., Nomura, N., Kikuchi, H., Masuho, Y., Yamashita, R., Nakai, K., Yada, T., Nakamura, Yusuke, Ohara, O., Isogai, T., Sugano, S., 2004. Complete sequencing and characterization of 21,243 full-length human cDNAs. Nat. Genet. 36, 40–45. https://doi.org/10.1038/ng1285

Palmer, L.G., 1982. Ion selectivity of the apical membrane Na channel in the toad urinary bladder. J. Membr. Biol. 67, 91–98. https://doi.org/10.1007/BF01868651

Palmer, L. G., Frindt, G., 1986. Epithelial sodium channels: characterization by using the patch-clamp technique. Fed. Proc. 45, 2708–2712.

Palmer, L G, Frindt, G., 1986. Amiloride-sensitive Na channels from the apical membrane of the rat cortical collecting tubule. Proc. Natl. Acad. Sci. U. S. A. 83, 2767–2770.

Passero, C.J., Carattino, M.D., Kashlan, O.B., Myerburg, M.M., Hughey, R.P., Kleyman, T.R., 2010. Defining an inhibitory domain in the gamma subunit of the epithelial sodium channel. Am. J. Physiol.-Ren. Physiol. 299, F854–F861. https://doi.org/10.1152/ajprenal.00316.2010

Passero, C.J., Mueller, G.M., Rondon-Berrios, H., Tofovic, S.P., Hughey, R.P., Kleyman, T.R., 2008. Plasmin Activates Epithelial Na+ Channels by Cleaving the γ Subunit*. J. Biol. Chem. 283, 36586–36591. https://doi.org/10.1074/jbc.M805676200

Picard, N., Eladari, D., El Moghrabi, S., Planès, C., Bourgeois, S., Houillier, P., Wang, Q., Burnier, M., Deschenes, G., Knepper, M.A., Meneton, P., Chambrey, R., 2008.

Defective ENaC Processing and Function in Tissue Kallikrein-deficient Mice*. J. Biol. Chem. 283, 4602–4611. https://doi.org/10.1074/jbc.M705664200
Pochynyuk, O., Tong, Q., Staruschenko, A., Ma, H.-P., Stockand, J.D., 2006. Regulation of the epithelial Na+ channel (ENaC) by phosphatidylinositides. Am. J. Physiol.-Ren. Physiol. 290, F949–F957. https://doi.org/10.1152/ajprenal.00386.2005
Pohorille, A., Schweighofer, K., Wilson, M.A., 2005. The origin and early evolution of membrane channels. Astrobiology 5, 1–17. https://doi.org/10.1089/ast.2005.5.1
Posert, R., 2023. TEVC_Helper.
Price, M.P., Gong, H., Parsons, M.G., Kundert, J.R., Reznikov, L.R., Bernardinelli, L., Chaloner, K., Buchanan, G.F., Wemmie, J.A., Richerson, G.B., Cassell, M.D., Welsh, M.J., 2014. Localization and behaviors in null mice suggest that ASIC1 and ASIC2 modulate responses to aversive stimuli. Genes Brain Behav. 13, 179–194. https://doi.org/10.1111/gbb.12108
Punjani, A., Rubinstein, J.L., Fleet, D.J., Brubaker, M.A., 2017. cryoSPARC: algorithms for rapid unsupervised cryo-EM structure determination. Nat. Methods 14, 290–296. https://doi.org/10.1038/nmeth.4169
Punjani, A., Zhang, H., Fleet, D.J., 2020. Non-uniform refinement: adaptive regularization improves single-particle cryo-EM reconstruction. Nat. Methods 17, 1214–1221. https://doi.org/10.1038/s41592-020-00990-8
Rauh, R., Hoerner, C., Korbmacher, C., 2016. δβγ-ENaC is inhibited by CFTR but stimulated by cAMP in Xenopus laevis oocytes. Am. J. Physiol.-Lung Cell. Mol. Physiol. 312, L277–L287. https://doi.org/10.1152/ajplung.00375.2016
Rothbauer, U., Zolghadr, K., Muyldermans, S., Schepers, A., Cardoso, M.C., Leonhardt, H., 2008. A Versatile Nanotrap for Biochemical and Functional Studies with Fluorescent Fusion Proteins*. Mol. Cell. Proteomics 7, 282–289. https://doi.org/10.1074/mcp.M700342-MCP200
Rubinstein, J.L., Brubaker, M.A., 2015. Alignment of cryo-EM movies of individual particles by optimization of image translations. J. Struct. Biol., Recent Advances in Detector Technologies and Applications for Molecular TEM 192, 188–195. https://doi.org/10.1016/j.jsb.2015.08.007
Schild, L., Schneeberger, E., Gautschi, I., Firsov, D., 1997. Identification of Amino Acid Residues in the α, β, and γ Subunits of the Epithelial Sodium Channel (ENaC) Involved in Amiloride Block and Ion Permeation. J. Gen. Physiol. 109, 15–26. https://doi.org/10.1085/jgp.109.1.15
Schorb, M., Haberbosch, I., Hagen, W.J.H., Schwab, Y., Mastronarde, D.N., 2019. Software tools for automated transmission electron microscopy. Nat. Methods 16, 471–477. https://doi.org/10.1038/s41592-019-0396-9
Shareghi, G.R., Stoner, L.C., 1978. Calcium transport across segments of the rabbit distal nephron in vitro. Am. J. Physiol. 235, F367-375. https://doi.org/10.1152/ajprenal.1978.235.4.F367
Sheng, S., Carattino, M.D., Bruns, J.B., Hughey, R.P., Kleyman, T.R., 2006. Furin cleavage activates the epithelial Na+ channel by relieving Na+ self-inhibition. Am. J. Physiol.-Ren. Physiol. 290, F1488–F1496. https://doi.org/10.1152/ajprenal.00439.2005
Sheng, S., Li, J., McNulty, K.A., Avery, D., Kleyman, T.R., 2000. Characterization of the selectivity filter of the epithelial sodium channel. J. Biol. Chem. 275, 8572–8581. https://doi.org/10.1074/jbc.275.12.8572

Sheng, S., Perry, C.J., Kleyman, T.R., 2004. Extracellular Zn2+ Activates Epithelial Na+ Channels by Eliminating Na+ Self-inhibition *. J. Biol. Chem. 279, 31687–31696. https://doi.org/10.1074/jbc.M405224200

Shimkets, R.A., Lifton, R., Canessa, C.M., 1998. In vivo phosphorylation of the epithelial sodium channel. Proc. Natl. Acad. Sci. U. S. A. 95, 3301–3305.

Snyder, P.M., Bucher, D.B., Olson, D.R., 2000. Gating Induces a Conformational Change in the Outer Vestibule of Enac. J. Gen. Physiol. 116, 781–790. https://doi.org/10.1085/jgp.116.6.781

Soundararajan, R., Pearce, D., Hughey, R.P., Kleyman, T.R., 2010. Role of Epithelial Sodium Channels and Their Regulators in Hypertension*. J. Biol. Chem. 285, 30363–30369. https://doi.org/10.1074/jbc.R110.155341

Stähler, F., Riedel, K., Demgensky, S., Neumann, K., Dunkel, A., Täubert, A., Raab, B., Behrens, M., Raguse, J.-D., Hofmann, T., Meyerhof, W., 2008. A Role of the Epithelial Sodium Channel in Human Salt Taste Transduction? Chemosens. Percept. 1, 78–90. https://doi.org/10.1007/s12078-008-9006-4

Staruschenko, A., Adams, E., Booth, R.E., Stockand, J.D., 2005. Epithelial Na+ Channel Subunit Stoichiometry. Biophys. J. 88, 3966–3975. https://doi.org/10.1529/biophysj.104.056804

Staub, O., Dho, S., Henry, P., Correa, J., Ishikawa, T., McGlade, J., Rotin, D., 1996. WW domains of Nedd4 bind to the proline-rich PY motifs in the epithelial Na+ channel deleted in Liddle's syndrome. EMBO J. 15, 2371–2380.

Stockand, J.D., 2002. New ideas about aldosterone signaling in epithelia. Am. J. Physiol.-Ren. Physiol. 282, F559–F576. https://doi.org/10.1152/ajprenal.00320.2001

Sun, A.W., Wu, M.H., Vijayalingam, M., Wacker, M.J., Chu, X.-P., 2023. The Role of Zinc in Modulating Acid-Sensing Ion Channel Function. Biomolecules 13, 229. https://doi.org/10.3390/biom13020229

Sutherland, S.P., Benson, C.J., Adelman, J.P., McCleskey, E.W., 2001. Acid-sensing ion channel 3 matches the acid-gated current in cardiac ischemia-sensing neurons. Proc. Natl. Acad. Sci. U. S. A. 98, 711–716. https://doi.org/10.1073/pnas.98.2.711

Ugawa, S., Ueda, T., Minami, Y., Horimoto, M., Shimada, S., 2001. A single amino acid substitution in MDEG2 specifically alters desensitization of the proton-activated cation current. NeuroReport 12, 2141–2145. https://doi.org/10.1097/00001756-200107200-00020

Ulmschneider, M.B., Bagnéris, C., McCusker, E.C., DeCaen, P.G., Delling, M., Clapham, D.E., Ulmschneider, J.P., Wallace, B.A., 2013. Molecular dynamics of ion transport through the open conformation of a bacterial voltage-gated sodium channel. Proc. Natl. Acad. Sci. 110, 6364–6369. https://doi.org/10.1073/pnas.1214667110

Ussing, H.H., 1949. The Active Ion Transport through the Isolated Frog Skin in the Light of Tracer Studies. Acta Physiol. Scand. 17, 1–37. https://doi.org/10.1111/j.1748-1716.1949.tb00550.x

Vallet, V., Chraibi, A., Gaeggeler, H.-P., Horisberger, J.-D., Rossier, B.C., 1997. An epithelial serine protease activates the amiloride-sensitive sodium channel. Nature 389, 607–610. https://doi.org/10.1038/39329

Vergo, S., Craner, M.J., Etzensperger, R., Attfield, K., Friese, M.A., Newcombe, J., Esiri, M., Fugger, L., 2011. Acid-sensing ion channel 1 is involved in both axonal injury and demyelination in multiple sclerosis and its animal model. Brain J. Neurol. 134, 571–584. https://doi.org/10.1093/brain/awq337

Verrey, F., 1995. Transcriptional control of sodium transport in tight epithelia by adrenal steroids. J. Membr. Biol. 144, 93–110. https://doi.org/10.1007/BF00232796

Vuagniaux, G., Vallet, V., Jaeger, N.F., Hummler, E., Rossier, B.C., 2002. Synergistic Activation of ENaC by Three Membrane-bound Channel-activating Serine Proteases (mCAP1, mCAP2, and mCAP3) and Serum- and Glucocorticoid-regulated Kinase (Sgk1) in Xenopus Oocytes. J. Gen. Physiol. 120, 191–201. https://doi.org/10.1085/jgp.20028598

Waldmann, R., Champigny, G., Bassilana, F., Heurteaux, C., Lazdunski, M., 1997. A proton-gated cation channel involved in acid-sensing. Nature 386, 173–177. https://doi.org/10.1038/386173a0

Waldmann, R., Champigny, G., Bassilana, F., Voilley, N., Lazdunski, M., 1995. Molecular Cloning and Functional Expression of a Novel Amiloride-sensitive Na+ Channel. J. Biol. Chem. 270, 27411–27414. https://doi.org/10.1074/jbc.270.46.27411

Wang, H., Traub, L.M., Weixel, K.M., Hawryluk, M.J., Shah, N., Edinger, R.S., Perry, C.J., Kester, L., Butterworth, M.B., Peters, K.W., Kleyman, T.R., Frizzell, R.A., Johnson, J.P., 2006. Clathrin-mediated endocytosis of the epithelial sodium channel. Role of epsin. J. Biol. Chem. 281, 14129–14135. https://doi.org/10.1074/jbc.M512511200

Wang, J., Ou, S.-W., Wang, Y.-J., 2017. Distribution and function of voltage-gated sodium channels in the nervous system. Channels 11, 534–554. https://doi.org/10.1080/19336950.2017.1380758

Wemmie, J.A., Askwith, C.C., Lamani, E., Cassell, M.D., Freeman, J.H., Welsh, M.J., 2003. Acid-Sensing Ion Channel 1 Is Localized in Brain Regions with High Synaptic Density and Contributes to Fear Conditioning. J. Neurosci. 23, 5496–5502. https://doi.org/10.1523/JNEUROSCI.23-13-05496.2003

Wesch, D., Althaus, M., Miranda, P., Cruz-Muros, I., Fronius, M., González-Hernández, T., Clauss, W.G., Alvarez de la Rosa, D., Giraldez, T., 2012. Differential N termini in epithelial Na+ channel δ-subunit isoforms modulate channel trafficking to the membrane. Am. J. Physiol. Cell Physiol. 302, C868-879. https://doi.org/10.1152/ajpcell.00255.2011

Wichmann, L., Dulai, J.S., Marles-Wright, J., Maxeiner, S., Szczesniak, P.P., Manzini, I., Althaus, M., 2019. An extracellular acidic cleft confers profound H^+-sensitivity to epithelial sodium channels containing the δ-subunit in *Xenopus laevis*. J. Biol. Chem. 294, 12507–12520. https://doi.org/10.1074/jbc.RA119.008255

Wichmann, L., Vowinkel, K.S., Perniss, A., Manzini, I., Althaus, M., 2018. Incorporation of the δ-subunit into the epithelial sodium channel (ENaC) generates protease-resistant ENaCs in Xenopus laevis. J. Biol. Chem. 293, 6647–6658. https://doi.org/10.1074/jbc.RA118.002543

Yamamura, H., Ugawa, S., Ueda, T., Nagao, M., Joh, T., Shimada, S., 2008a. Epithelial Na+ channel delta subunit is an acid sensor in the human oesophagus. Eur. J. Pharmacol. 600, 32–36. https://doi.org/10.1016/j.ejphar.2008.10.022

Yamamura, H., Ugawa, S., Ueda, T., Nagao, M., Shimada, S., 2008b. Epithelial Na+ channel delta subunit mediates acid-induced ATP release in the human skin. Biochem. Biophys. Res. Commun. 373, 155–158. https://doi.org/10.1016/j.bbrc.2008.06.008

Yamamura, H., Ugawa, S., Ueda, T., Nagao, M., Shimada, S., 2006. A novel spliced variant of the epithelial Na+ channel δ-subunit in the human brain. Biochem. Biophys. Res. Commun. 349, 317–321. https://doi.org/10.1016/j.bbrc.2006.08.043

Yamamura, H., Ugawa, S., Ueda, T., Nagao, M., Shimada, S., 2005. Icilin activates the delta-subunit of the human epithelial Na+ channel. Mol. Pharmacol. 68, 1142–1147. https://doi.org/10.1124/mol.104.010850

Yamamura, H., Ugawa, S., Ueda, T., Nagao, M., Shimada, S., 2004a. Protons Activate the δ-Subunit of the Epithelial Na+ Channel in Humans. J. Biol. Chem. 279, 12529–12534. https://doi.org/10.1074/jbc.M400274200

Yamamura, H., Ugawa, S., Ueda, T., Nagao, M., Shimada, S., 2004b. Capsazepine Is a Novel Activator of the δ Subunit of the Human Epithelial Na+ Channel. J. Biol. Chem. 279, 44483–44489. https://doi.org/10.1074/jbc.M408929200

Yang, F., Sun, X., Ding, Y., Ma, H., Yang, T.O., Ma, Y., Wei, D., Li, W., Xu, T., Jiang, W., 2016. Astrocytic Acid-Sensing Ion Channel 1a Contributes to the Development of Chronic Epileptogenesis. Sci. Rep. 6, 31581. https://doi.org/10.1038/srep31581

Yoder, N., Gouaux, E., 2020. The His-Gly motif of acid-sensing ion channels resides in a reentrant 'loop' implicated in gating and ion selectivity. eLife 9, e56527. https://doi.org/10.7554/eLife.56527

Yoder, N., Yoshioka, C., Gouaux, E., 2018. Gating mechanisms of acid-sensing ion channels. Nature 555, 397–401. https://doi.org/10.1038/nature25782

Yu, X.-W., Hu, Z.-L., Ni, M., Fang, P., Zhang, P.-W., Shu, Q., Fan, H., Zhou, H.-Y., Ni, L., Zhu, L.-Q., Chen, J.-G., Wang, F., 2015. Acid-sensing ion channels promote the inflammation and migration of cultured rat microglia. Glia 63, 483–496. https://doi.org/10.1002/glia.22766

Yue, Gang, Malik, B., Yue, Guichin, Eaton, D.C., 2002. Phosphatidylinositol 4,5-Bisphosphate (PIP2) Stimulates Epithelial Sodium Channel Activity in A6 Cells *. J. Biol. Chem. 277, 11965–11969. https://doi.org/10.1074/jbc.M108951200

Zhang, P., Fyfe, G.K., Grichtchenko, I.I., Canessa, C.M., 1999. Inhibition of alphabeta epithelial sodium channels by external protons indicates that the second hydrophobic domain contains structural elements for closing the pore. Biophys. J. 77, 3043–3051. https://doi.org/10.1016/S0006-3495(99)77135-3

Zhang, Y., Sloan, S.A., Clarke, L.E., Caneda, C., Plaza, C.A., Blumenthal, P.D., Vogel, H., Steinberg, G.K., Edwards, M.S.B., Li, G., Duncan, J.A., Cheshier, S.H., Shuer, L.M., Chang, E.F., Grant, G.A., Gephart, M.G.H., Barres, B.A., 2016. Purification and Characterization of Progenitor and Mature Human Astrocytes Reveals Transcriptional and Functional Differences with Mouse. Neuron 89, 37–53. https://doi.org/10.1016/j.neuron.2015.11.013

Zhao, R.-Z., Nie, H.-G., Su, X.-F., Han, D.-Y., Lee, A., Huang, Y., Chang, Y., Matalon, S., Ji, H.-L., 2012. Characterization of a novel splice variant of δ ENaC subunit in human lungs. Am. J. Physiol. Lung Cell. Mol. Physiol. 302, L1262-1272. https://doi.org/10.1152/ajplung.00331.2011

Zhu, H., Gouaux, E., 2021. Architecture and assembly mechanism of native glycine receptors. Nature 599, 513–517. https://doi.org/10.1038/s41586-021-04022-z